POLDER-2

Land Surface Level-3 Products

User Manual

Algorithm Description & Product validation

Issue 1.40

Prepared by Roselyne Lacaze (MEDIAS-France)

Issue 1.40 – August 26th 2005

Content

List of figures

List of Tables

1. Introduction

Monitoring of terrestrial vegetation from satellites at global and regional scales requires accurate and frequent measurements of surface reflectance. In this context, the POLDER instrument leads a key improvement providing, at high temporal resolution, measurements of the Bi-directional Reflectance Distribution Function (BRDF) corrected for atmospheric effects.

The first algorithms of the "Land Surface" processing line have been applied to the 8 months of ADEOS-1/POLDER-1 data. The methodology, which takes advantage of the POLDER directionality, is presented in Leroy et al. (1997). The Level 3 products are generated over a synthesis period of 30 days with a sliding window to get a temporal resolution of 10 days. Advanced algorithms have been developed to be applied to ADEOS-2/POLDER-2 data and to re-processed ADEOS-1/POLDER-1 data. In addition to the Leaf Area Index (LAI) retrieval, the major improvements are:

- A multi-temporal filtering module that eliminates the observations contaminated by residual clouds and/or aerosols.
- The inversion of a new 3-coefficients semi-empirical BRDF model (Maignan et al., 2004) to normalize the bi-directional measurements
- The application of temporal weighting favouring the data collected in the middle of the synthesis period. Thus, the smoothing of the temporal variations of the biophysical parameters due to the monthly synthesis decreases.
- An error is associated with each retrieved parameter. It depends on both the input data quality, and the retrieval algorithm, what concerns the technical sensor characteristics, the calibration accuracy, the cloud detection and atmospheric correction quality, the model ability to simulate the BRDF, and the inversion method relevancy. The estimated error is an approximation itself, and is only an indicator of the influence of all previous factors on the retrieved parameters.

2. Land Surface Level 3 algorithms

The "Land Surface" Level 3 processing line generates 2 products from ADEOS-2/POLDER-2 data (Figure 1):

- The "Directional Parameters" product contains the 3 directional coefficients resulting from the inversion of a BRDF model (Maignan et al., 2004).
- The "Albedo and Vegetation" product contains the spectral Directional-Hemispherical Reflectances, DHR, and the Normalized Difference Vegetation Index (NDVI) corrected for directional effects, already present in ADEOS-1/POLDER-1 products. Two new biophysical parameters are added: the Leaf Area Index (LAI) and the Fraction of Vegetation Cover (FVC).

The "Land Surface" Level 3 algorithm relies on 3 major steps (Figure 1):

- the filtering module
- the linear inversion of a BRDF model

- the inversion of a vegetation model by a neural network to retrieve the LAI

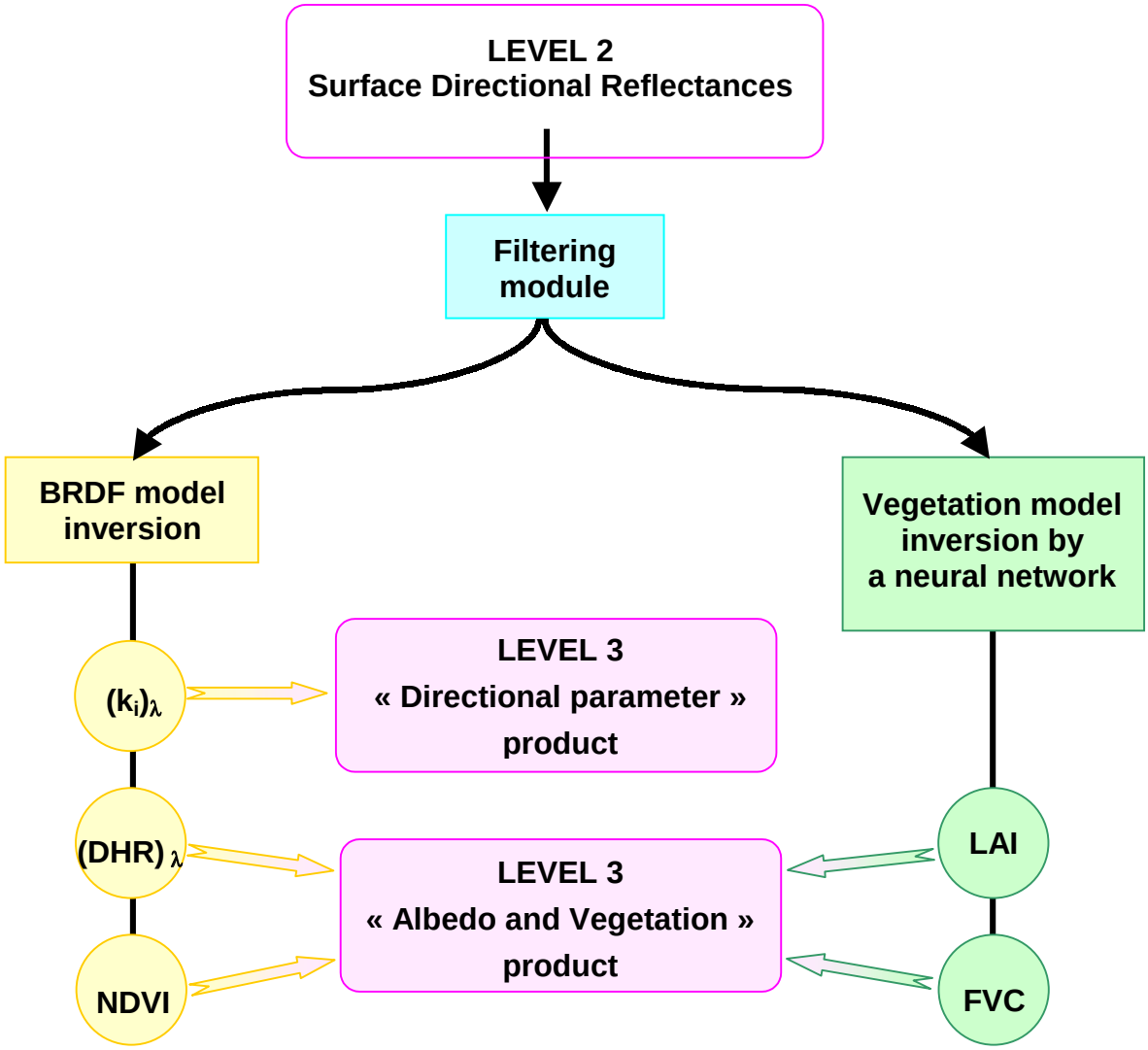

Figure 1 : Outline of the Level 3 Land Surface processing line

2.1. The filtering module

The multi-directional spectral reflectances are the inputs of the "Land Surface" Level 3 processing line. Their quality controls the relevance of biophysical parameters. In order to eliminate contaminated measurements not detected by the Level 2 cloud detection and atmospheric corrections, a multi-temporal filtering module has been developed.

The filtering module is applied to 443nm bi-directional reflectances. Indeed, in this spectral range, the land surface reflectance is low and the measured signal is largely due to atmospheric interactions such as gaseous absorption, Rayleigh scattering and aerosol effects. In order to reduce the impact of the bi-directional effects, the analysis is performed on the measurements acquired in the perpendicular plane. All POLDER wavebands are affected by the results of the filtering.

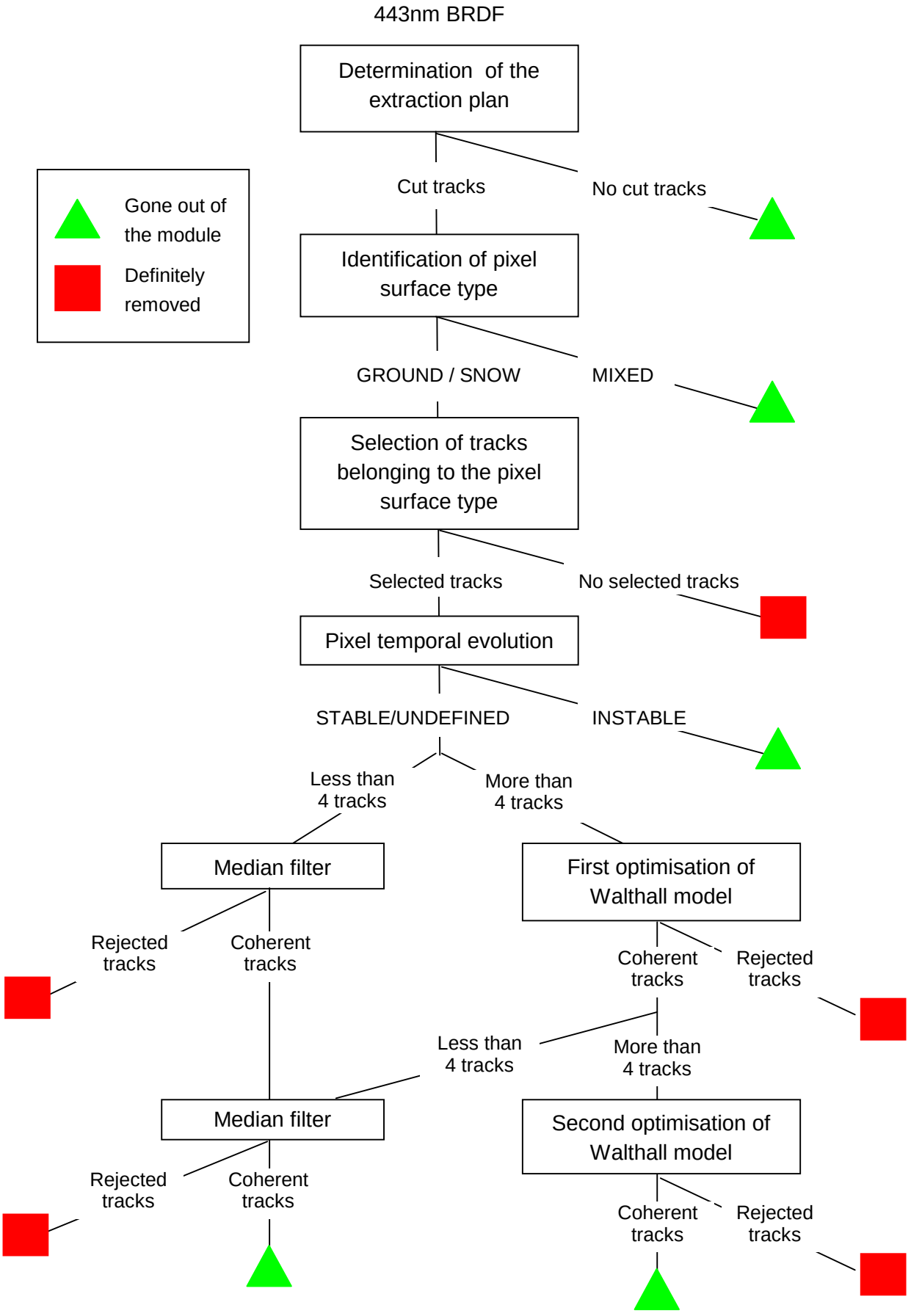

Figure 2 : Functional scheme of the temporal filtering module

The filtering module is applied under the assumption that disturbed acquisitions are few regarding to the whole BRDF measurements, and that the selected acquisition in the track is representative of the whole track. For a given pixel, a track consists of a maximum of 14 observations acquired during an overpass. Moreover, it assumes that the land surface properties are stable during the synthesis period. Then, the main temporal inconsistencies of measurements are due to cloud and/or aerosols.

The filtering module relies on 3 steps according the functional scheme in Figure 2:

1. Selection of the acquisition closest to the perpendicular plane for each POLDER track during the synthesis period.
2. Determination of surface type (ground, snow or mixed) and of its temporal evolution over the synthesis period.
3. Fitting the directional model of Walthall (1985) to remove the noisy measurements.

The first step consists in extracting one representative measurement per track. For that, the algorithm identifies the tracks direction by analysing the viewing azimuth angle evolution on successive observations, which determines the extraction plane: the closest plane to the perpendicular plane that cuts the greatest number of tracks. The no-cut tracks go out of the filtering module. Then, the measurement of each cut track which minimises the angular distance with the extraction plan is selected.

The determination of the surface type is performed using acquisitions during the central 10-day period. Each acquisition is associated with one of the three classes (SNOW, MIXED, GROUND) defined according to the following thresholds:

- SNOW for 443nm reflectance greater than 0.3
- MIXED for 443nm reflectance between 0.2 and 0.3
- GROUND for 443nm reflectance lower than 0.2

The pixel is associated with the majority class. Tracks belonging to the minority classes are definitely removed. If the cardinals of two classes are equal, the pixel is considered as MIXED. The MIXED pixels go out of the filtering module. The temporal evolution of SNOW and GROUND pixels is analysed. If the number of remaining measurements is greater than 6 and are distributed, at least, over a week, a linear relationship is fitted by a least mean square minimisation. For other cases, the temporal evolution of the pixel is UNDEFINED. If the retrieved slope is between –0.05 and 0.05 (R/orbit), the pixel is considered as STABLE over the synthesis period, else it is considered as INSTABLE. The INSTABLE pixels go out of the filtering module.

The third step is applied to SNOW and GROUND pixels whose temporal evolution is STABLE or UNDEFINED. If there are more than 4 remaining measurements, a linear empirical reflectance model (Walthall, 1985) is fitted using a least mean square minimisation procedure. The acquisitions for which the difference between modelled and measured reflectances are larger than 0.025 for a GROUND pixel (0.1 for a SNOW pixel) are definitely removed from for the processing. If the remaining measurements are not numerous enough to invert the Walthall model, the acquisitions that deviate more than 0.1 from the median

reflectance value are considered as noisy and removed. This alternative option is less relevant but can be applied in any cases, especially when a small number of clear tracks are available as in equatorial areas, where it allows to eliminate some residual cloud contamination. A second adjustment is performed under the same conditions of number of remaining measurements than the first one.

2.2. The BRDF model inversion

A new linear semi-empirical BRDF model proposed by Maignan et al. (2004) has been implemented in the Level 3 processing line to normalize bi-directional POLDER measurements. It follows the general formulation (Eq. 1) of the bi-directional reflectance $R(\theta_s, \theta_v, \varphi)$ defined by Roujean et al. (1992):

Eq. 1
$$R(\theta_s,\theta_v,\varphi) = k_0 + k_1 F_1(\theta_s,\theta_v,\varphi) + k_2 F_2(\theta_s,\theta_v,\varphi)$$

where θ_s, θ_v and φ are the solar zenith, view zenith and relative azimuth angles respectively, F_i are a-priori kernels based on either physical or empirical considerations, and k_i are free parameters to be inverted on the measurements.

This model combines the reciprocal geometric kernel of "Li_sparse" (Lucht et al., 2000) (Eq. 2) with the volumic kernel of "Ross_thick" (Roujean et al., 1992) merged with a hotspot module (Bréon et al., 2002). The modified version of volumic kernel (Eq. 3) allows to reproduce accurately the hotspot phenomenon.

Eq. 2
$$F_1 = \frac{m}{\pi}(t - \sin t \cos t - 1) + \frac{1+\cos\xi}{2\cos\theta_s \cos\theta_v}$$
$$\cos t = \frac{2}{m}\sqrt{\Delta^2 + (\tan\theta_s \tan\theta_v \sin\varphi)^2}$$
$$m = \frac{1}{\cos\theta_s} + \frac{1}{\cos\theta_v}$$

Eq. 3
$$F_2(\theta_s,\theta_v,\varphi) = \frac{4}{3\pi}\frac{1}{\cos\theta_s + \cos\theta_v}\left[\left(\frac{\pi}{2} - \xi\right)\cos\xi + \sin\xi\right]\left(1 + \left(1 + \frac{\xi}{\xi_0}\right)^{-1}\right) - \frac{1}{3}$$

where ξ is the phase angle given by $\cos\xi = \cos\theta_s \cos\theta_v + \sin\theta_s \sin\theta_v \cos\varphi$, and ξ_0 is a characteristic angle that can be related to the ratio of scattering element size and the canopy vertical density. ξ_0 is set to 1.5° to avoid the addition of a free parameter in the BRDF modelling. Δ is related to the horizontal distance between the projections of sun and viewing directions:

$$\Delta(\theta_s,\theta_v,\varphi) = \sqrt{\tan^2\theta_s + \tan^2\theta_v - 2\tan\theta_s \tan\theta_v \cos\varphi}$$

A temporal weighting gives more weights to the acquisitions close in time to the centre of the synthesis period. The weighting function is a gaussian curve based on the central track of the synthesis period (Eq. 4). Its standard deviation is equal to half the number of tracks during the synthesis period. The temporal weighting enhances the seasonal variations of hemispherical reflectances and NDVI, then the changes of surface properties are more accurately represented.

Eq. 4

$$W_i = \exp\left(-\frac{1}{2}\left(\frac{t_i - t_c}{hw} \right)^2 \right)$$

W_i is the weight applied to the track *i* of track number t_i, t_c is the track number of the central track of the synthesis period. *hw* is half the number of tracks during the synthesis period.

The model parameters [K] are inverted so as to minimize the root mean square difference between the measurements and the model values. For linear models, this inversion is a simple matrix inversion:

Eq. 5

$$[K] = ([F]^t [F])^{-1} [F]^t [R]$$

where [R] is a *1*x*N* matrix, representing the column vector of the *N* measured weighted reflectances and [F] is a *3*x*N* matrix, representing for each of the *3* kernels the column vector of the weighted kernel values for each of the *N* measurements geometries.

The inversion is carried out in 5 wavebands (443nm, 565nm, 670nm, 765nm, and 865nm). The resulting spectral directional coefficients [K] are:

- a nadir-zenith reflectance, k_0
- a roughness indicator, k_1
- a volume scattering indicator, k_2.

However, because of the correlation between the F_1 et F_2 kernels, the use of the directional coefficients taken independently as surface indicators should be cautious. Their optimal use is as a set of coefficients to accurately simulate the BRDF.

The error associated to each directional coefficients is estimated by the root mean square error (rmse) of the k_i distribution. It is represented by the root square of the diagonal elements of the variance-covariance matrix calculated during the BRDF model inversion. This method is not completely realistic because the directional kernels are not totally independent.

The directional coefficients and their errors are given in the “Directional Parameters” product (Figure 1).

The directional coefficients resulting from the BRDF model inversion are used for computing the spectral Directional Hemispherical Reflectances (DHR) for the median sun angle θ_{s_med} of the synthesis period (Eq. 6).

Eq. 6 $$DHR(\theta_{s\_med}) = k_0 + k_1 * G_1(\theta_{s\_med}) + k_2 * G_2(\theta_{s\_med})$$

where $G_i(\theta_s) = \frac{1}{\pi}\int_\Omega F_i(\theta_s, \theta_v, \varphi)\cos\theta_v d\omega$ is the integration of kernels F_i over the full viewing hemisphere. The integrals are approximated by pre-computed polynomial relationships of θ_s. The associated error on spectral DHR are estimated by Eq. 7 where [COV] is the variance-covariance matrix of the linear regression.

Eq. 7 $$ErrDHR = \sqrt{[G]^t [COV][G]}$$

with

Eq. 8 $$[COV] = \sigma ([F]^t [F]^{-1}) \quad \textbf{with} \quad \sigma = \frac{\|R\|^2 - [K]^t [F]^t [R]}{N - 3}$$

The Normalized Difference Vegetation Index (NDVI), corrected for the directional effects, is derived from DHR_{670nm} and DHR_{865nm} (Eq. 9) , and its error is calculated by Eq. 10.

Eq. 9 $$NDVI = \frac{DHR_{865} - DHR_{670}}{DHR_{865} + DHR_{670}}$$

Eq. 10 $$ErrNDVI = 2 * DHR_{865} * NDVI * \frac{ErrDHR_{865} + ErrDHR_{670}}{(DHR_{865} + DHR_{670})^2}$$

The spectral DHR, the NDVI and their errors are contained in the “Albedo and Vegetation“ product (Figure 1).

2.3. The vegetation model inversion

The Leaf Area Index (LAI) is defined as half the total intercepting green foliage area per unit ground surface area (Chen and Black, 1992). The Fraction of Vegetation Cover (FVC) is defined as the part of the land surface covered by vegetation.

The ADEOS-2/POLDER-2 algorithm computes the LAI using a neural network, which inverts the radiative transfer model of Kuusk (1995) considering the vegetation as a turbid medium of leaves with spherical orientation. This model simulates the simple scattering in the canopy (in particular the hot spot phenomenon quantified by the parameter l*, ratio of the leaf size to the canopy height) following the Nilson and Kuusk (1989) approach, and the multiple scattering according the SAIL model (Verhoef, 1984). Furthermore, the leaf optical properties are described by the PROSPECT model (Jacquemoud et al., 1996) whereas the spectral and angular properties of soil are reproduced by the coupling of the functions of Price (1990) and the directional Walthall (1985) model, respectively.

For the specific application to the POLDER data, parameters of the PROSPECT model have been adjusted to account for the chlorophyll concentration, C_{ab}, the senescent pigments concentration, C_s, the dry matter content, C_{dm}, the water equivalent thickness, C_w, and the effective number of layers inside a leaf, N. More, only director factors, a_1 and $a_{2,}$ of the 2 first functions of Price (1990), which have been optimized, are considered; others are set to 0.

The learning base of the neural network has been produced by sampling LAI [0 - 6.5], C_{ab} [15 - 80µg/cm²], N [1 - 4.5], C_s [0 - 2], a_1 [0.1- 0.8], whereas other parameters are fixed (C_w = 0.01g/cm², C_{dm} = 0.015g/cm², l* = 0.1 and a_2 = 1). The network inputs are a single orbit of 11 directional reflectances in 3 spectral bands (565nm, 670nm, and 865nm) and their angular configurations. The output is the LAI estimated for each POLDER track.

A merging algorithm, based upon the median value of the LAI "track" distribution, computes a monthly value over 30 days. The gaussian temporal weighting described in 2.2 is applied to individual LAI "track" in order to enhance the representation of the central 10-day period. The error on LAI is estimated by the weighted standard deviation of LAI "track" to the monthly value.

The Fraction of Vegetation Cover (FVC) is derived from LAI (Eq. 11) and its error is estimated by Eq. 12:

Eq. 11 $$FVC = 1- \exp (- 0.5 * LAI)$$

Eq. 12 $$ErrFVC = 0.5 * \exp(-0.5 * LAI) * errLAI$$

The method for assessing LAI and FVC errors does not allow an error calculation when only one LAI "track" is available. Furthermore, this method quantifies only the part of error induced by the directional measurements and does not account for the part of error induced by the vegetation model. Now, the error associated to the vegetation model prevails; therefore, the obtained values underestimate the true error on LAI and FVC, especially for ecosystems where there is a bias on the LAI.

3. Products technical features

A physical range is considered for each parameter (Table 1). The directional coefficients don't have a real physical meaning, then their limits have been defined empirically.

The directional coefficients and their errors contained in the "Directional Parameter" product are coded on two-bytes unsigned integer. If the parameter physical value (before coding) is undefined then the parameter is equal to (2^{16}-2 = 65534). If the parameter physical value is larger (lower) than the maximum (minimum) limit of the physical range, the parameter is set to 2^{16}-3 (2^{16}-4).

The DHR, NDVI, LAI, FVC and their errors contained in the "Albedo and Vegetation" product are coded on one-byte unsigned integer. If the parameter physical value (before coding) is undefined then the parameter is set to 254. If the parameter physical value is larger (lower) than the maximum (minimum) limit of the physical range, the parameter is set to 253 (252).

More details about the product format are available in DR1.

Parameter	Physical Range
Directional coefficient k0	[-0.1, 1.2]
Error on k0	[0, 1]
Directional coefficient k1	[-0.3, 0.2]
Error on k1	[0, 0.5]
Directional coefficient k2	[-0.8, 2]
Error on k2	[0, 1.5]
DHR	[0, 1.1]
Error on DHR	[0, 1]
NDVI	[-0.2, 1]
Error on NDVI	[0, 1]
LAI	[0, 8]
Error on LAI	[0, 8]
FVC	[0, 1]
Error on FVC	[0,1]

Table 1 : Physical domain of Land Surface Level-3 parameters

4. Validation

The POLDER-2 land surface products represents the properties of the continental ecosystems. They are useful for weather forecast and climate modelling, water and carbon cycles studies, whose results are partly controlled by the relevance of the input biophysical parameters. Then, they must be validated, first to estimate their accuracy for the user community, and also to provide feedback so that retrieval algorithm can be improved.

4.1. Impact of the filtering module

The filtering module has been tested on ADEOS-1/POLDER-1 data. The inconsistent spatial variability of biophysical parameters over cloudy areas is clearly reduced.

Figure 3 shows this improvement on the Directional Hemispherical Reflectance over the Central Africa. The patchiness over the equatorial forest on no-filtered POLDER-1 product (map at the top) is clearly smoothed and the area appears more homogeneous on the filtered POLDER-1 product (map at the bottom). The decrease of the Directional Hemispherical Reflectance at 670nm over the Southwest of the area is due to the filtering of the bi-directional reflectances contaminated by aerosols of biomass burning.

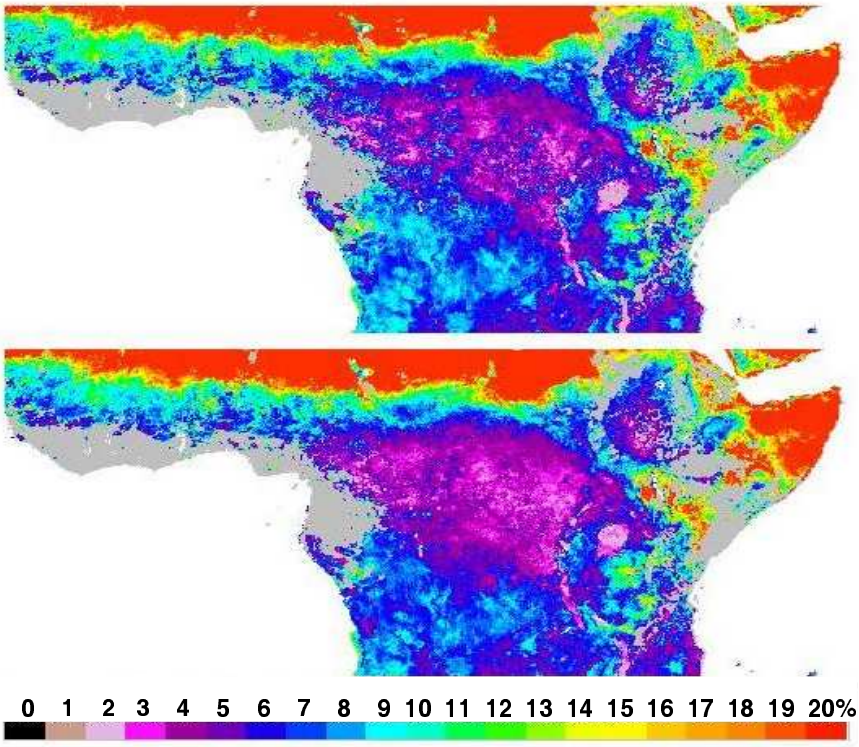

Figure 3 : Directional Hemispherical Reflectance at 670nm on June 15, 1997 generated without the filtering module (top) and using the filtering module (bottom).

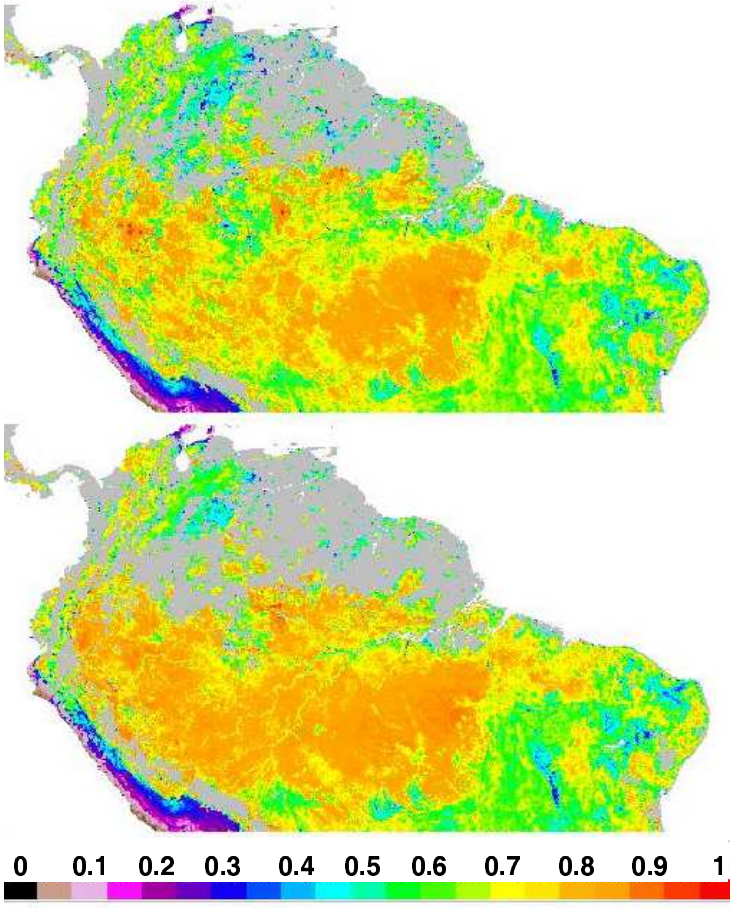

Figure 4 : NDVI on June 25, 1997, generated without the filtering module (top) and using the filtering module (bottom).

The same improvement is obtained on the NDVI. Figure 4 displays maps on the Amazonian forest. The spots of low values on the no-filtered POLDER-1 NDVI (map at the top) disappeared with an increase of the NDVI (map at the bottom). The physical characteristics of the surface, such as rivers, are enhanced. The mapping is more accurate and the patterns can be reasonably linked to true surface structures.

4.2. Improvement brought by the new BRDF model

The Maignan et al. model has been tested on the POLDER-1/ADEOS-1 data, and compared with the results of the Roujean et al. model inversion. The improvement has been shown by a decrease of the rmse between measured and simulated réflectances (Maignan et al., 2004). We note also, for directional coefficients, DHR and NDVI, a large reduction of values outside the physical range. Then, the number of "no-significant" pixels is lower and, consequently, the product quality is better.

Implementing the Maignan et al. model aims at improving the representation of land surface BRDF and its specific features such as the hot spot phenomenon, mainly. However, we note a small impact on the DHR values, because the hot spot phenomenon, which is angularly narrow, is smoothed by the directional integration.

4.3. Validation procedure

The validation procedure will be adapted to each product. Indeed, some of them are structural vegetation properties (LAI, FVC), others depend on the spectral characteristics of the sensor (DHR, NDVI). In the best case, the validation procedure will rely on the following steps:

- Verification of the realism of the products:
    - Analyse of the spatial and temporal distribution of pixels for which parameter values are out of physical range.
    - Analyse of the spatial variability, i.e. the representation of the gradients at the continental scale, and temporal evolution, basically over an annual cycle.
- Comparison with ADEOS-1/POLDER-1 products, when existing, to estimate the improvements brought by the new modules implemented in the advanced ADEOS-2/POLDER-2 algorithms.
- Comparison with available equivalent products derived from other sensors, such as SPOT-5/VEGETATION-2, ENVISAT/MERIS, NOAA/AVHRR, TERRA/MODIS, by similar or different approaches. Note that the 6km resolution of POLDER limits the relevance of comparisons with kilometric or sub-kilometric products.
- Comparison with in-situ measurements: LAI and FVC reference maps are available, produced in the frame of the VALERI (VAlidation of Land European Remote sensing instrument) project. They are elaborated from ground-based measurements and high resolution satellite images.

4.4. Validation results

4.4.1. Verification of the realism of the products

This first step consists in analysing the cases for which the algorithms fail, checking the spatial distribution of parameters at the continental scale, and verifying their temporal profile over an annual cycle.

4.4.1.1 The out-of-range values

The pixels with values out of the physical ranges presented in Table 1 are counted and located, in time and space. These pixels are coded on specific values (§ 3). The statistics are calculated over continental pixels for all wavebands and periods of synthesis. The larger percentages of out-of-range directional coefficients stay very low, under 1%. It seems that the empirical validity ranges defined for coefficients k1 and k2 are appropriate, even if they cannot be linked directly to a physical property of the surface (§ 2.2). They are detected at 443nm, mainly, which is the more sensitive waveband to the atmospheric effects. In the other bands, the number of out-of range DHR values is insignificant, and there is no pixels with NDVI larger than 1. None out-of-range values are obtained for LAI and FVC. The spatial distribution of out-of-range pixels is analysed using the ECOCLIMAP land cover map (Masson et al., 2003, www1). The most of them are located over the classes "Permanent snow and Ice", "Polar tundra" and "Amazonian Forest" where snow and/or water and/or residual clouds, whose directional signature is not well reproduce by the BRDF model, can be found. These results show that the BRDF model is suitable for an application at global scale.

4.4.1.2 Spatial variations of parameters

The quality criterion is the reproduction of vegetation gradients at continental scale due to large worldwide ecosystems. For that, transects along meridians are plotted: along 25° East in Africa from Mediterranean coast to South Africa (Annex1_1 & Annex1_2), along 66.3° West in South America from Caribbean coast to gulf of San Juan in Argentina (Annex1_3 & Annex1_4), along the 30° East in Central Europe from Black Sea to Barents Sea (Annex1_5 & Annex1_6); and along 90° West in North America from gulf of Mexico to Hudson Bay (Annex1_7 & Annex1_8). The main ECOCLIMAP classes are indicated on the graphs.

Maximum DHR in Africa are obtained over the Sahara with quite same values in 670 and 865nm (Annex1_1). It can be noted the variability of soil type, rocks and sand, with high DHR values for the latter and lower values for the former. On each side of the equator line, the inversion of season is well marked on DHR at 865nm. Minimum and maximum values are similar on Sahelian woodland at North and equatorial wooded grassland at South. These profiles display local features such as the arid area of Kalahari around 21° South where a peak of DHR appears. Over equatorial forest, DHR values are realistic: lower than 0.05 at 670nm and around 0.25 in the near infrared, which lead to high values of NDVI. NDVI profiles show large variations in time and space. Seasonal cycle is more marked on the Southern ecosystems than over Sahelian vegetation in Northern Africa. Same general trends appear on LAI and FVC transects (Annex1_2), but the profiles are more irregular than NDVI, especially between 10° South and 5° North. This is likely explained by the fact that the LAI retrieval algorithm is more sensitive to noise on input reflectances than the BRDF algorithm. Nevertheless, the LAI and FVC profiles are realistic with zero over desert, around 5.5 (LAI) and 1 (FVC) on the equatorial forest, and middle values over transitional vegetations. The Kalahari area is also well characterized on LAI and FVC.

DHR transects in South America are in Annex1_3 and Annex1_4. They do not show as much as variability than profiles over Africa. Variations due to inversion of seasons around equator line are reduced because the Amazonian forest is a very stable ecosystem, with DHR and NDVI values similar than those over African equatorial forest. Temporal cycle is noticeable in NDVI over the Brasilian Cerrado. LAI and FVC display alike trends, except over Amazonian forest where a temporal cycle appears. This is a not realistic, and translates a limitation of the LAI retrieval algorithm. The impact on the FVC is lower, values are around 0.85 for an area where the vegetation cover is full.

Both transects over Northern hemisphere go through identical ecosystems: temperate crops and grassland, deciduous forests, conifer forest and, polar tundra at the Northern latitudes. Graphs of DHR (Annex1_5 & Annex1_7) present many similarities: lack of data during winter months over boreal regions, high DHR over snowy areas, regular profiles in summer with maximum values around 0.1 at 670nm and between 0.2 and 0.4 in NIR. NDVI profiles (Annex1_5 & Annex1_7) display more variability in North America where ecosystems are more various and clearly delimited. NDVI, LAI et FVC (Annex1_6 & Annex1_8) present clear temporal cycle over deciduous forests and crops. Over boreal taïga, the summer LAI is around 2.5 in Europe, and 1.5 in America. These low values result from a limitation of the retrieval algorithm: the radiative transfer model used to learn the neural network assumes a random distribution of foliage elements, what is not true for clumped vegetation as conifer forests.

4.4.1.3 Temporal variations of parameters

The seasonal variations of biophysical parameters over an annual cycle is another criterion of quality. Annex2 contains temporal graphs of DHR, NDVI, LAI and FVC for 18 sites, chosen as representatives of the main continental biomes. To cover a full vegetative cycle, POLDER-1 (November 1996-June 1997) and POLDER-2 (April – October 2003) products are plotted.

The development of vegetation is well reproduced: the POLDER-2 products “fill the gap” between the spring and the winter POLDER-1 products, consistently. Over common weeks, the overlap is quite good, considering the non-concomitance of observations and the very specific character of year 2003.

The temporal evolution of DHR is satisfactory: profiles are regular, with a decrease of DHR 670nm and an increase of DHR 865nm at the full development of vegetation, and the snowy and snow-melting periods are well marked on the Northern sites (Arctic tundra, Deciduous Forest). The vegetative cycle is well represented on NDVI graphs, and we can note an early start of vegetation growth in 2003 in temperate regions (Annex2_3). The same trend is displayed on LAI and FVC profiles (Annex2_4 and Annex2_5). However, they are more irregular because of the instability of the retrieval algorithm. This limitation appears clearly on the “Semi-deciduous rain forest “ site located in Central Africa where the low values of LAI and FVC are due to undetected residual clouds.

Annex 3 presents maps of LAI for the central 10-day periods of each month from April to October 2003. The seasonal variation of vegetation at continental scale is clearly displayed. Over the South hemisphere, the dry season is marked with the decrease of the LAI in Southern Africa (Annex3_1) and in South America (Annex3_2). In the same way, the vegetation growth can be followed in spring and summer over the Northern hemisphere, with the crops in Central Europe (Annex3_3) and the deciduous forests in the East coast of USA (Annex3_4).

These graphs and maps show that POLDER-2 biophysical parameters present realistic spatial and temporal variations, considering the pre-known characteristics of ecosystems and period of observations.

4.4.2. Comparison POLDER-2 / POLDER-1 products

Common synthesis periods between POLDER-1 and POLDER-2 products are from 15 April to 15 June, even if the years are different: 1997 for POLDER-1 and 2003 for POLDER-2.

To complement the seasonal profiles analysed in the previous section, Annex4 presents temporal evolution of DHR 670nm and 865nm over desertic sites, which are very stable targets. Graphs show that POLDER-2 DHR are higher than POLDER-1 DHR, even if the differences are very low. Maps on Annex4_2 and Annex4_4 gives the spatial distribution of these differences. The ratio POLDER-1/POLDER-2 maps is generally less than 1 over Sahara. The mean values agree with the calibration ratio equal to 0.96 at 670nm and 0.94 at 865nm (Ruffel et al., 2004). The temporal trends are consistent and the POLDER-2 values "fill the gap" well between June and November of POLDER-1 acquisitions.

Comparisons of LAI over Africa and South America reveal that POLDER-2 values are higher over equatorial rain forest (Annex4_5 & Annex4_6). This is an improvement because POLDER-1 LAI was likely too low for such ecosystem. This difference is not due to variations of the surface because such biome is very stable. It seems that the neural network used to retrieve LAI gives better results with POLDER-2 acquisitions. Over temperate areas (Annex4_7 & Annex4_8), the maps show that the northern vegetation growth was early in 2003. This feature has been already put on view in the previous section on temporal profiles. On the Africa maps (Annex4_5), the effect of the drought in Southern Africa in 2003 is clearly noticeable with a lower LAI on POLDER-2 product.

4.4.3.Comparison POLDER-2 / MODIS products

During the POLDER-2 acquisition period, MODIS products are available. Then, the albedo and LAI derived from the two sensors can be compared.

4.4.3.1. Comparison of POLDER-2 DHR with MODIS Black-Sky Albedo

The MODIS product MOD43C1 is provided in a regular lat/lon grid at 0.05° of resolution. The POLDER DHR are re-sampled in the same grid to perform the comparison. The DHR 565nm, 670nm and 865nm are related to BSA b4 (545-565nm), b1 (620-670nm), and b2 (841-876nm), respectively. The BSA are retrieved from the inversion of the RossThick_LiSparseReciprocal model (the same that the one used in the POLDER algorithm but without the hotspot module) for the average of local noon sun angle over the 16 days of the synthesis period. The sliding window is also equal to 16 days, then there is no overlap between synthesis (Schaaf et al., 2002).

The difference in length of synthesis period is a limitation to the comparison, especially in spring and autumn when the surface conditions change quickly. This is not the case over desert which are very stable targets (Annex5_1, Annex5_2 & Annex5_3). The comparison is carried out using temporal profiles over the common 7 months of acquisitions. Over desert sites, graphs show a good agreement, both in seasonal trend and reflectance level. At 565nm and 670nm, POLDER-2 DHR are higher than MODIS BSA, which is coherent with the differences in waveband. At 865nm POLDER-2 DHR is quite equal or slightly lower than MODIS BSA, since the POLDER-2 NIR wavelength is included in the MODIS b4 waveband.

Over some sites, MODIS profiles exhibit sudden decrease of BSA, which could be due to an undetected aerosol event. Then, the POLDER-2 profiles are more regular than MODIS BSA variations. Figure 5 confirms the good agreement between POLDER-2 DHR and MODIS BSA with R^2 equal to 0.984 and a rmse equal to 0.018. Over continental biomes where seasonal variations are sharp, profiles are in a general good agreement: trends and absolute values are similar (Annex5_4, Annex5_5, Annex5_6). However, at opposite than over desert sites, the POLDER-2 DHR profiles look more irregular than MODIS BSA variations. Like on the desert sites, the deviation between POLDER-2 DHR and MODIS BSA values are maximum in the visible bands, and very low in the near infrared.

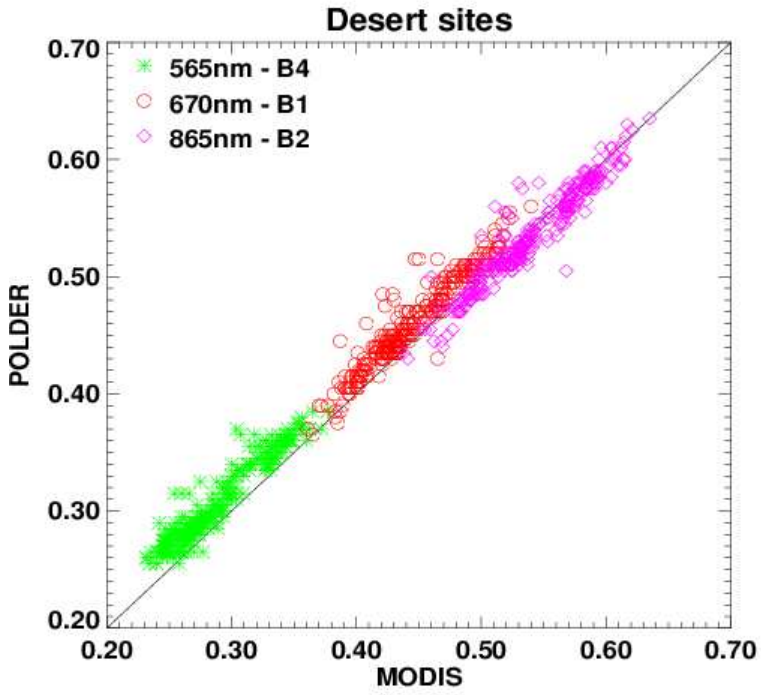

Figure 5 : Scatterplot of POLDER-2 DHR and MODIS BSA over desert sites.

4.4.3.2. Comparison of POLDER-2 LAI with MODIS LAI

The monthly MODIS LAI product at 4km resolution provided by the Boston University is used for this analysis. It is compared with the nearest neighbour POLDER pixel, for the synthesis period centred on the 15th of each month.

The main MODIS LAI algorithm is based on the inversion, using a LUT, of a 3D radiative transfer model which depend on the vegetation structure (Knyazikhin et al., 1998). If this algorithm fails, a back-up procedure is applied to assess LAI by empirical relationships with vegetation indices (Myneni et al., 1997).

Annex5_7, Annex5_8, Annex5_9, and Annex5_10 display the spatial differences of POLDER-2 and MODIS LAI. Over Africa (Annex5_7), MODIS LAI is higher both on equatorial forest where values reach 7, and on woodland and shrubland of Southern Africa. This creates a smoother gradient of vegetation on MODIS LAI. A vegetative cycle is noticeable on MODIS LAI over the northern part of equatorial forest that doesn't appear on POLDER-2 LAI. Over South America (Annex5_8), MODIS LAI is higher than POLDER LAI over Amazonia, but lower over the Brazilian woodlands and Argentinean grasslands, which enhances the Northwest-Southeast gradient of vegetation. Over France (Annex5_9), the

opposite trend appear: POLDER-2 LAI is higher than MODIS LAI with difference larger than 2. Over North America (Annex5_10), there is no general tendency: MODIS LAI is higher on boreal forest where the POLDER algorithm doesn't work well because the model used to learn the neural network doesn't account for the vegetation clumping; South to the Great Lakes, the difference is very large in summer, with MODIS LAI around 2.8 whereas POLDER-2 LAI reaches 5. This discrepancy is unexplained.

The comparison of POLDER-2, MODIS and in-situ LAI is presented in the next section.

4.4.4. Comparison with in-situ measurements

The VALERI program aims to set up a worldwide network of validation sites and to develop experimental methodologies to measure biophysical parameters of the vegetation at spatial and temporal scales fitted to the comparison with satellite products.

From April to October 2003, 6 sites have been instrumented (Table 2). The measurements collected in 2002 over the Counami rain forest are also used because of the great stability of this ecosystem. In-situ LAI and FVC are assessed from gap fraction extracted from hemispherical photographs. Transfer functions are established between ground LAI and FVC, and SPOT reflectances. The presentation of sites, the description of measurement protocol and sampling strategy, and the reports of in-situ data processing method to produce reference map are available in various documents on the VALERI web site (www2).

Site name	**Vegetation type**	**Campaign date**
Turco, Bolivia	Barren & sparsely vegetated	April 2003
Fundulea, Romania	Cropland	May 2003
Barrax, Spain	Cropland	July 2003
Jarvselja, Estonia	Mixed forest	July 2003
Hirsikangas, Finland	Needle leaf forest	August 2003
Larose, Canada	Mixed forest	August 2003
Counami, French Guyana	Evergreen broadleaf forest	October 2002

Table 2 : List of VALERI sites used for the POLDER-2 validation

For the specific POLDER-2 validation, the transfer functions established for each site over the 3km x 3km instrumented area have been up-scaled to the whole SPOT image. Thus, many POLDER pixels can be fully covered by the reference map. The latitude/longitude of the center of POLDER pixel is used to extract the MODIS LAI from monthly products at 4km resolution.

The reference maps are presented in Annex6. Turco is an homogeneous flat area of low and sparse grassland and shrubs (Annex6_1 & Annex6_2). The LAI and FVC values are very low, with maximum values around 0.15 for LAI and 0.2 for FVC. Fundulea and Barrax are cropland areas, in Romania and Spain, respectively. Both sites display well delimited fields, with various species (cereals, sunflower, peas, alfalfa, grassland, etc..), and large bare soil areas. This make an heterogeneous landscape with a large range of LAI and FVC

values. Maximum LAI and FVC are larger over Barrax (Annex6_5 & Annex6_6) than over Fundulea (Annex6_3 & Annex6_4). Jarvselja and Hirsikangas sites are boreal forests. In Estonia, the area is mostly covered by a mixed forest of different age, including both conifers (pines and spruce) and deciduous (birch, aspen, alder); unmanaged open areas are also found. In Finland, the site is a 90% forested area dominated by Scots pine, the rest consists of agricultural fields, peat production area and small water bodies. Maps over Jarvselja show an homogeneous landscape with LAI close to 6 and FVC around 0.8 (Annex6_7 & Annex6_8). LAI map over Hirsikangas show more heterogeneous landscape with a large range of values (Annex6_9) whereas the FVC is very close to 1 (Annex6_10). Larose site is a mixed forest of conifer and deciduous trees, mainly, with some grassland, shrubland and wetlands. Underwood of dense shrubs is present on deciduous trees plots. LAI and FVC values reach 5 (Annex6_11) and 0.8 (Annex6_12), respectively. Finally, we use the measurements made in the Counami tropical rain forest in French Guyana. It is a very dense and homogeneous site characterized by the mean values of ground measurements: 4.39 for LAI, 0.85 for FVC. No maps have been produced.

The VALERI LAI and FVC values are compared with POLDER-2 and MODIS products (Annex6_13 & Annex6_14). The heterogeneity of sites is translated by the length of error bar on VALERI data. Graphs show a good agreement between satellite products and VALERI LAI over Barrax and Fundulea. If POLDER-2 and MODIS LAI display the same trend over these cropland sites, the maximum values are different, POLDER-2 LAI being larger than MODIS LAI. Over the Larose forest, satellite products give quite same LAI, larger than VALERI values, around 2 or 2.5, which seems low for a dense mixed forest in summer. This can be partly explained by the fact that the ground measurements have been made above the underwood. POLDER-2 and MODIS present similar profiles over Finland and Estonia. Over Hirsikangas, MODIS LAI is larger than POLDER-2 LAI, which is closer to VALERI LAI. Over Jarvselja, the agreement is good between satellite and reference LAIs. VALERI LAI over Turco is very low and the satellite products are both higher, even if POLDER-2 product is closer to VALERI values than MODIS. Over the Counami tropical forest, the agreement is very good between satellite LAI and ground measurements. However, the POLDER-2 product display a vegetative cycle (values from 2.5 to 5) which is not coherent for such stable ecosystem. The MODIS profile seems more realistic with values around 5, except for sudden decrease due likely to failure of cloud detection.

Same comments can be done for FVC comparison: a good agreement for cropland sites, boreal and tropical forests; small difference over Turco and a large discrepancy over Larose.

This comparison reveals a good general agreement between POLDER-2 and VALERI LAI and FVC. However, it is too restricted in time and space to conclude clearly on the POLDER-2 quality. For example, although the good matching is obtained over tropical forest for the date of ground measurement, the seasonal cycle of POLDER-2 product is not realistic. For changing ecosystems as crops or forests, ground measurements at various stages of development would be very useful for such validation process.

4.4.5. Conclusion

The results of validation demonstrate an overall good quality of POLDER-2 biophysical parameters. At global scale, the out-of-range pixels are negligible and located over surfaces whose characteristics limit the performance of models. The continental gradients of vegetation and the seasonal variations are realistic according to the pre-known information of the ecosystems. A good coherence is obtained between POLDER-2 and POLDER-1

products, as POLDER-2 values “fill the gap” between spring and winter POLDER-1 values, in spite of the shift in acquisition year. MODIS and POLDER-2 albedo are consistent according to the difference in wavebands. If LAI products displays similar trends, high differences on maximum values are observed locally, some of them cannot be explained by the limits of algorithms. The comparisons with ground VALERI data are cheerful but the points are too sparse in time and space to perform a solid analysis and to conclude beyond all doubt.

At final, the POLDER-2 biophysical parameters represent the surface properties in a consistent way, even if some defaults are identified, such as a too low LAI over coniferous boreal forest. Thus, in spite of only 7 months are available, they can be useful input for environmental studies.

The POLDER-2 algorithms serve as basis for implementing operational lines to process POLDER-3 data onboard the micro-satellite PARASOL, and which are acquired since April 2005.

5. References

DR1 : POLDER Level-3 Products, Data Format and User Manual, Ed.3, Rev.3, January 26th, 2004.

Bréon, F.M., F. Maignan, M. Leroy and I. Grant, Analysis of hot spot directional signatures measured from space. *Journal of Geophysical Research, 107 (16), 4,282-4,296,* 2002.

Chen, J. M. and T. A. Black, Defining leaf area index for non-flat leaves, *Plant, Cell and Environment, 15, 421-429,* 1992.

Jacquemoud, S., S. L. Ustin, J. Verdebout, G. Scmuck, G. Andreoli and B. Hosgood, Estimating leaf biochemistry using the PROSPECT leaf optical properties model, *Remote Sensing of Environment, 56, 194-202*, 1996.

Knyazikhin, Y, J.V. Martonchik, R.B. Myneni, D.J. Diner, and S.W. Running, Synergetic algorithm for estimating vegetation canopy leaf area index and fraction of absorbed photosynthetically active radiation from MODIS and MISR data, *Journal of Geophysical Research, 103, 32,257-32,27,* 1998.

Kuusk, A., A fast invertible canopy reflectance model, *Remote Sensing of Environment, 51: 342-350,* 1995.

Lucht, W., C. Barker Schaaf and A. Strahler, An algorithm for the retrieval of albedo from space using semi-empirical BRDF models, *IEEE Transactions on Geoscience and Remote Sensing, 38, 977-988,* 2000.

Maignan, F., F.M. Bréon and R. Lacaze, Bi-directional reflectance of Earth targets : evaluation of analytical models using a large set of spaceborne measurements with emphasis on the Hot Spot, *Remote Sensing of Environment, 90, 210-220,* 2004.

Masson, V., J.L. Champeaux, F. Chauvin, C. Mériguet et R. Lacaze, A global database of land surface parameters at 1-km resolution in meteorological and climate models, *Journal of Climate, 16, 1261-1282*, 2003.

Myneni, R.B., R.R. Nemani, and S.W. Running, Estimation of global leaf area index and absorbed PAR using radiative transfer models, *IEEE Transactions on Geoscience and Remote Sensing, 35, 1380-1393,* 1997.

Nilson, T. and A. Kuusk, A reflectance model for the homogeneous plant canopy and its inversion, *Remote Sensing of Environment*, *27: 157-167,* 1989.

Price, J. C., On the information content of soil reflectance spectra, *Remote Sensing of Environment*, 33: 113-121, 1990.

Roujean, J. L., M. Leroy and P. Y. Deschamps, A bi-directional reflectance model of the Earth' s surface for the correction of remote sensing data,*Journal of Geophysical Research, 97, D18, 20,455-20,468,* 1992.

Ruffel, C., B. Lafrance, et B. Fougnie, POLDER-1 : Mise à jour de l'étalonnage radiométrique, *CNES, Ed.2, Rev.0,* 23 June 2004.

Schaaf, C.B., et al., First operational BRDF, albedo nadir reflectance products from MODIS, *Remote Sensing of Environment, 83, 135-148,* 2002.

Verhoef, W., Light scattering by leaf layers with application to canopy reflectance modelling: the SAIL model, *Remote Sensing of Environment,* 16: 125-141, 1984.

Walthall, C. L., J. M. Norman, J. M. Welles, G. Campbell and B. L. Blad, Simple equation to approximate the bi-directional reflectance from vegetative canopies and bare soil surfaces, *Applied Optics,* 24, 383-387, 1985.

www1 : http://www.cnrm.meteo.fr/gmme/PROJETS/ECOCLIMAP/page_ecoclimap.htm

www2 : http://www.avignon.inra.fr/valeri/

6. Acknowledgement

Development of the "Land Surface" Level 3 algorithms results from a collaboration between Noveltis and the Centre d'Etudes Spatiales de la BIOsphère (CESBIO). It has been supported by Centre National d'Etudes Spatiales (CNES). The validation of the ADEOS-2/POLDER-2 products is carried out by MEDIAS-France.

This manual is based upon technical documents provided by Noveltis and MEDIAS-France.

The ADEOS-2/POLDER-2 products are available for ordering through the CNES web site at the following address: http://polder.cnes.fr.

For any question, please contact: roselyne.lacaze@medias.cnes.fr

Annex 1 : Spatial distribution of biophysical parameters

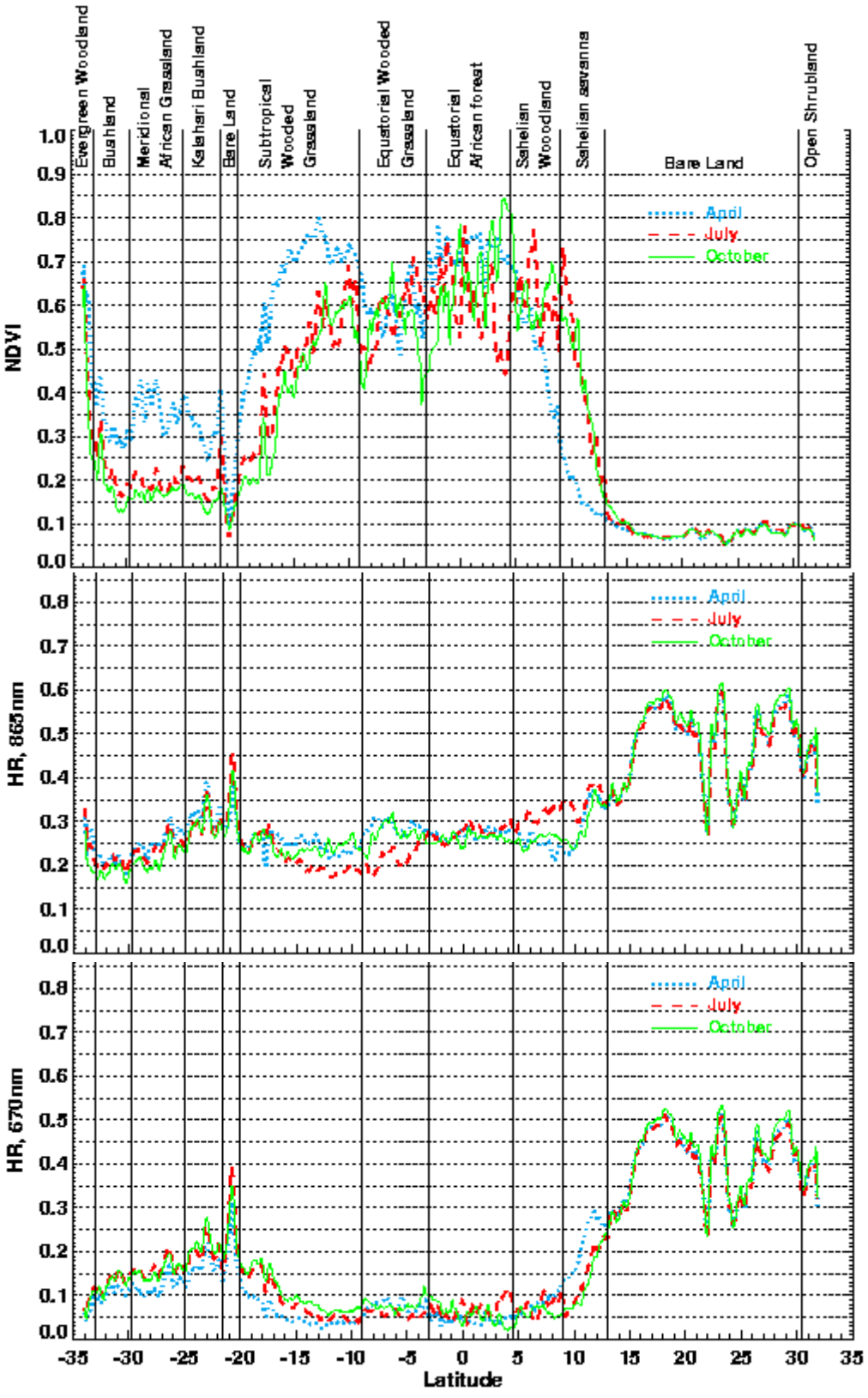

Annex1 1 : Spatial distribution of DHR 670, 865nm and NDVI along 25° East in Africa

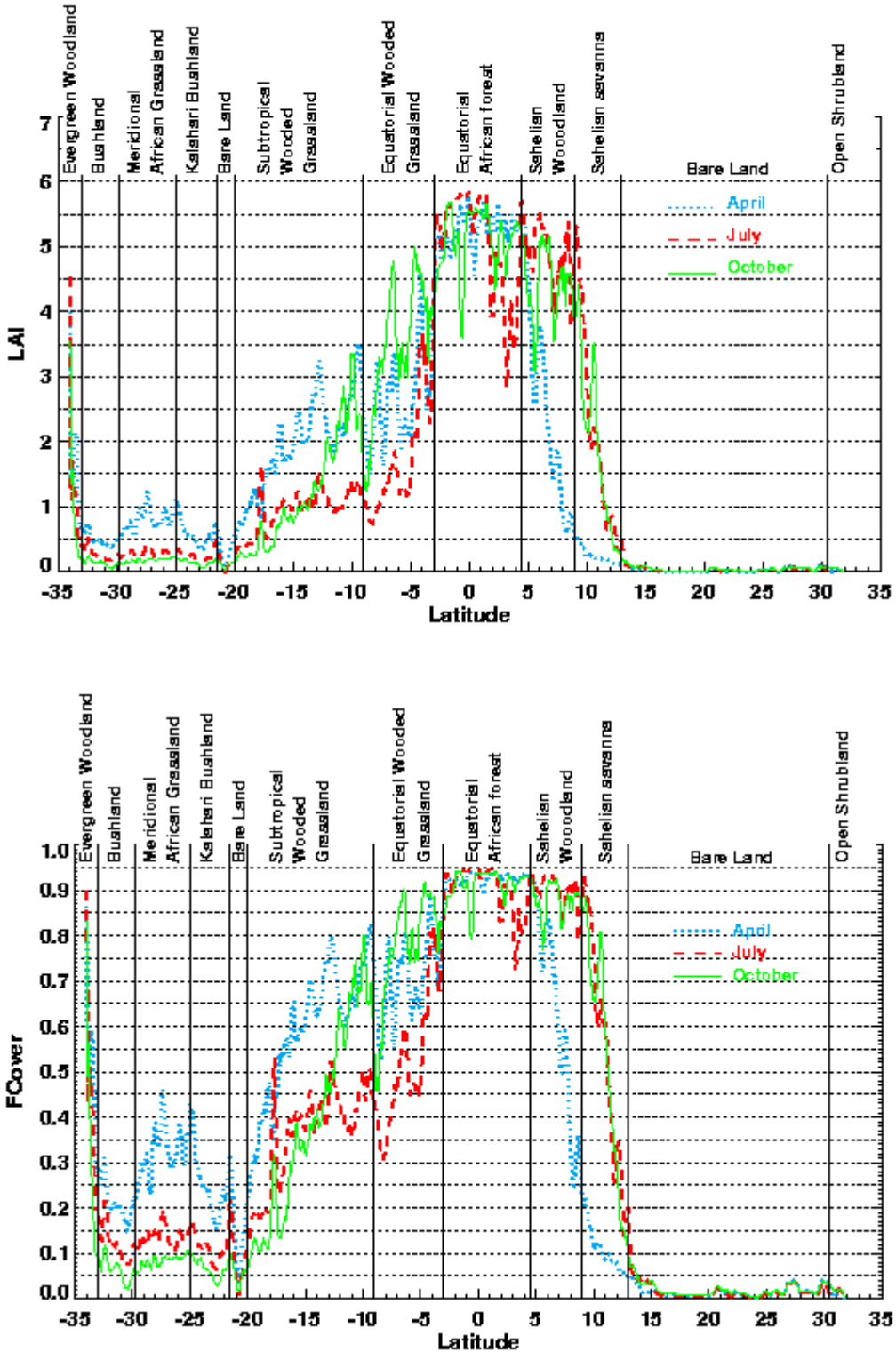

Annex1 2 : Spatial distribution of LAI and FVC along 25° East in Africa

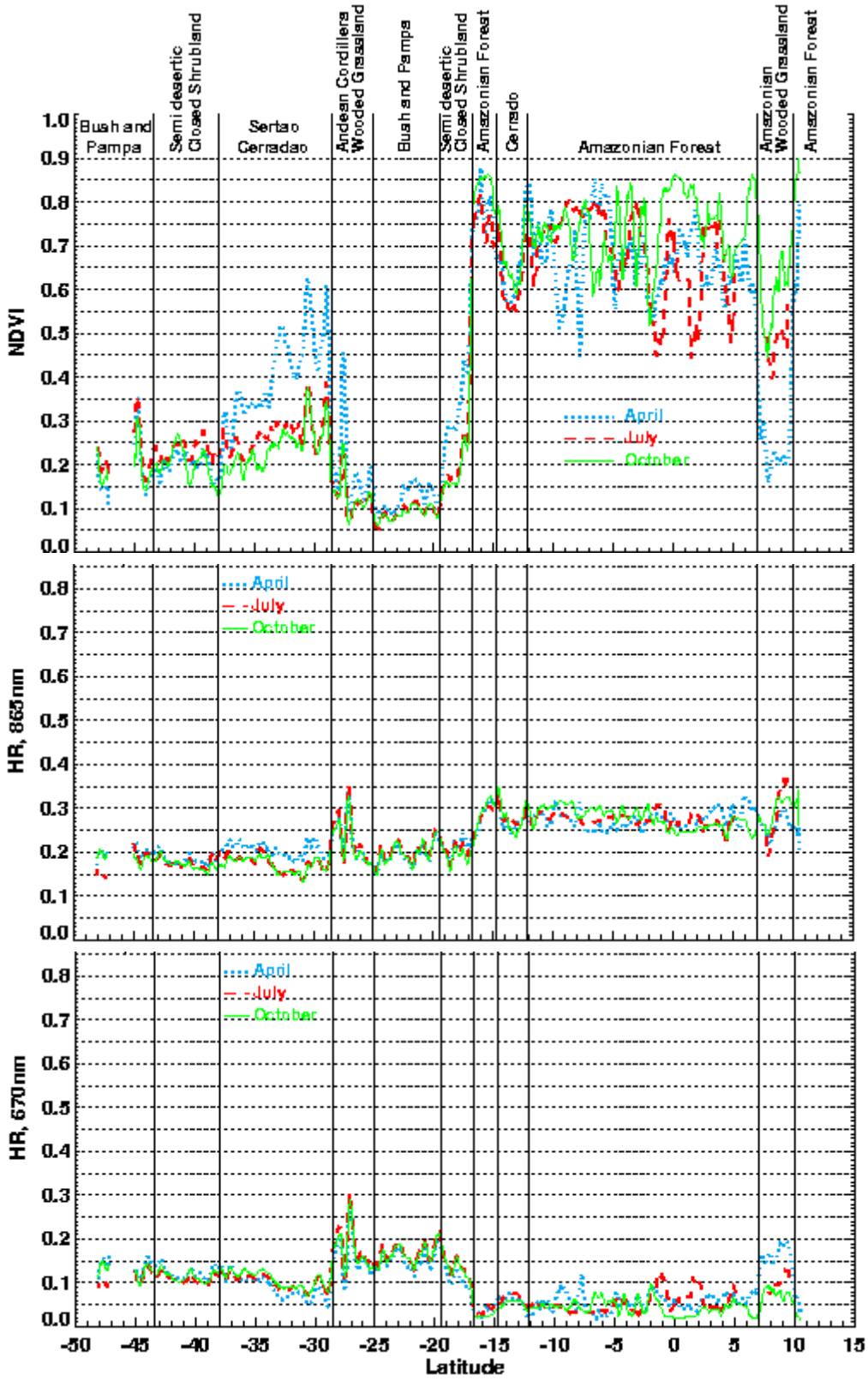

Annex1 3 : Spatial distribution of DHR 670, 865nm and NDVI along 66.3° West in South America.

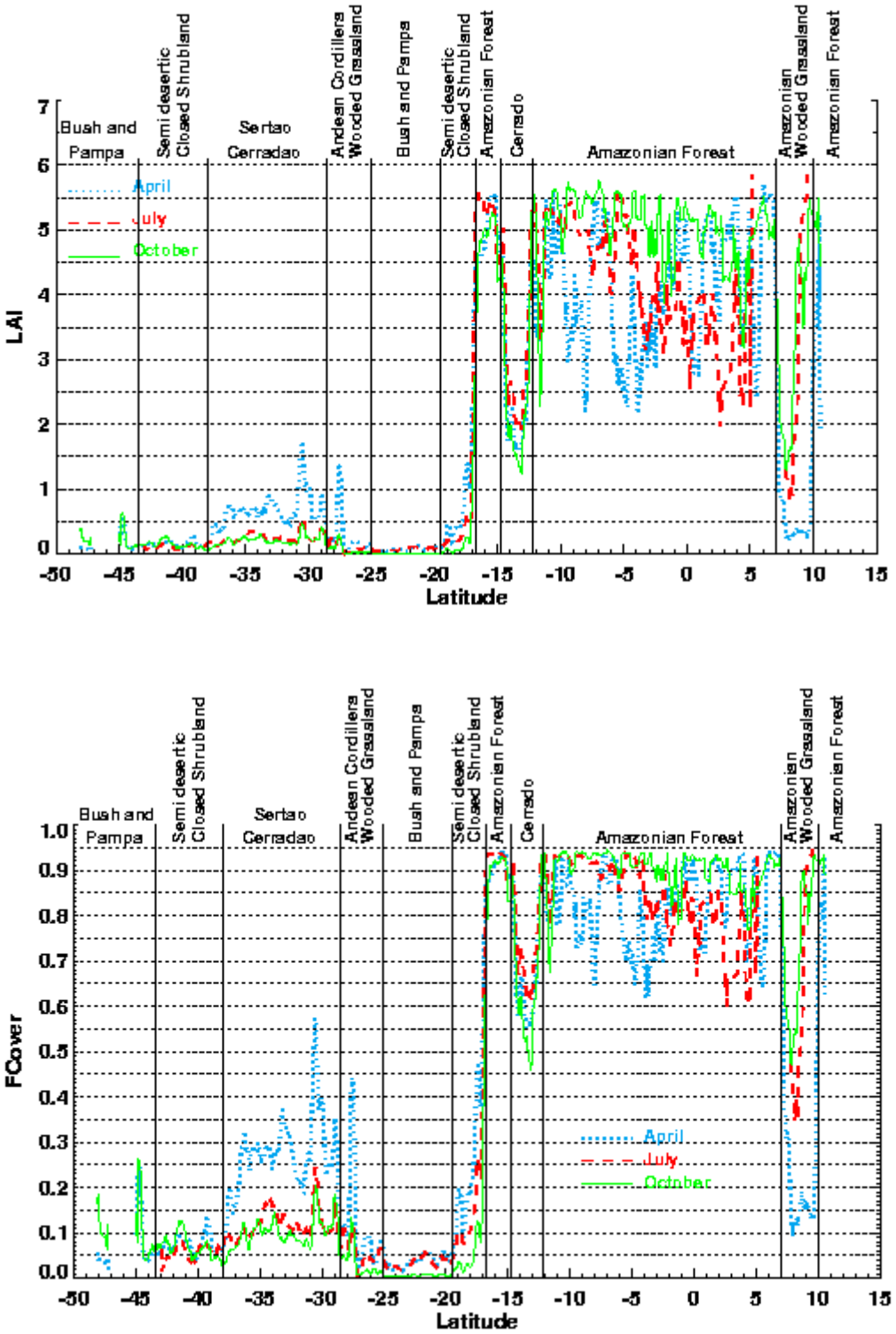

Annex1 4 : Spatial distribution of LAI and FVC along 66.3° West in South America.

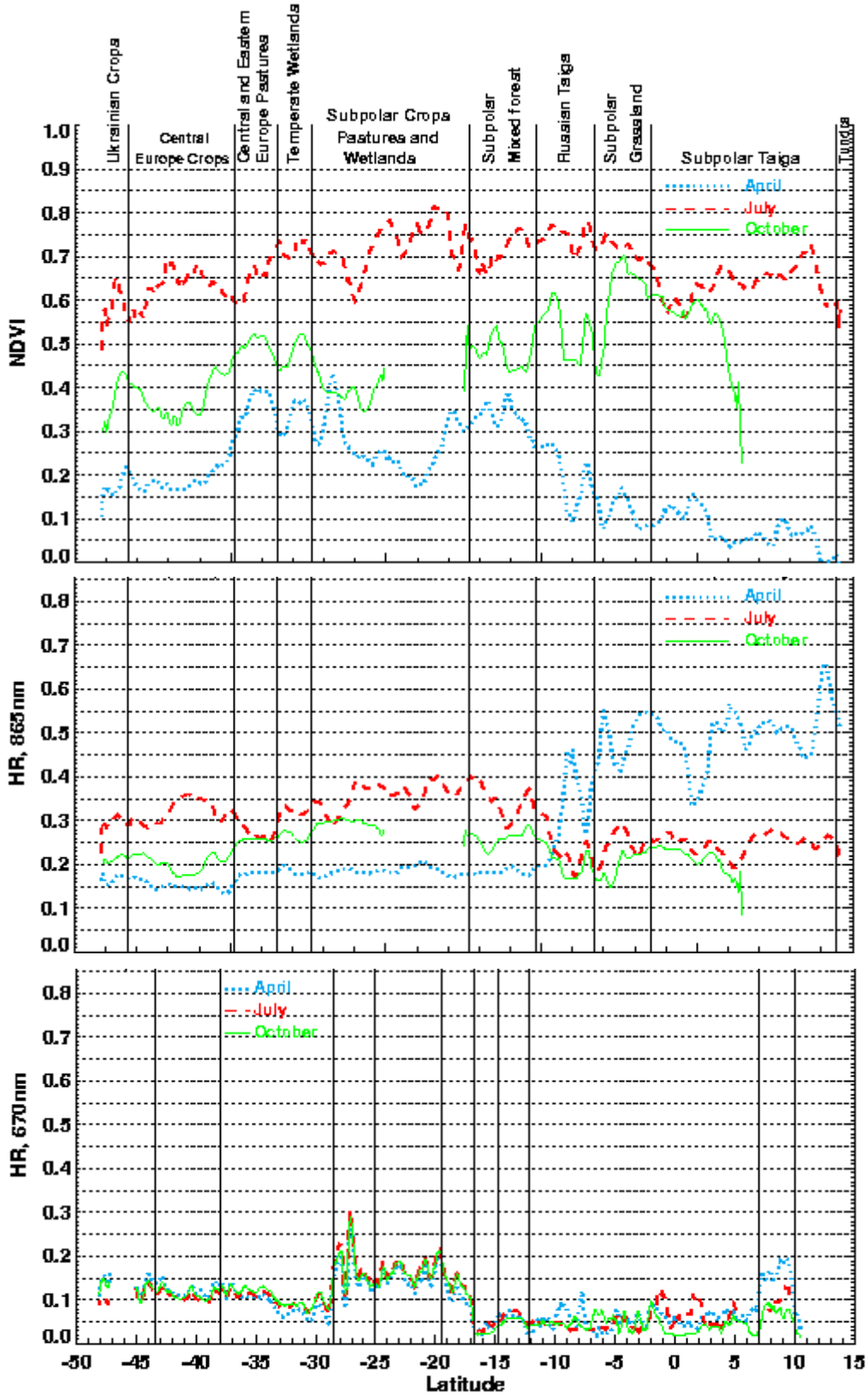

Annex1 5 : Spatial distribution of DHR 670, 865 nm and NDVI along 30° East in Central Europe.

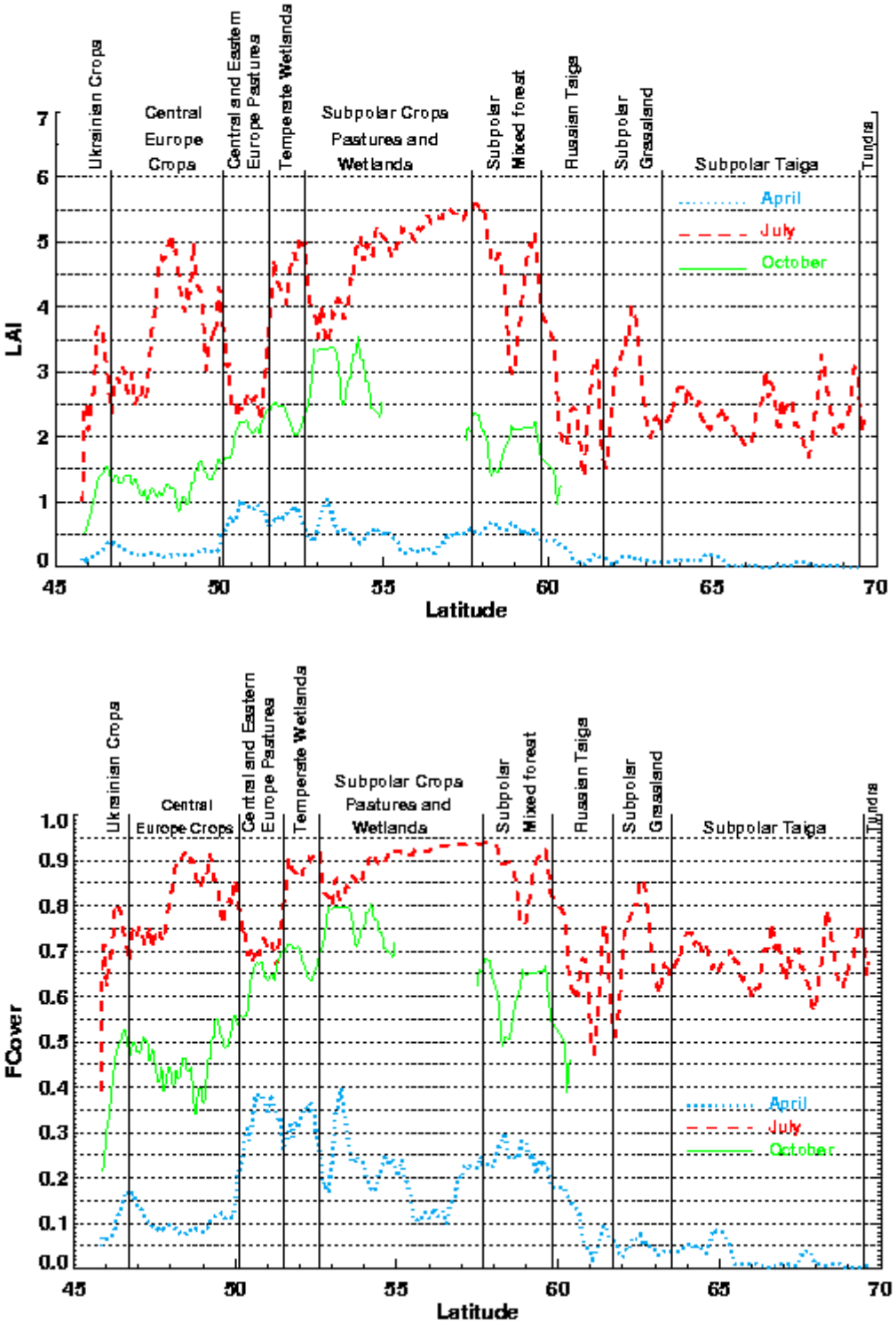

Annex1 6 : Spatial distribution of LAI and FVC along 30° East in Central Europe.

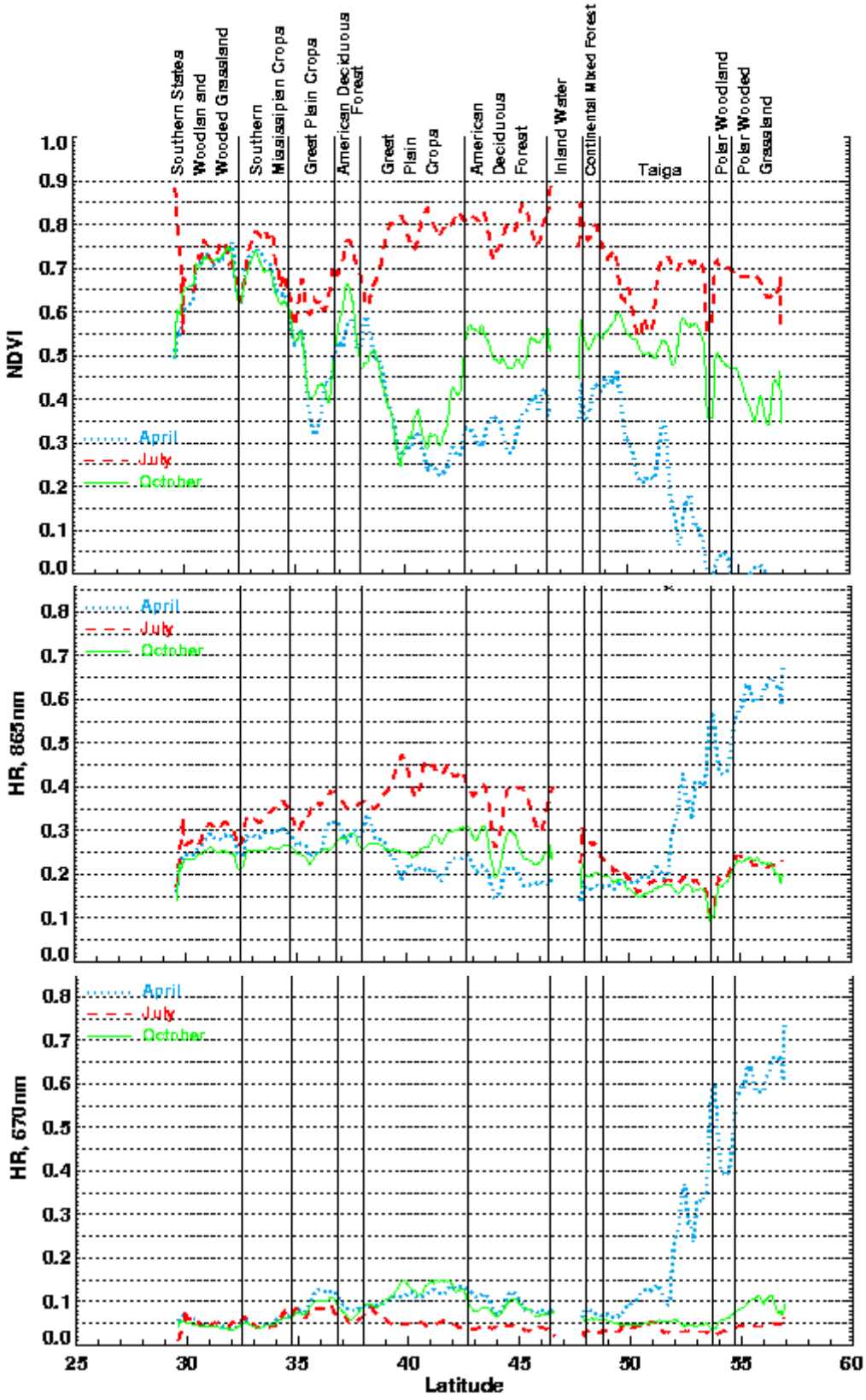

Annex1 7 : Spatial distribution of DHR 670, 865nm and NDVI along 90° West in North America.

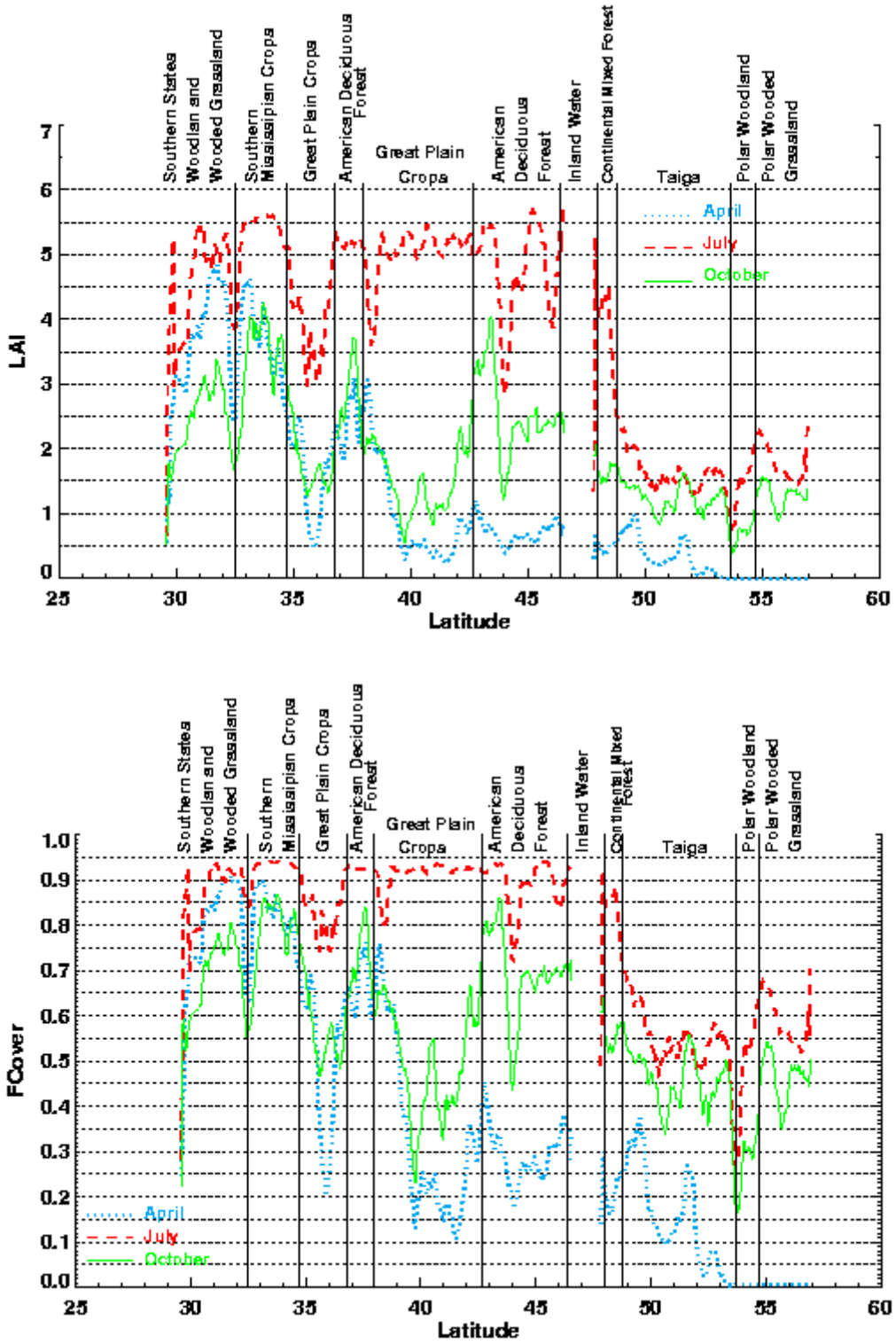

Annex1 8 : Spatial distribution of LAI and FVC along 90° West in North America.

Annex 2 : Temporal variations of biophysical parameters

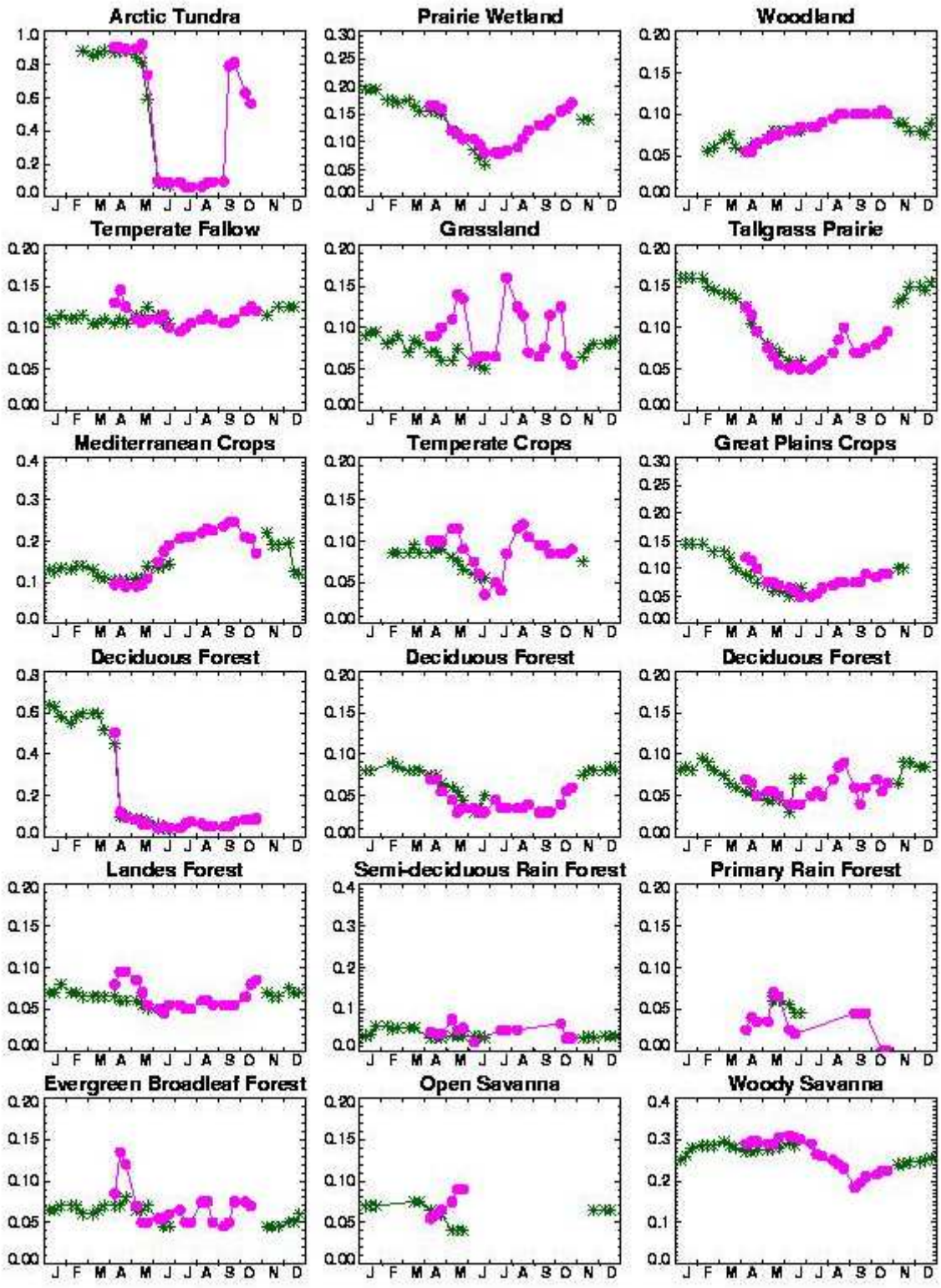

Annex2 1 : Temporal profile of DHR 670nm over an annual cycle

(POLDER-1: green; POLDER-2: magenta)

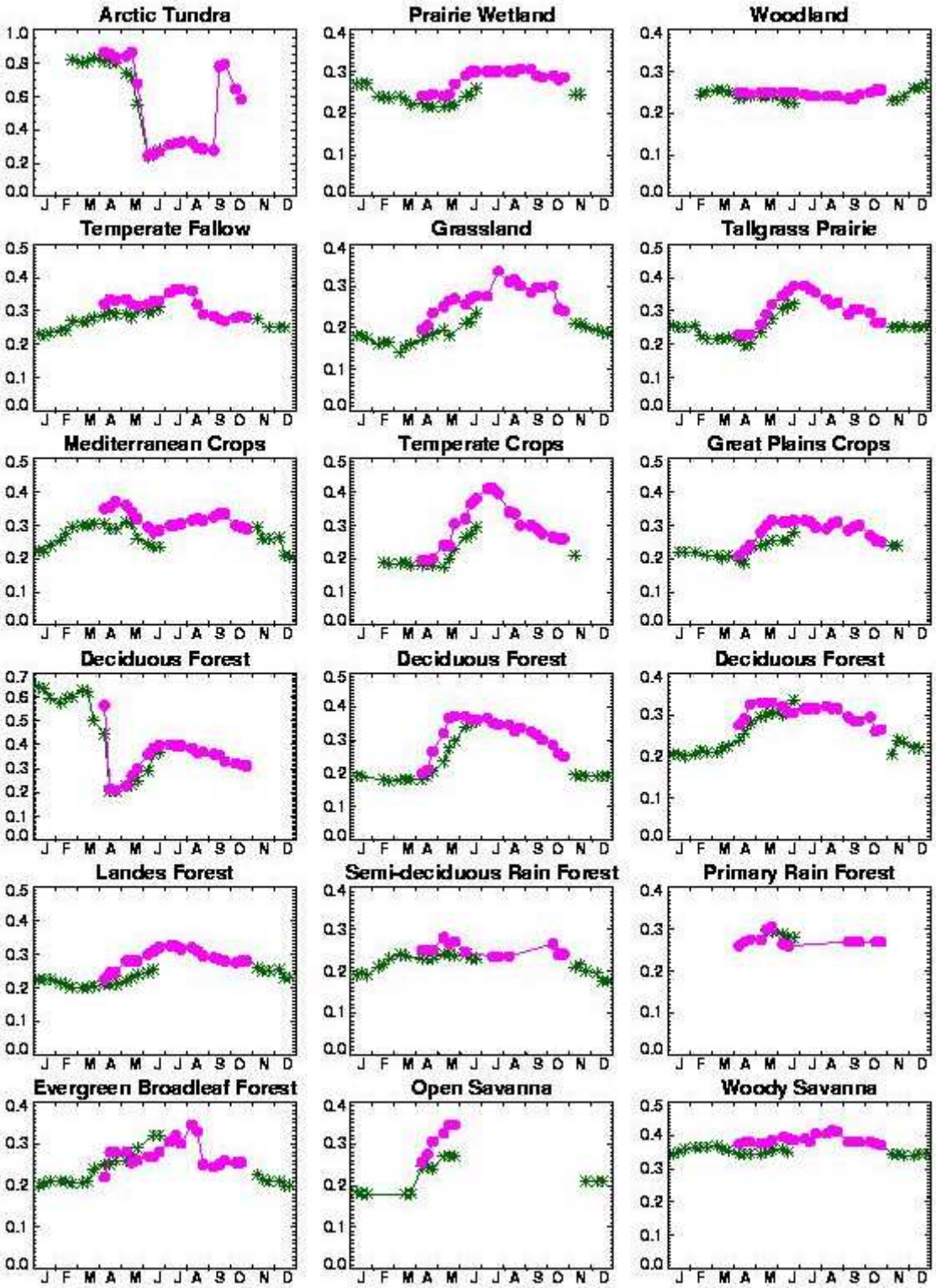

Annex2 2 : Temporal profiles of DH5 865nm over an annual cycle.

(POLDER-1: green; POLDER-2: magenta)

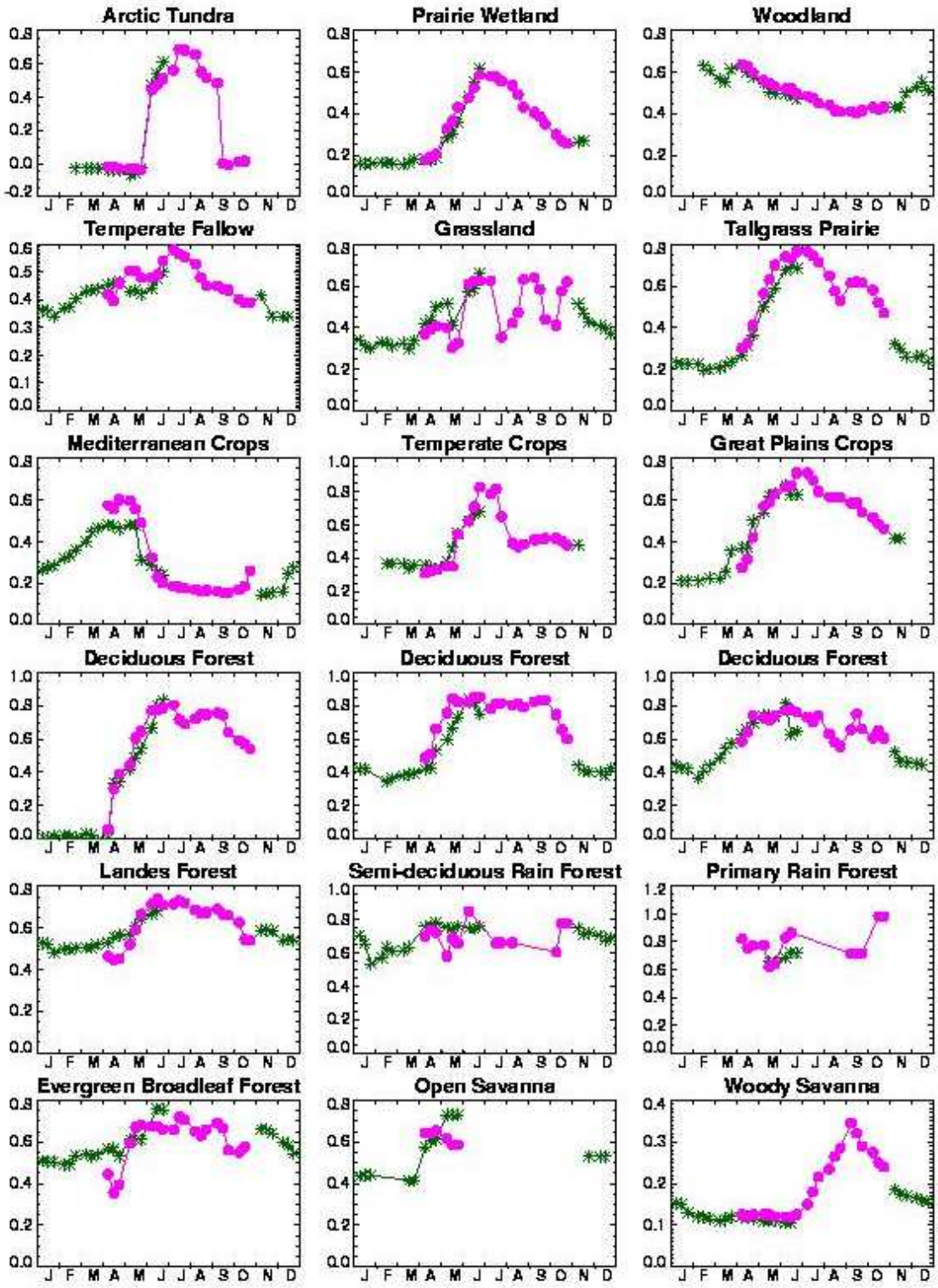

Annex2 3 :Temporal profiles of NDVI over an annual cycle

(POLDER-1: green; POLDER-2: magenta)

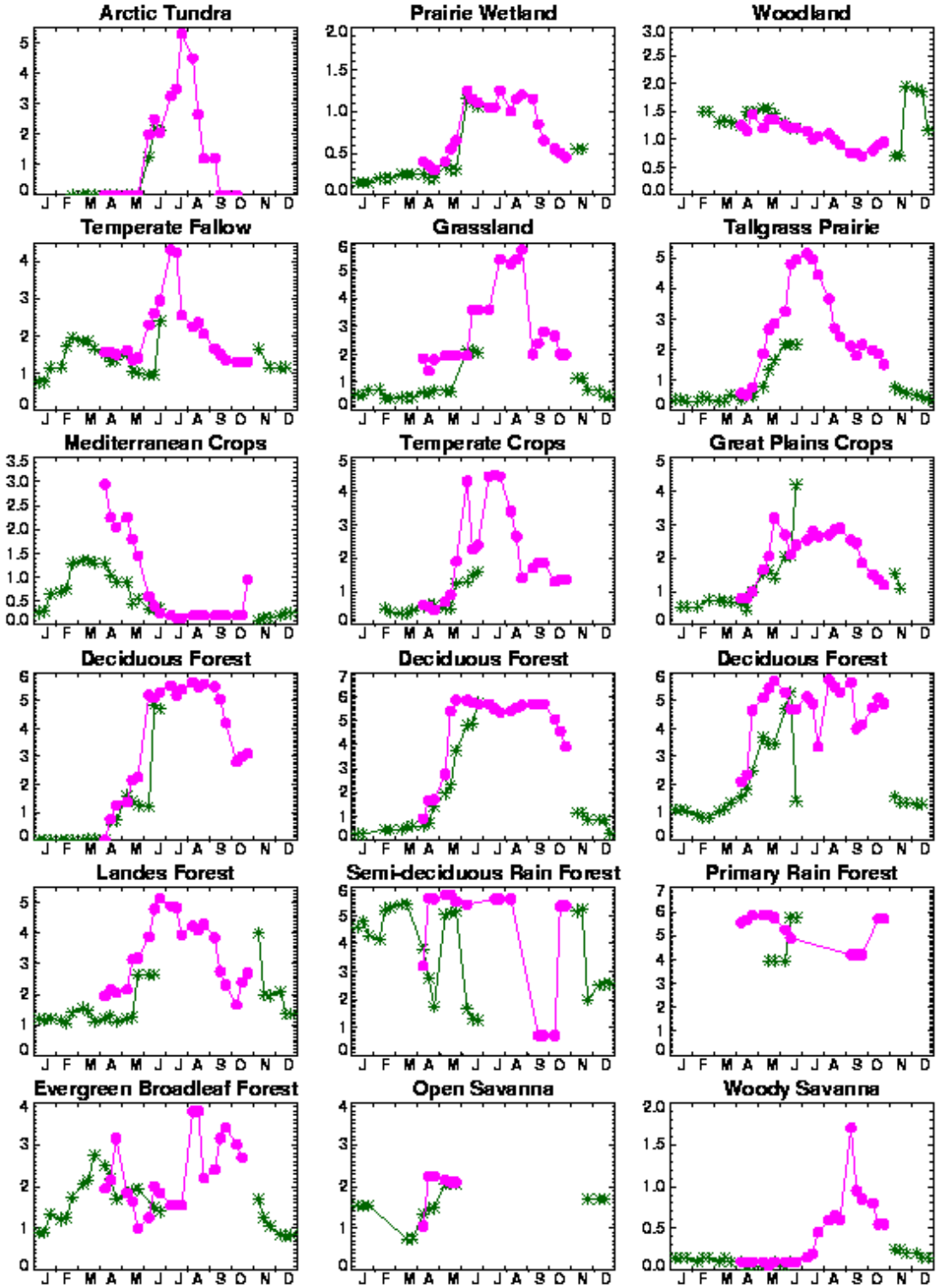

Annex2 4 : Temporal profile of LAI over an annual cycle

(POLDER-1 : green ; POLDER-2 : magenta)

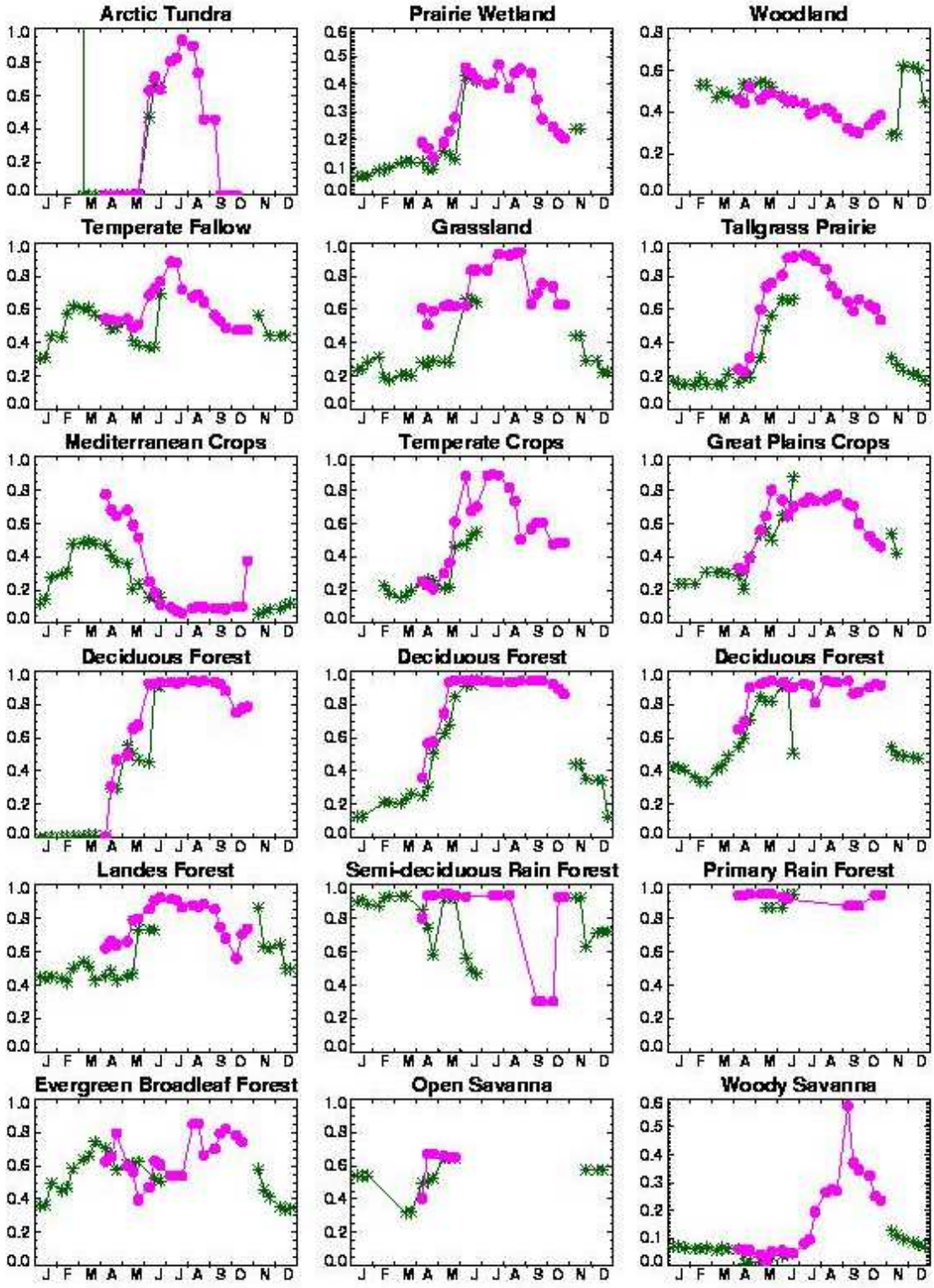

Annex2 5 : Temporal profile of FVC over an annual cycle

(POLDER-1 : green ; POLDER-2 : magenta)

Annex 3 : Multi temporal maps of LAI

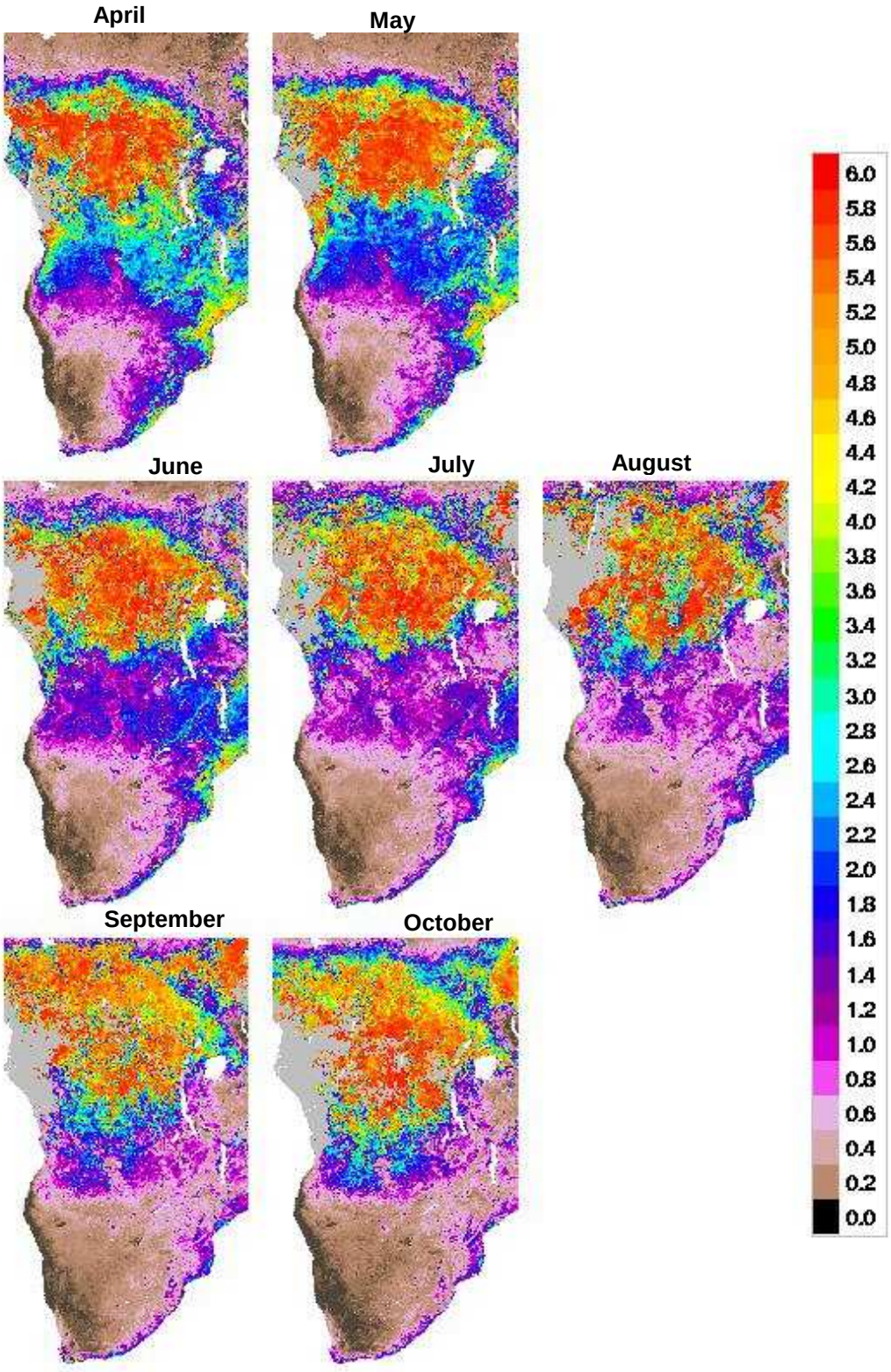

Annex3 1 : POLDER-2 LAI over Africa for the central 10-day periods from April to October 2003.

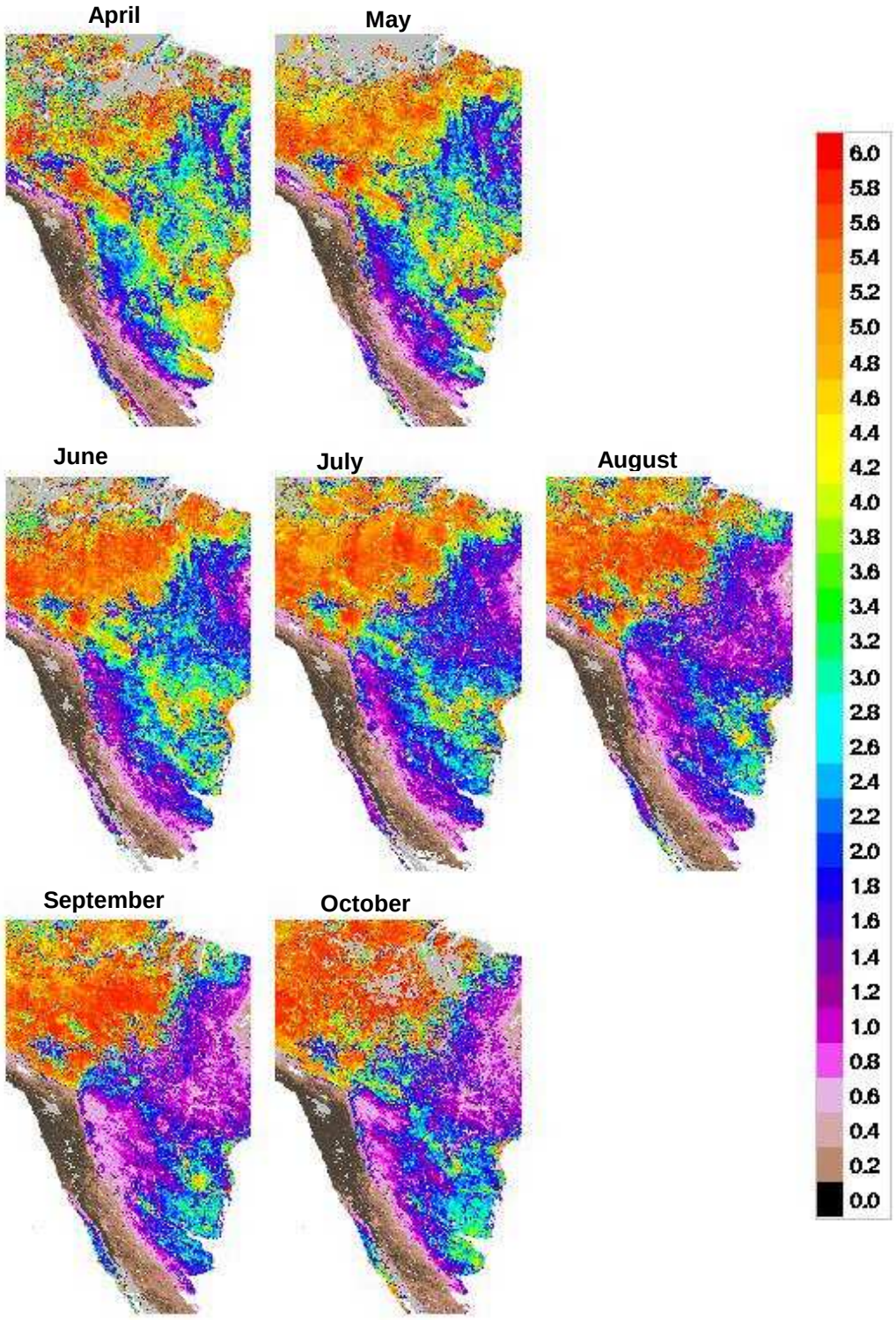

Annex3 2 : POLDER-2 LAI over South America for the central 10-day periods from April to October 2003.

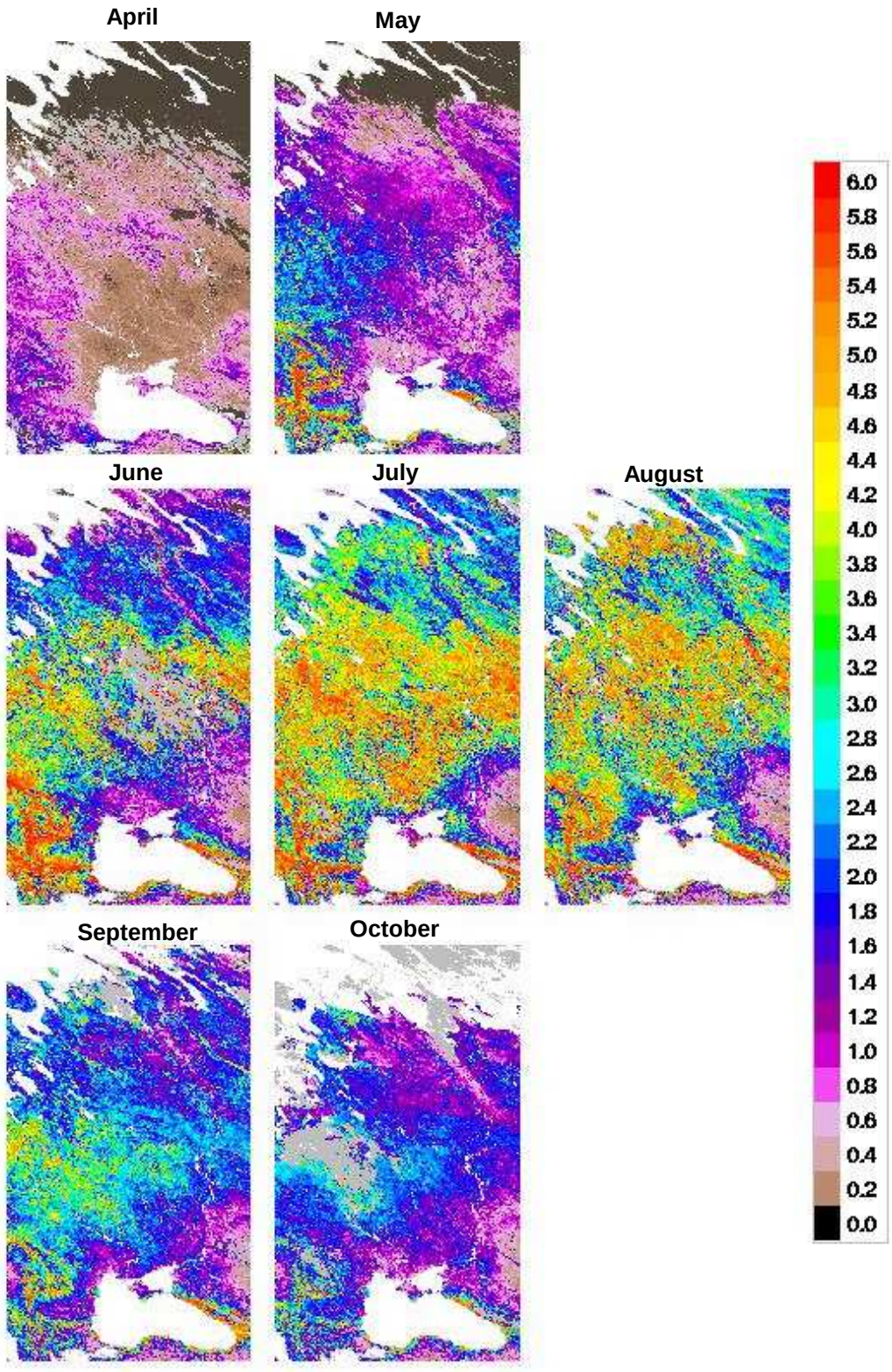

Annex3 3 : POLDER-2 LAI over Central Europe for the central 10-day periods from April to October 2003.

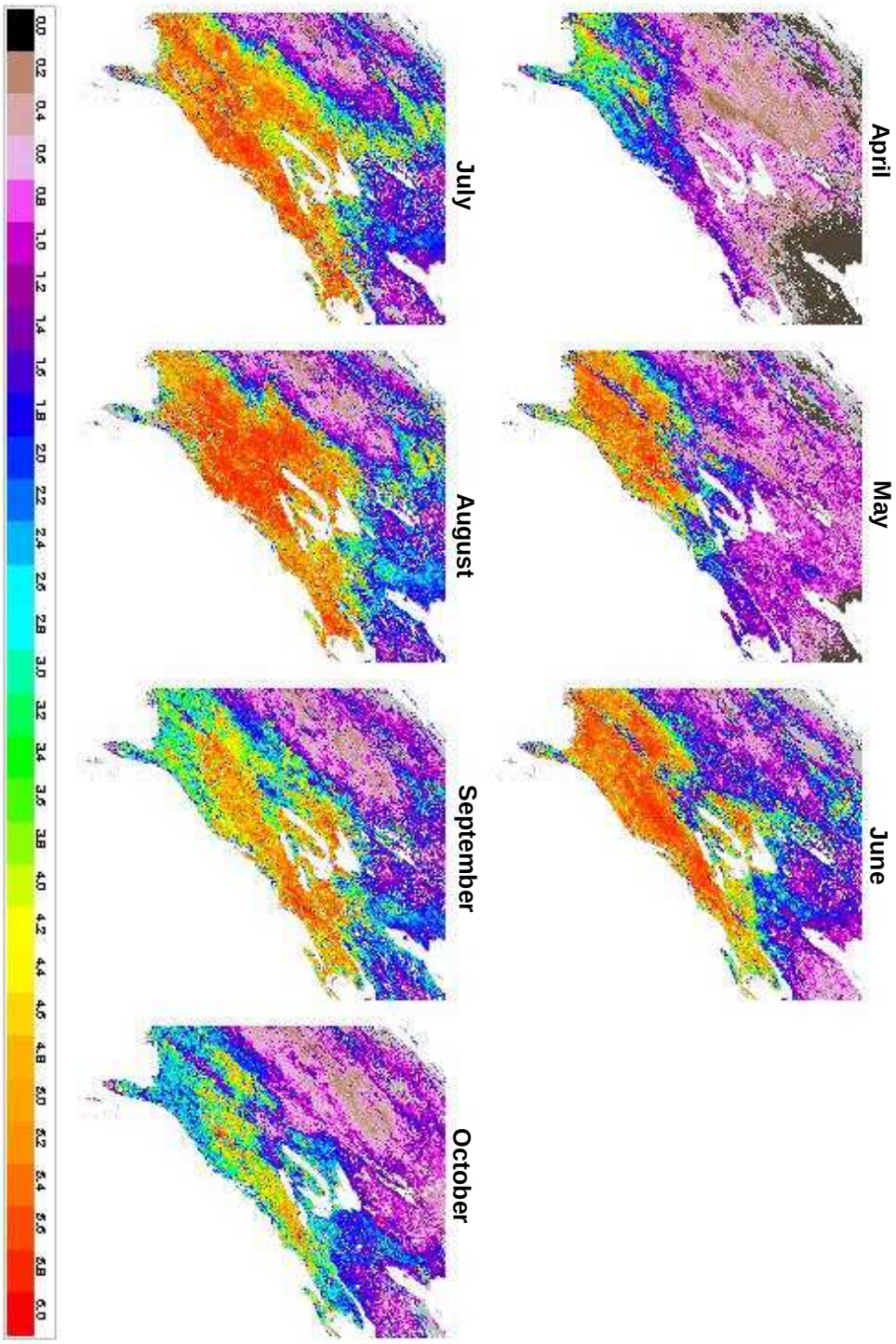

Annex3 4 : POLDER-2 LAI over North America for the central 10-day periods from April to October 2003.

Annex 4 : Comparison POLDER-2 / POLDER-1

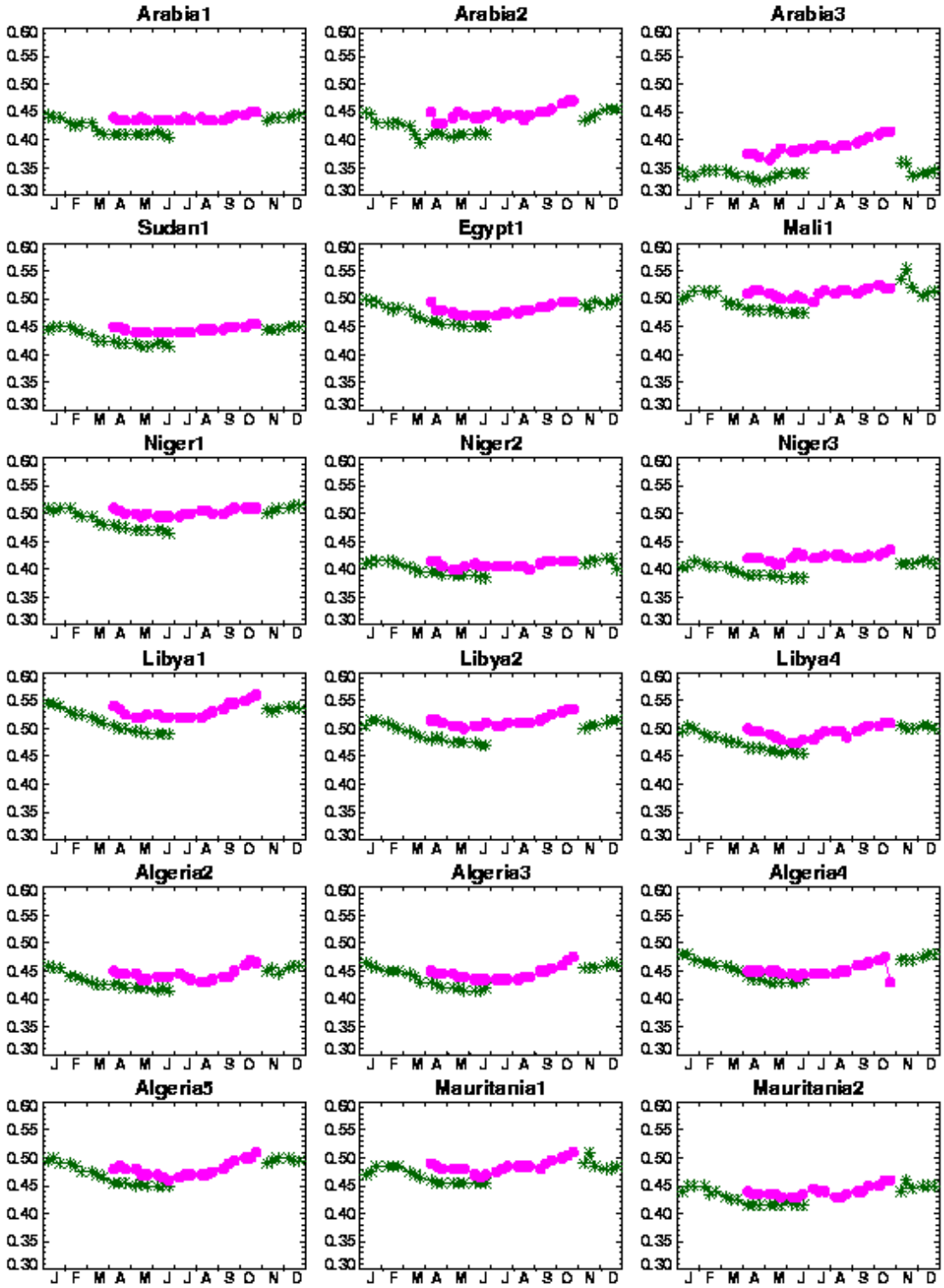

Annex4 1 : Temporal profiles of DHR 670nm over desert sites

(POLDER-1 :green; POLDER-2: magenta)

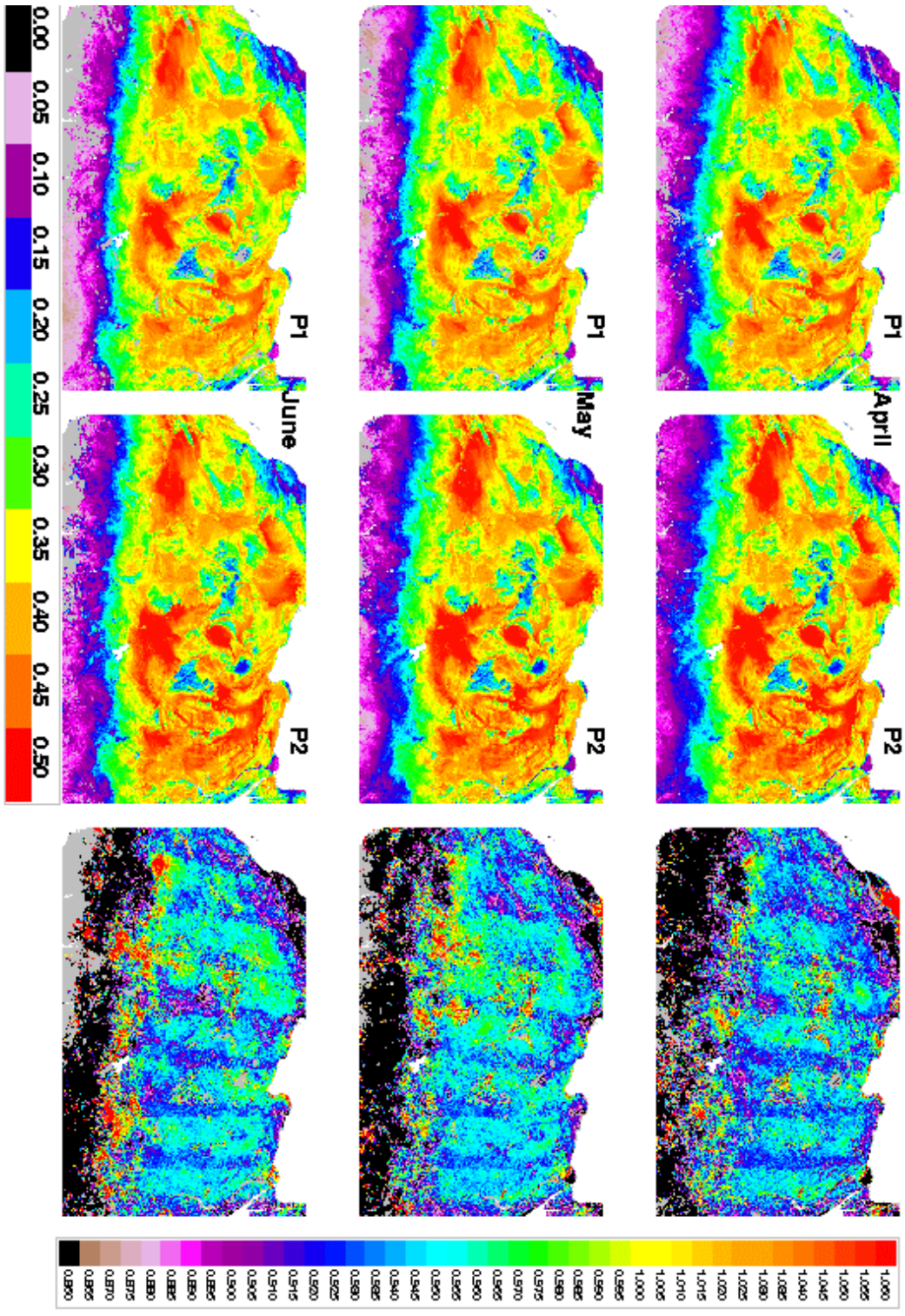

Annex4 2 : DHR 670nm over Sahara from POLDER-1 (left), POLDER-2 (middle), and ratio POLDER-1/POLDER-2 (right)

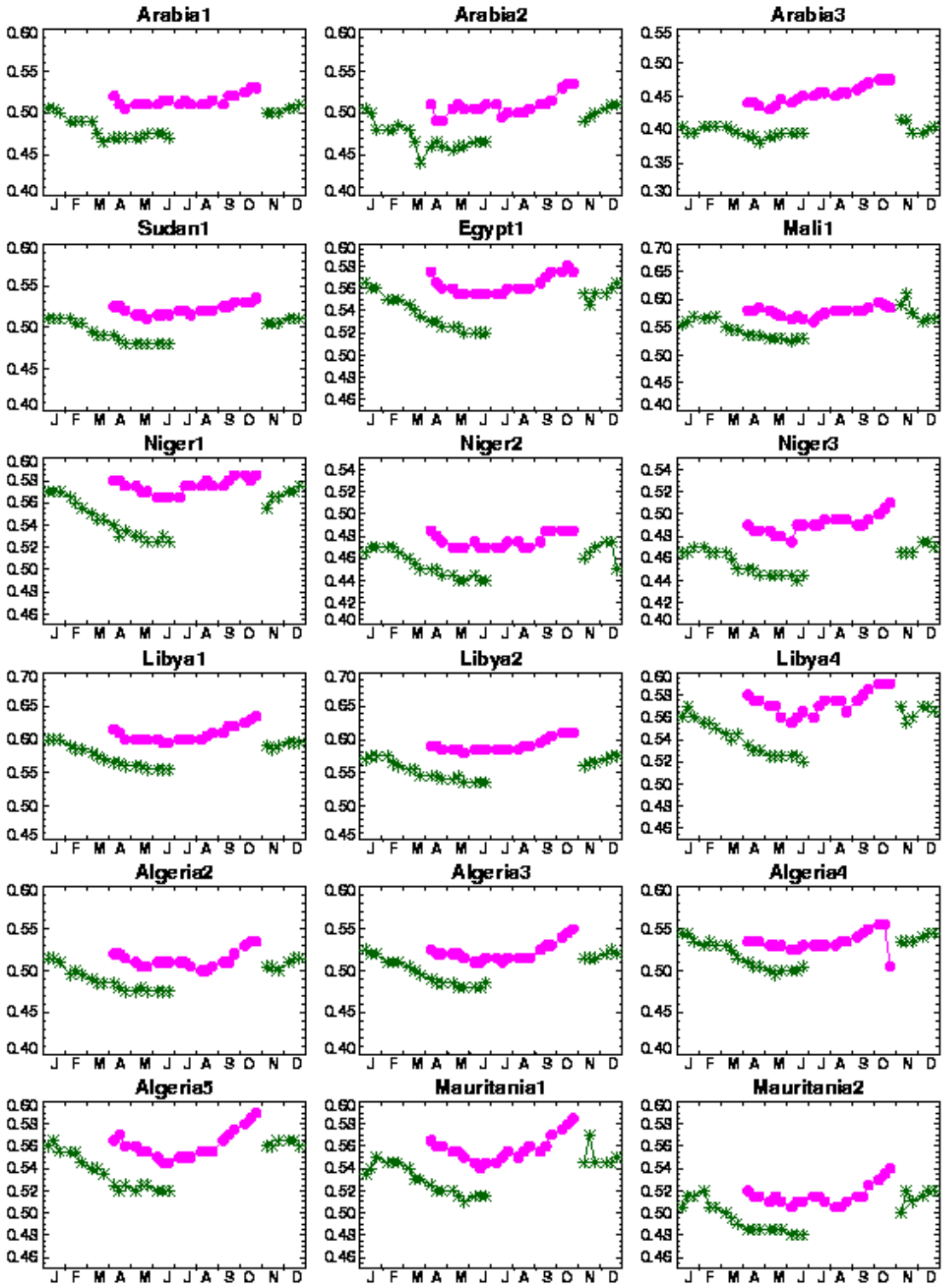

Annex4 3 : Temporal profiles of DHR 865nm over desert sites

(POLDER-1: green; POLDER-2 : magenta)

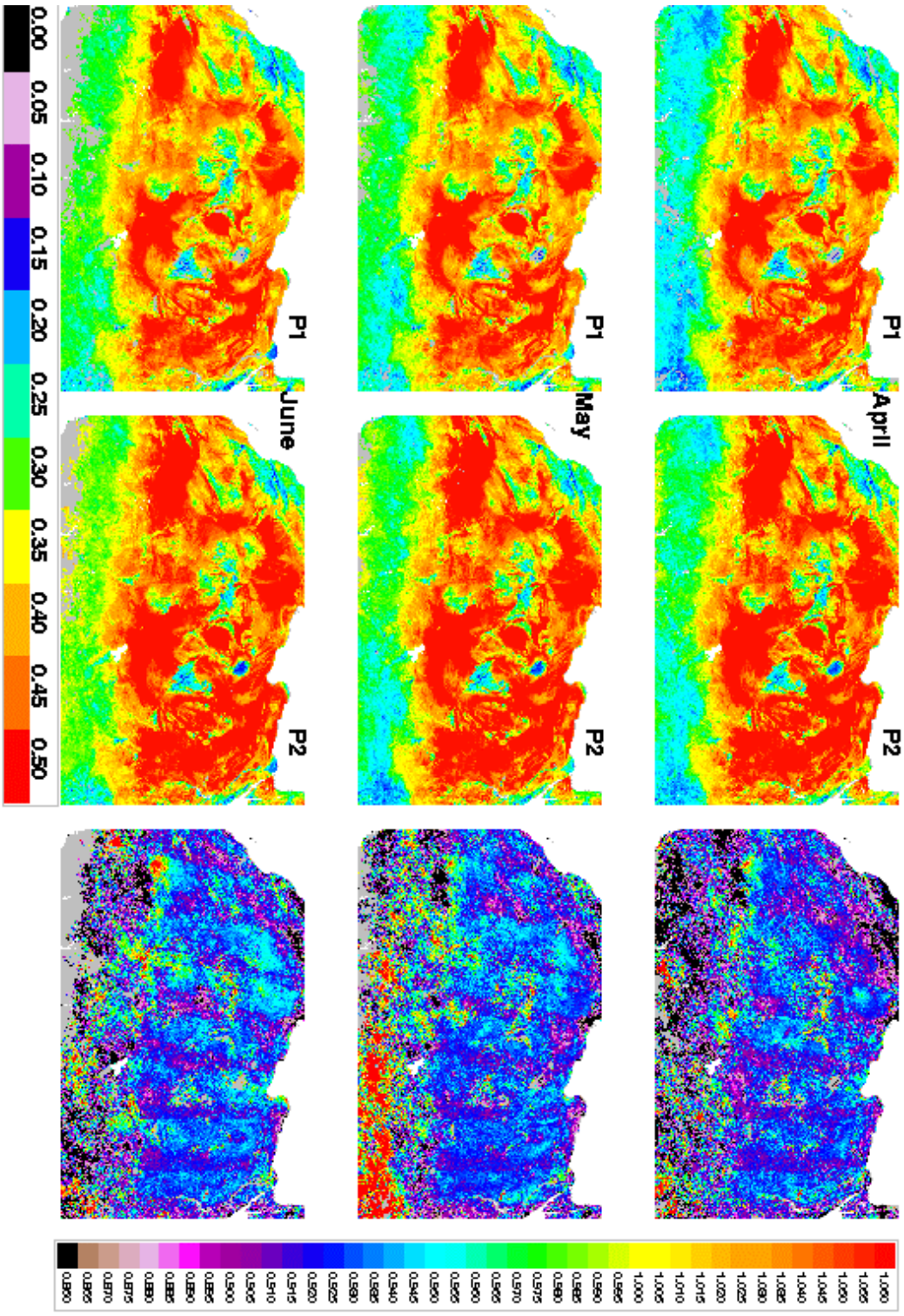

Annex4 4 : DHR 865nm over Sahara from POLDER-1 (left), POLDER-2 (middle), and ratio POLDER-1/POLDER-2 (right)

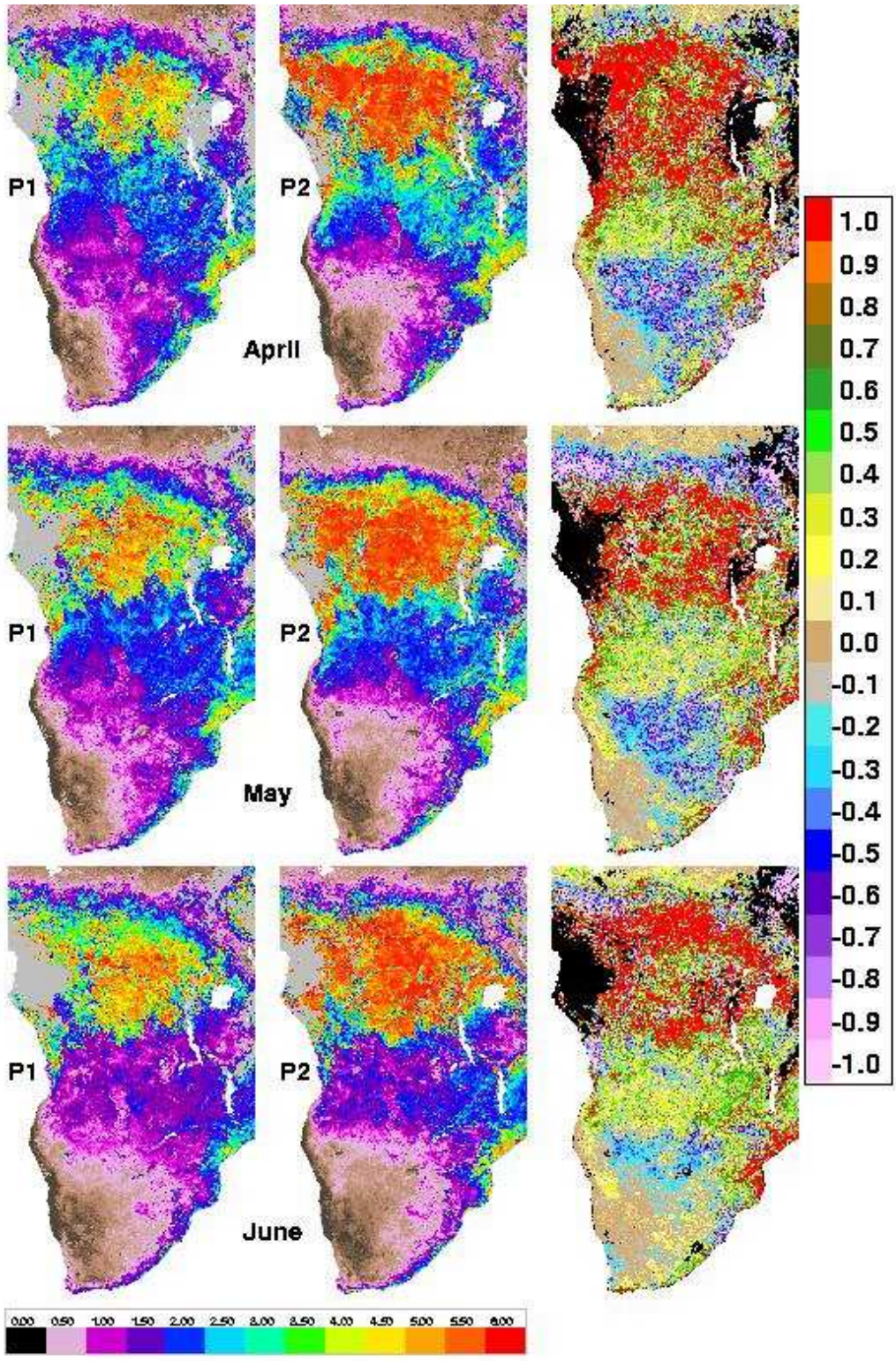

Annex4 5 : LAI POLDER-1 (left), POLDER-2 (middle) and difference (POLDER-2 – POLDER-1) at right for synthesis periods on 15th April, 15th May and 15th June, over Africa.

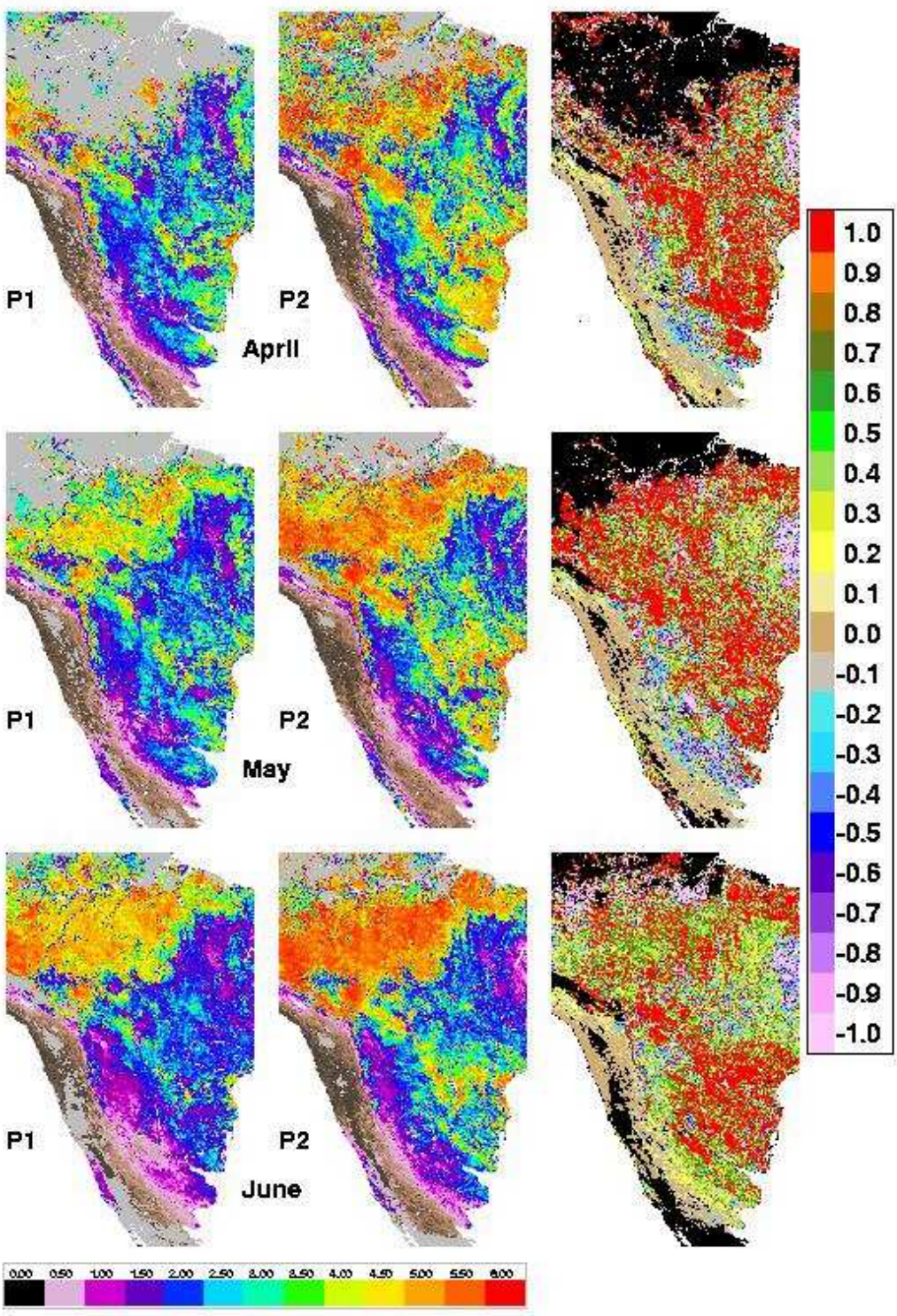

Annex4 6 : LAI POLDER-1 (left), POLDER-2 (middle) and difference (POLDER-2 – POLDER-1) at right for synthesis periods on 15th April, 15th May and 15th June, over South America.

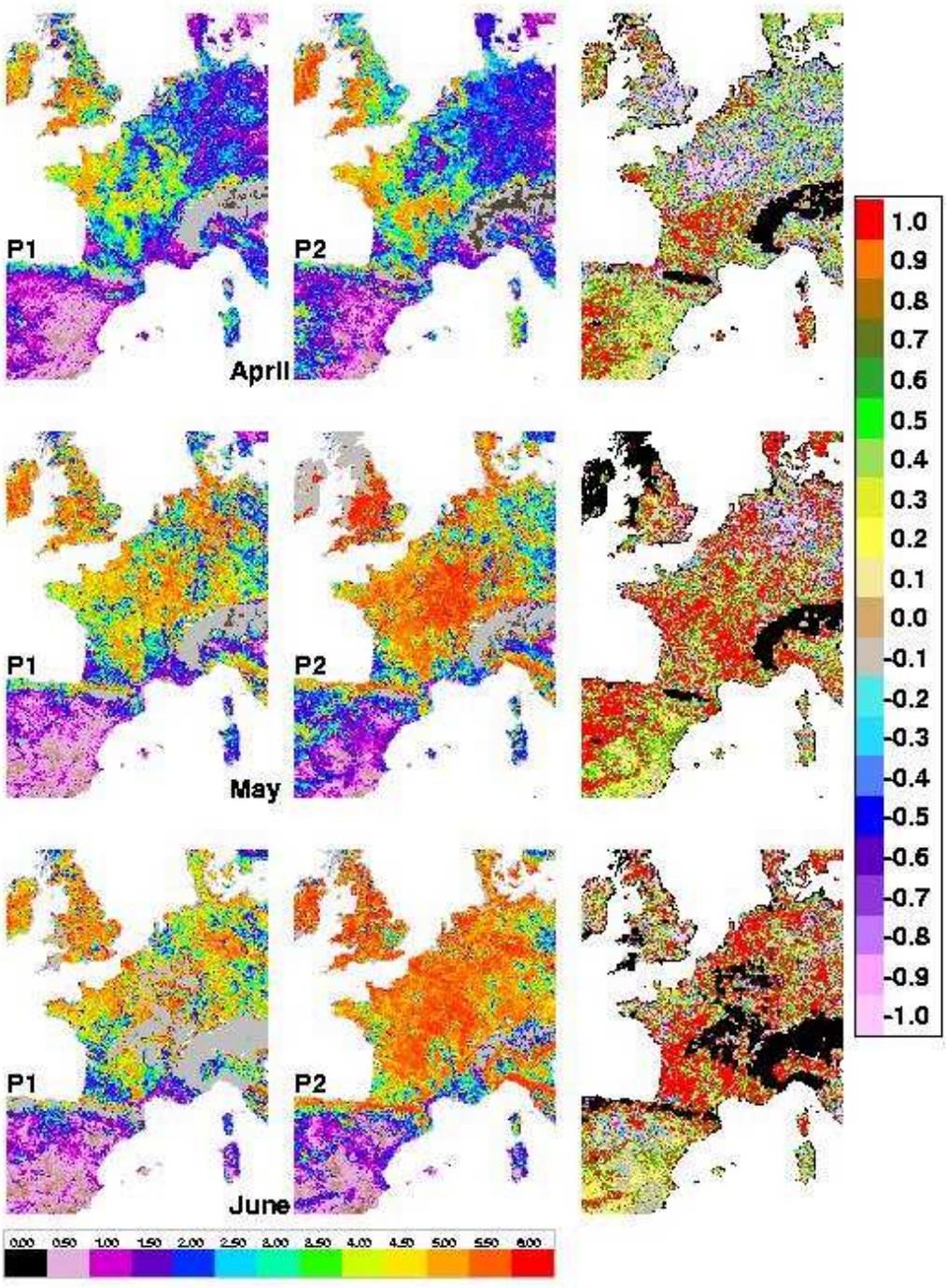

Annex4 7 : LAI POLDER-1 (left), POLDER-2 (middle) and difference (POLDER-2 – POLDER-1) at right for synthesis periods on 15th April, 15th May and 15th June, over France.

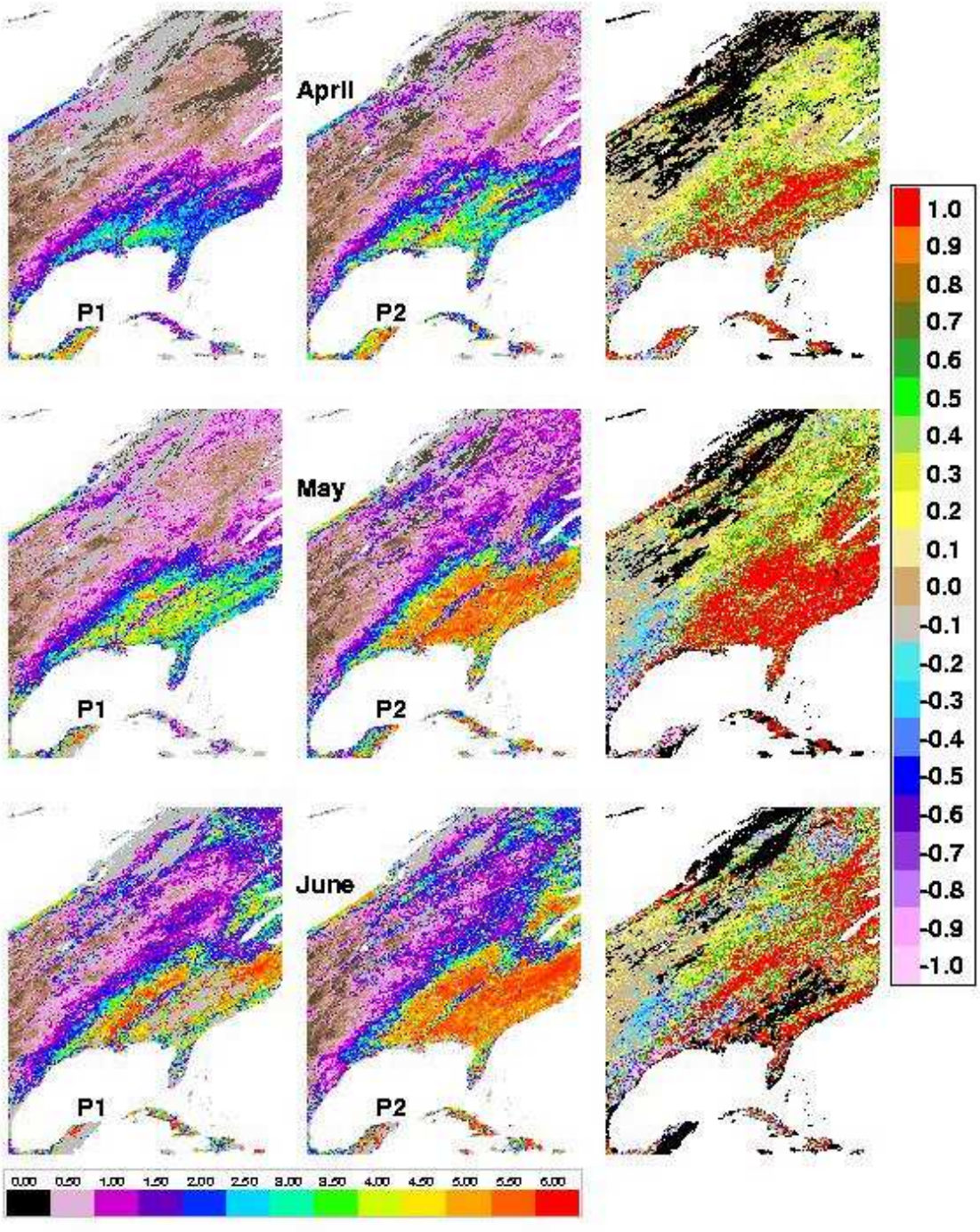

Annex4 8 : LAI POLDER-1 (left), POLDER-2 (middle) and difference (POLDER-2 – POLDER-1) at right for synthesis periods on 15th April, 15th May and 15th June, over North America.

Annex 5 : Comparison POLDER-2 / MODIS

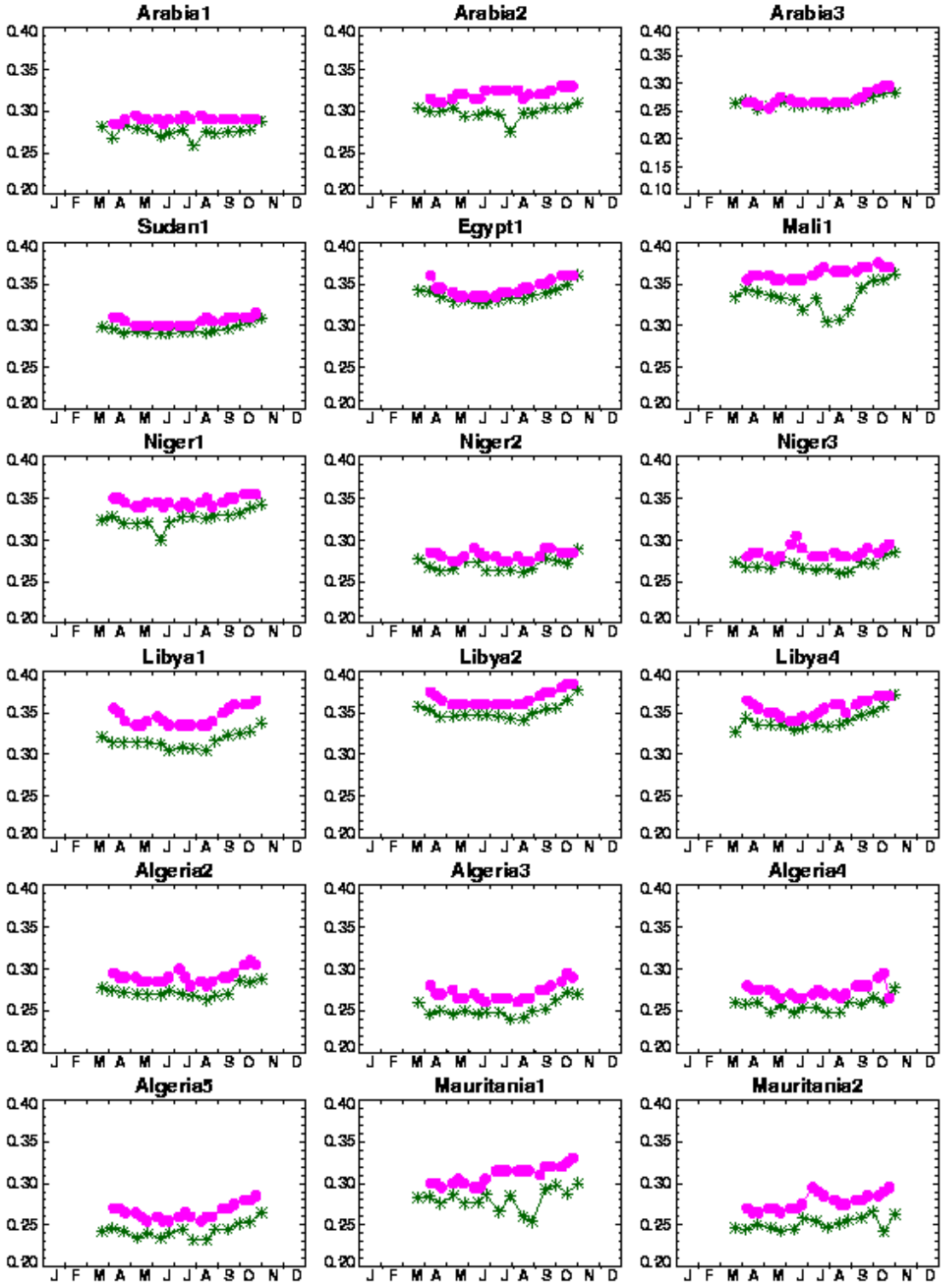

Annex5 1 : Temporal profiles of POLDER-2 DHR 565nm (magenta) and MODIS BSA b4 [545 – 565nm] (green) over desert sites.

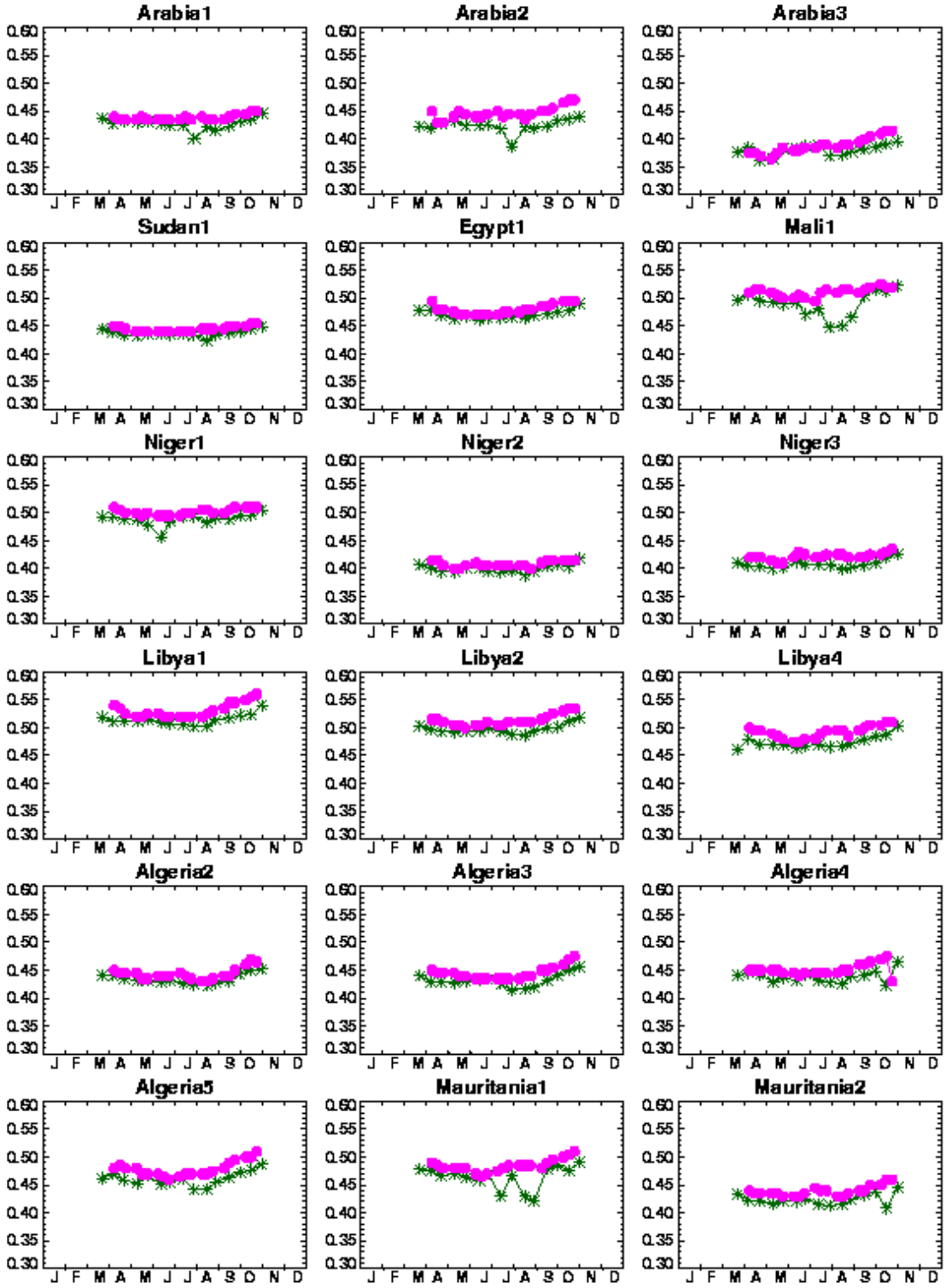

Annex5 2 : Temporal profiles of POLDER-2 DHR 670nm (magenta) and MODIS BSA b1 [620 – 670nm] (green) over desert sites.

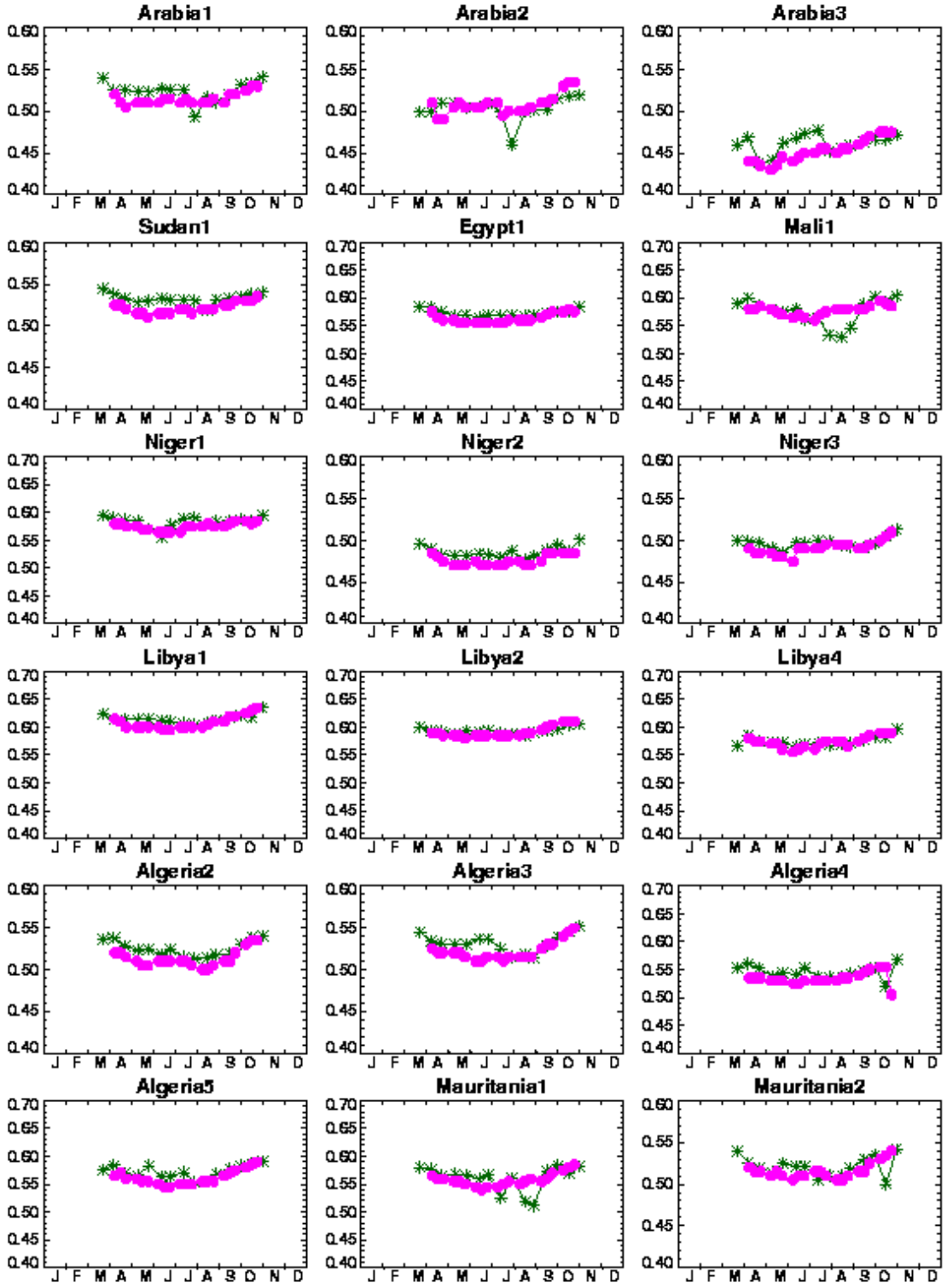

Annex5 3 : Temporal profiles of POLDER-2 DHR 865nm (magenta) and MODIS BSA b2 [841 – 876nm] (green) over desert sites.

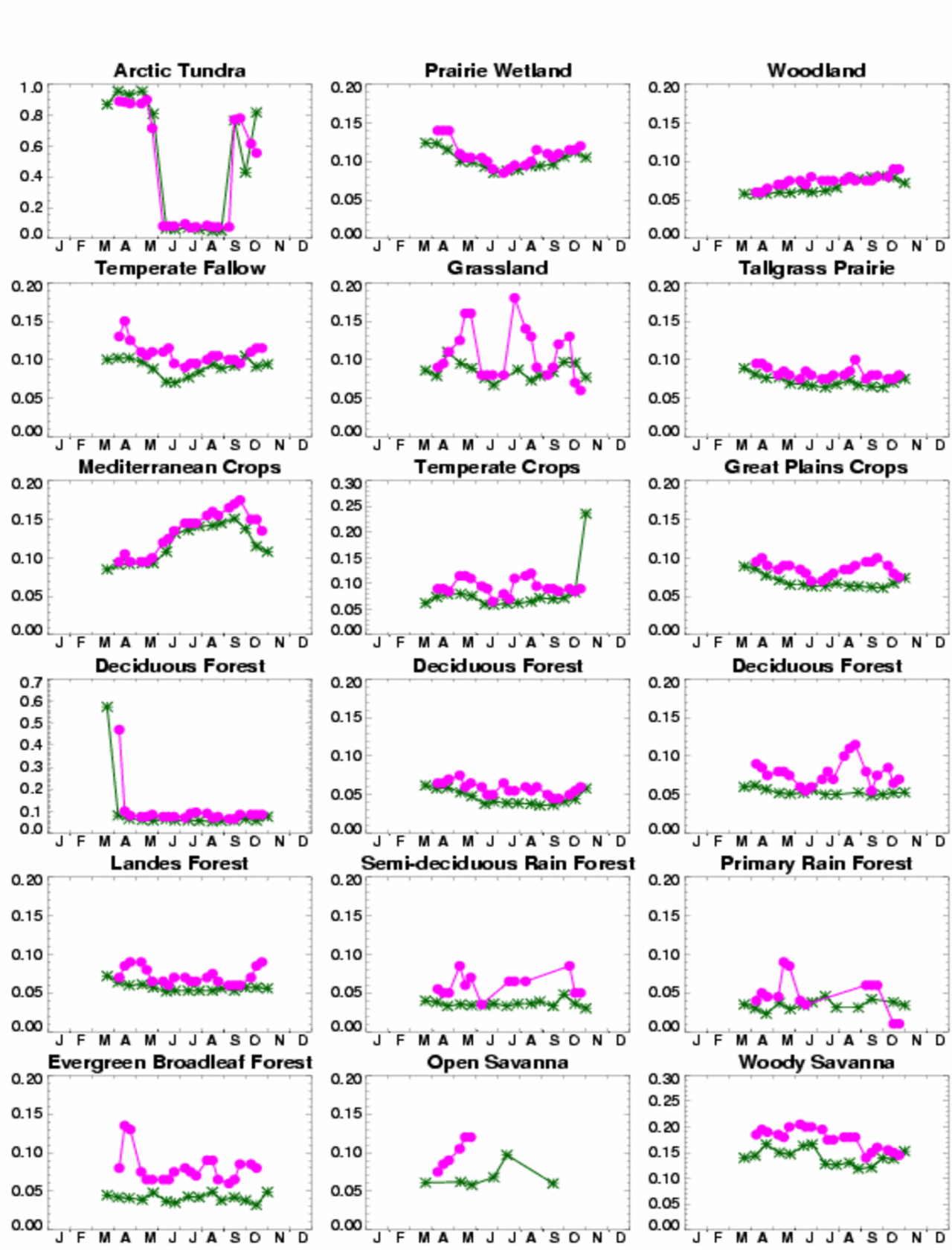

Annex5 4 : Temporal profiles of POLDER-2 DHR 565nm (magenta) and MODIS BSA b4 [545 – 565nm] (green) over main continental ecosystems.

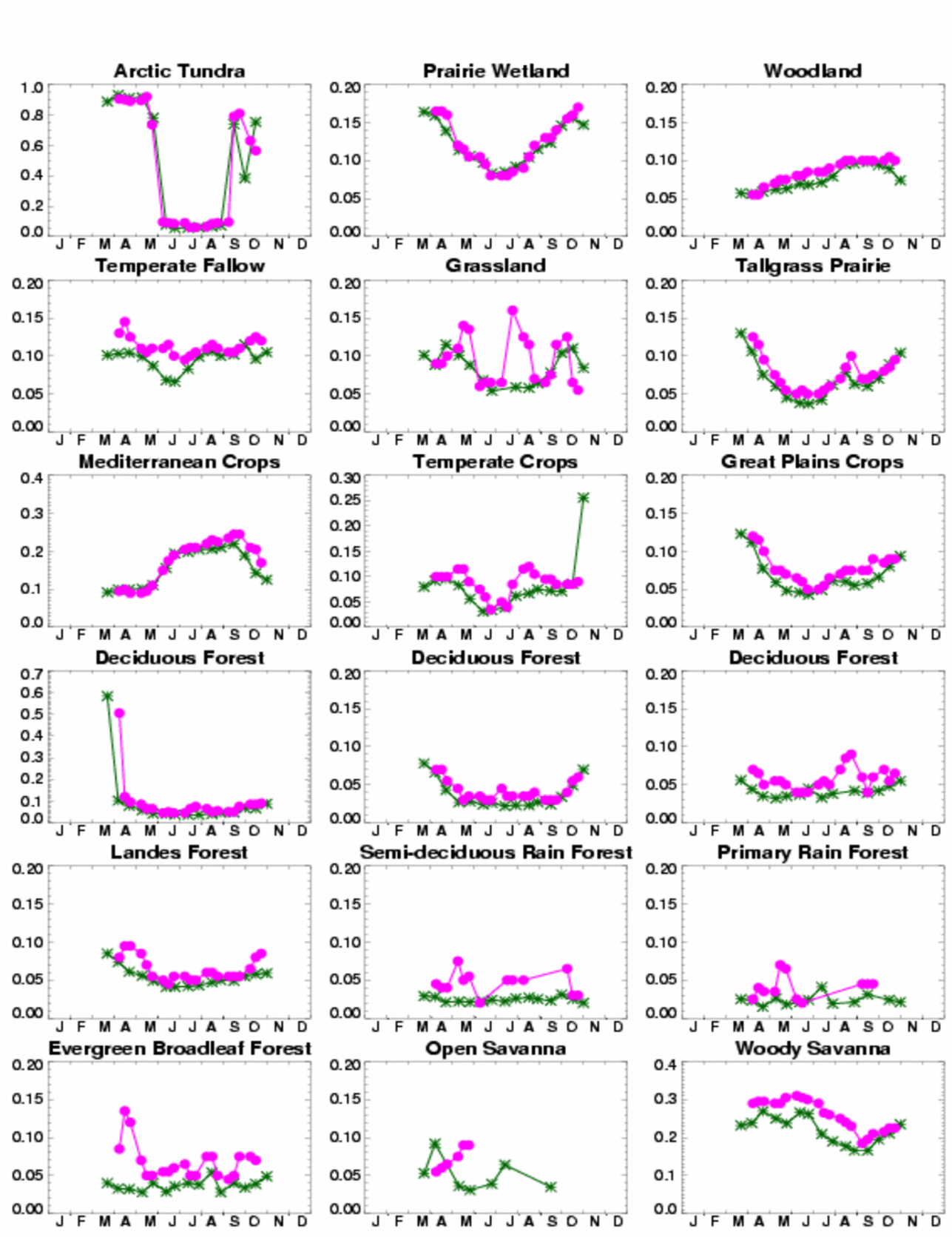

Annex5 5 : Temporal profiles of POLDER-2 DHR 670nm (magenta) and MODIS BSA b1 [620 – 670nm] (green) over main continental ecosystems.

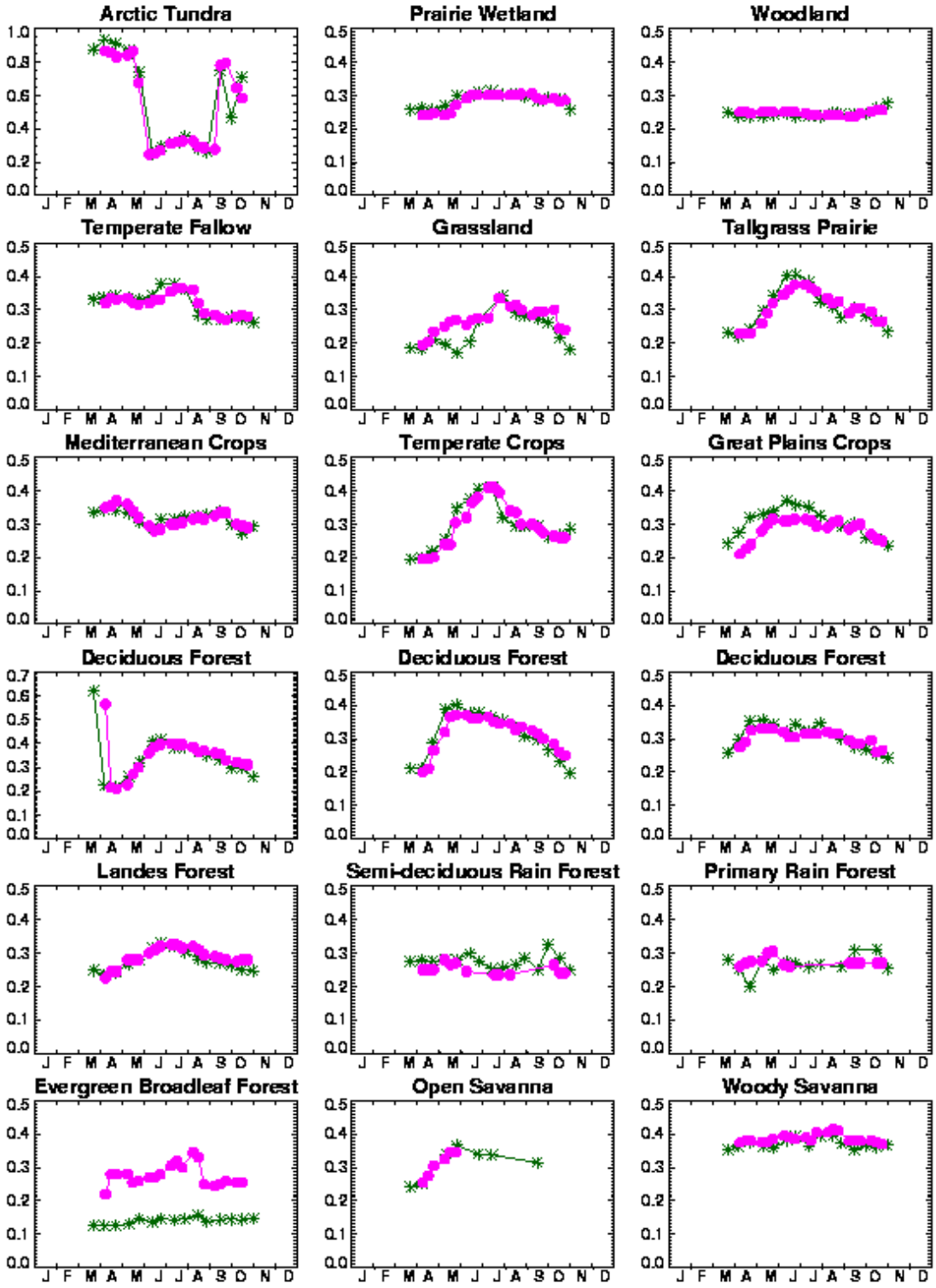

Annex5 6 : Temporal profiles of POLDER-2 DHR 865nm (magenta) and MODIS BSA b2 [841 – 876nm] (green) over main continental ecosystems.

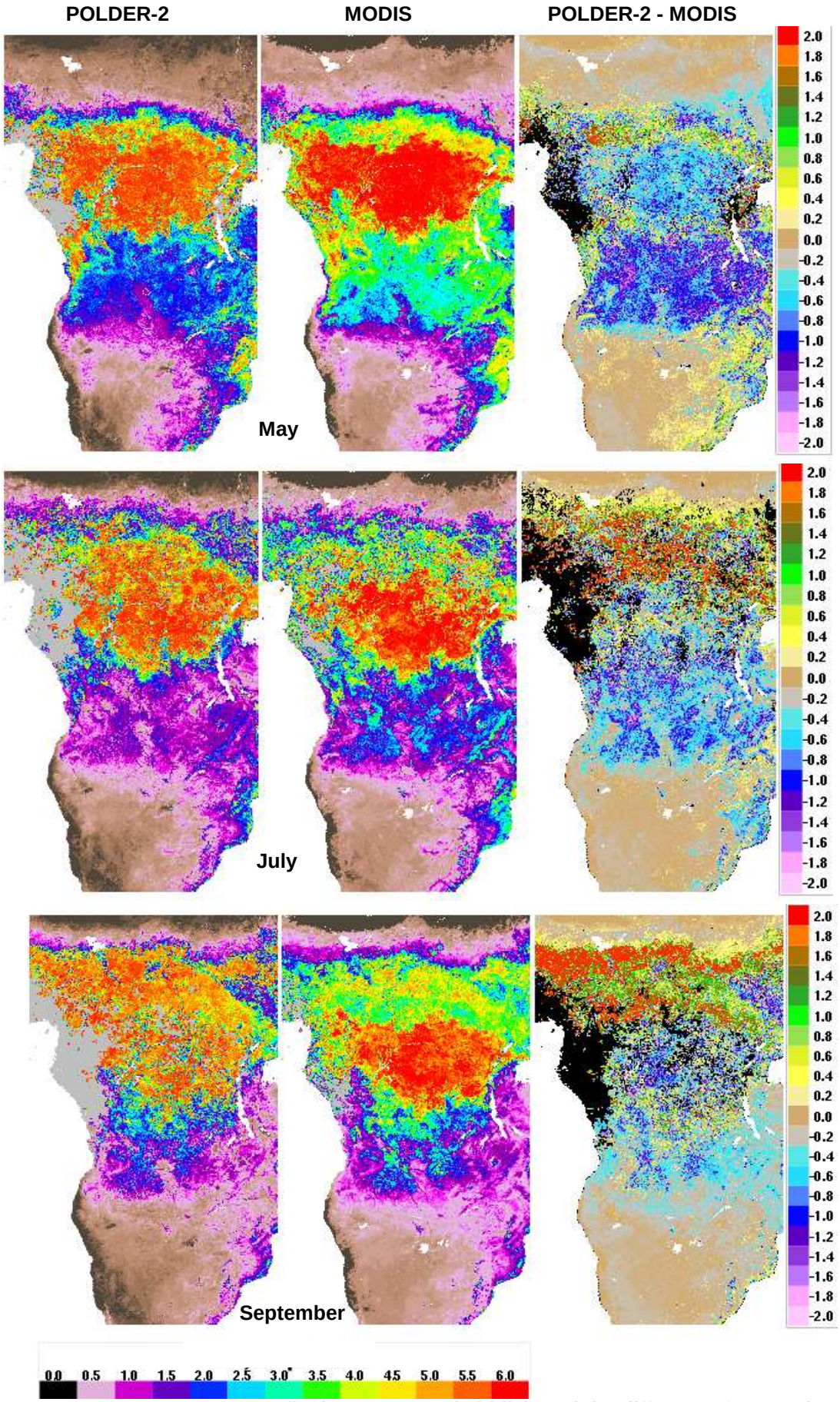

Annex5 7 : LAI POLDER-2 (left), LAI MODIS (middle), and the difference for May (top), July (middle), and September (bottom) over Africa.

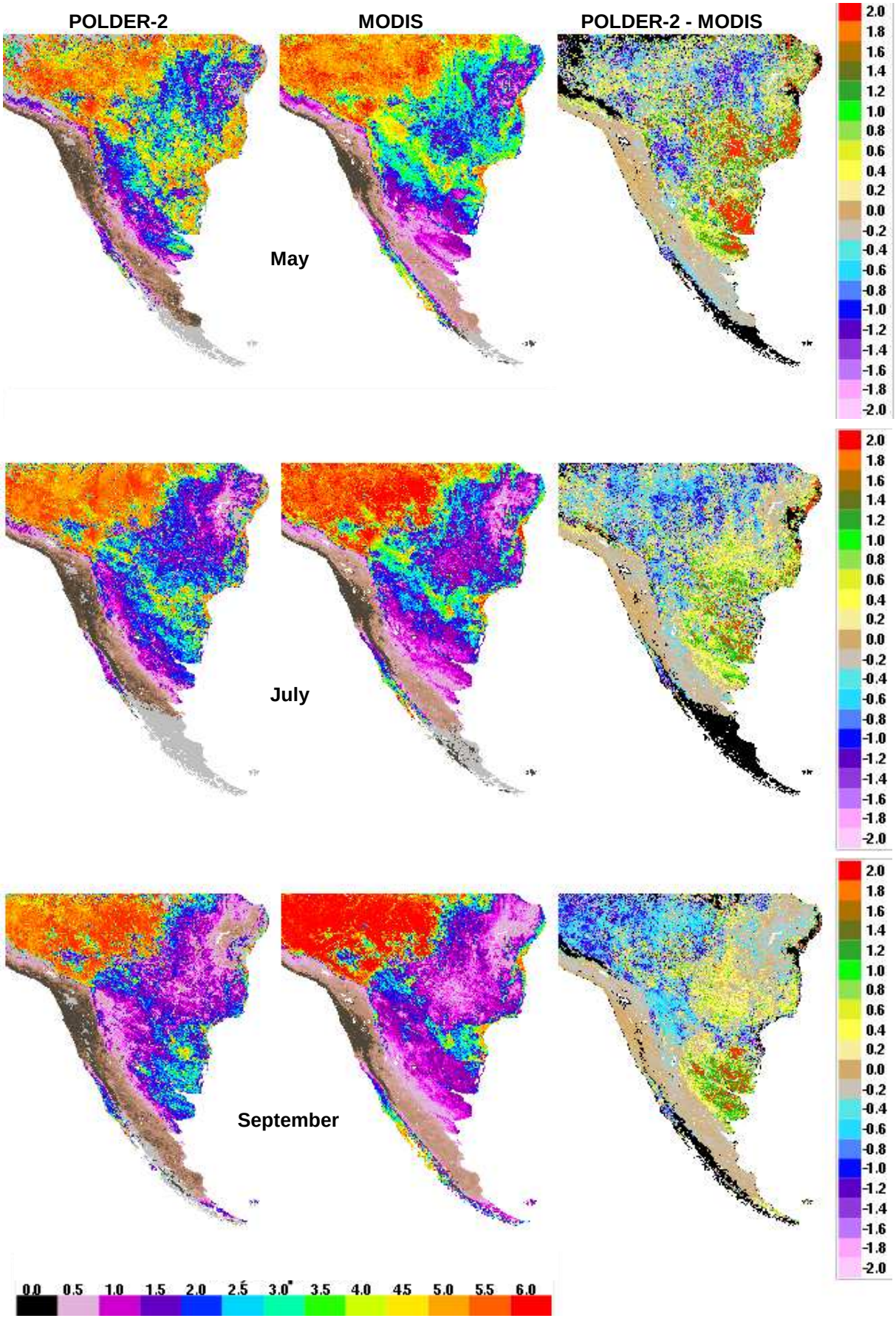

Annex5 8 : LAI POLDER-2 (left), LAI MODIS (middle), and the difference for May (top), July (middle), and September (bottom) over South America.

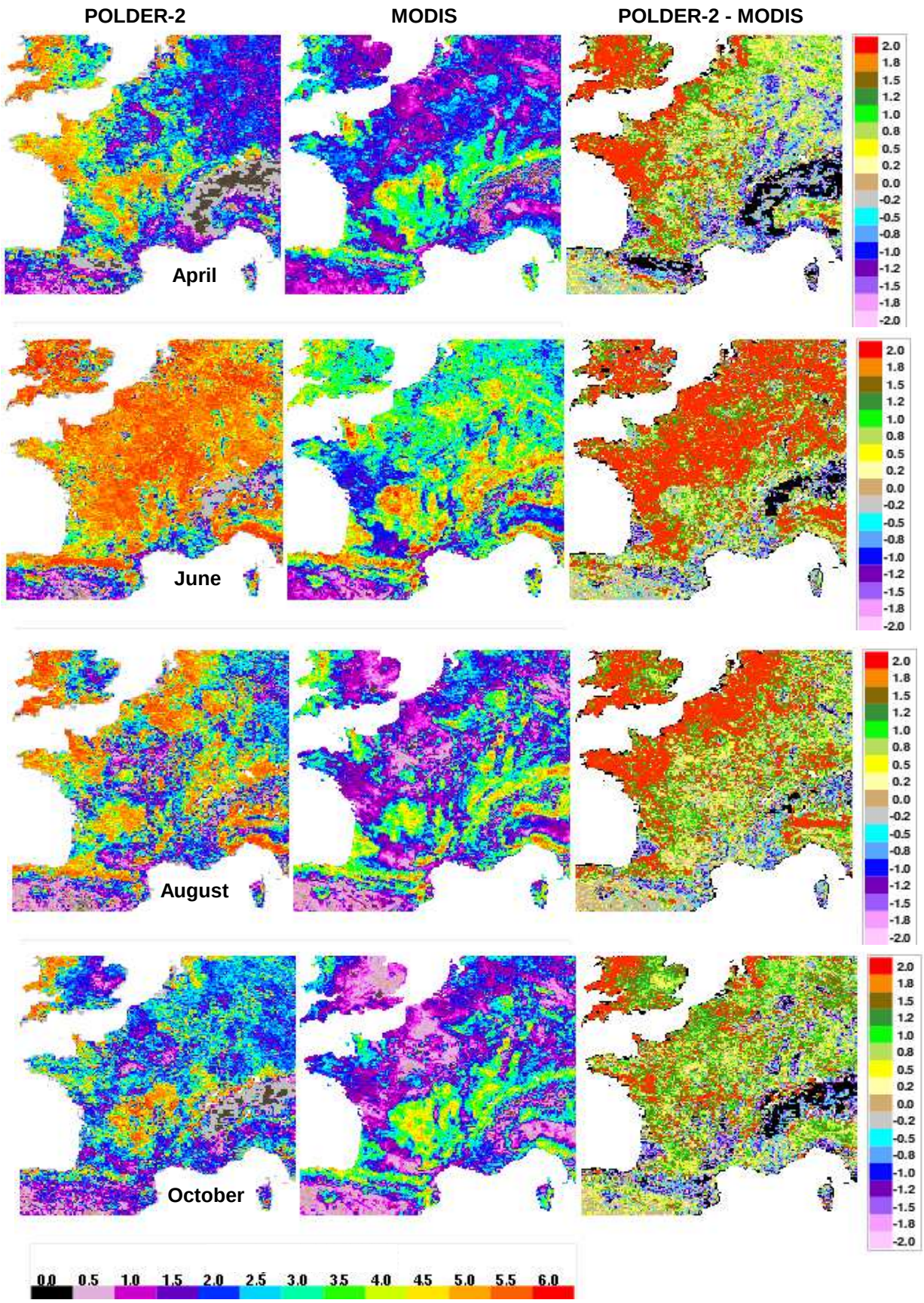

Annex5 9 : LAI POLDER-2 (left), LAI MODIS (middle), and the difference for April, June, August and October (from top to bottom) over France.

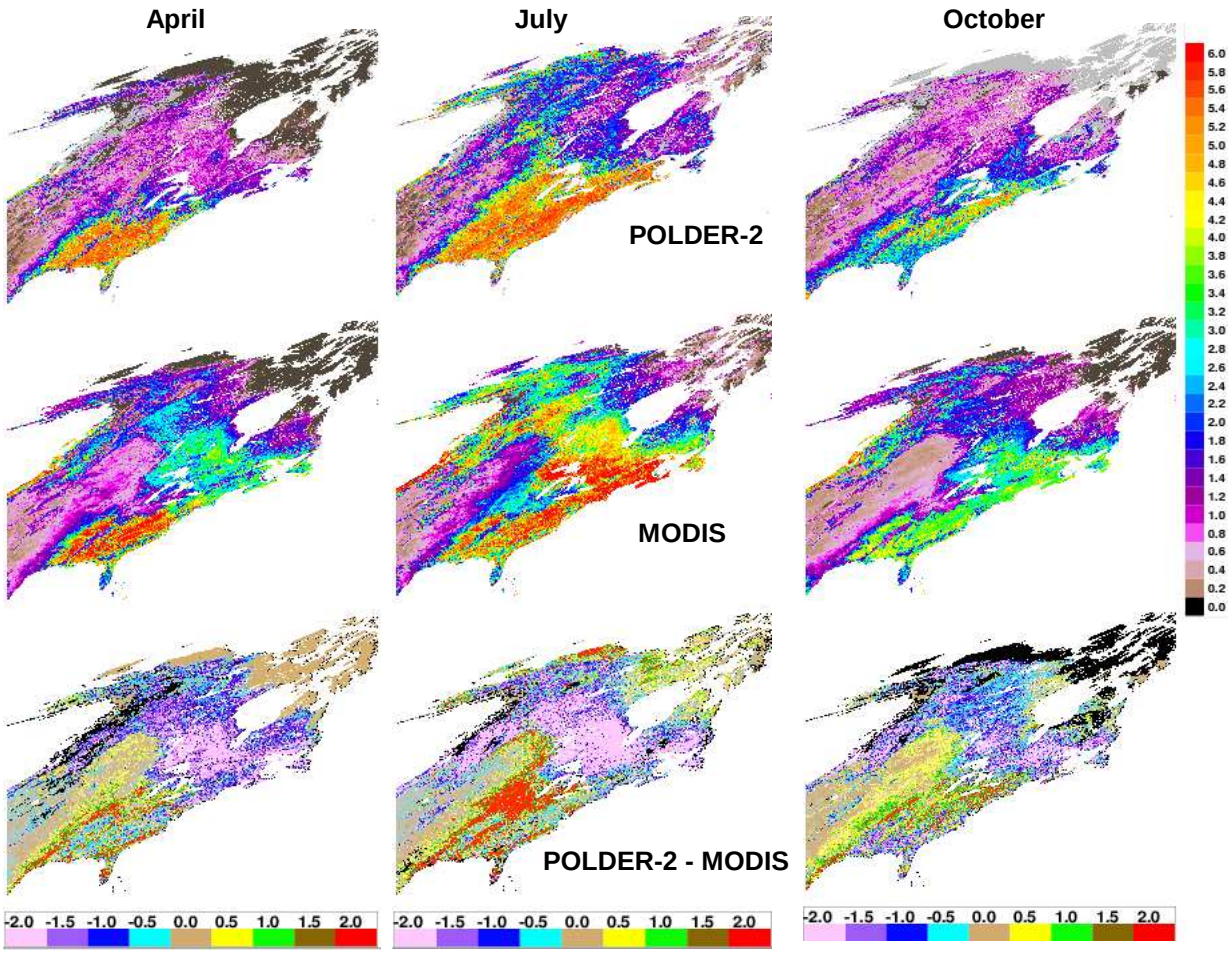

Annex5 10 : LAI POLDER-2 (top), LAI MODIS (middle), and the difference (bottom) for April, July, and October (from left to right) over North America.

Annex 6 : Comparison with in-situ measurements

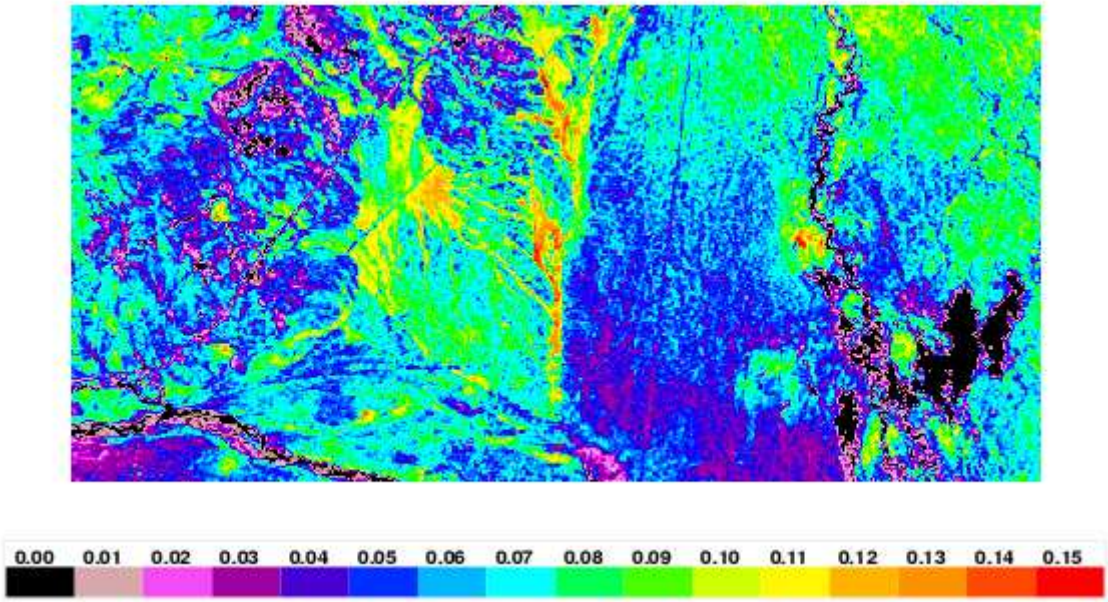

Annex 6 1 : LAI map (20m resolution) from VALERI ground data over Turco (Bolivia).

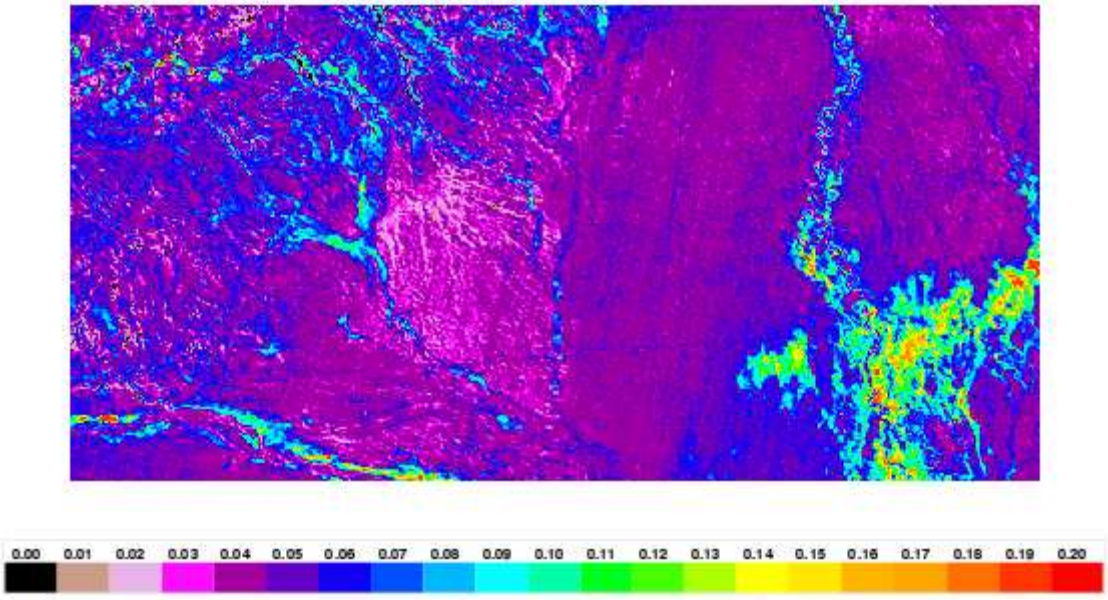

Annex 6 2 : FVC map (20m resolution) from VALERI ground data over Turco (Bolivia).

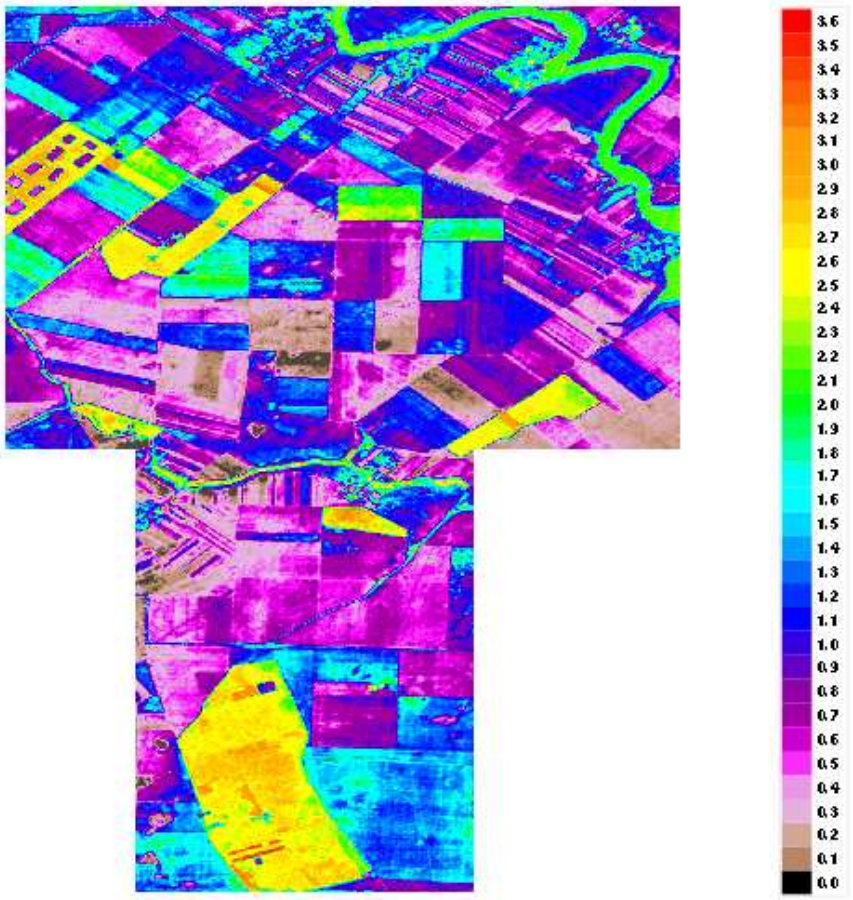

Annex 6 3 : LAI map (20m resolution) from VALERI ground data over Fundulea (Romania).

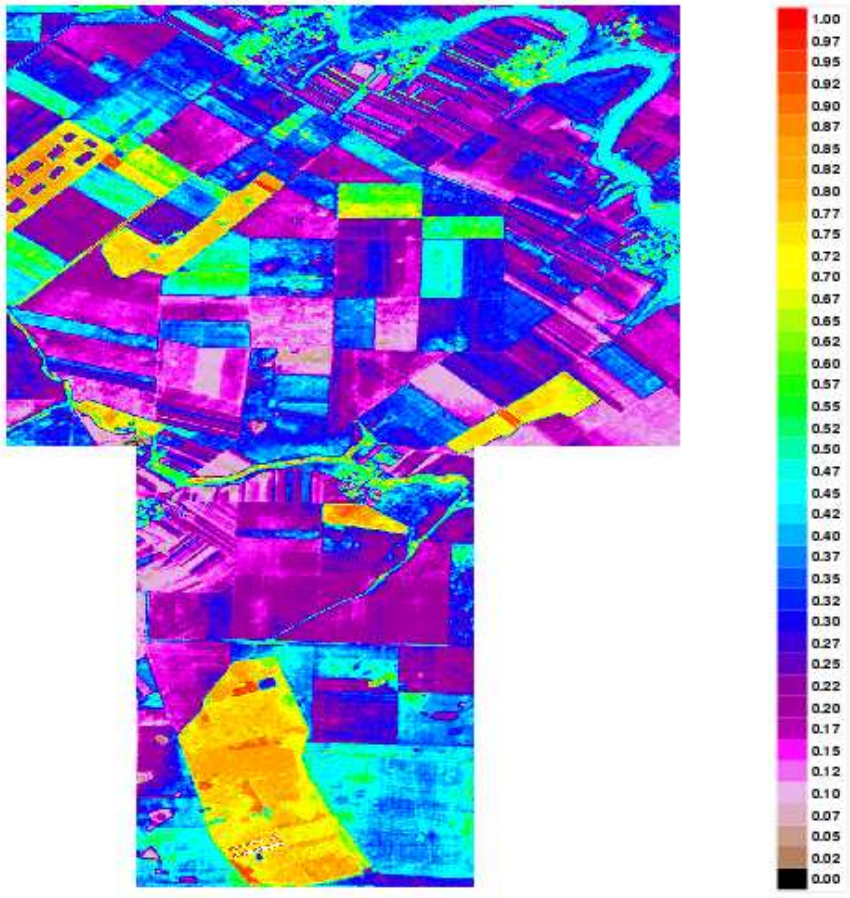

Annex 6 4 : FVC map (20m resolution) from VALERI ground data over Fundulea (Romania).

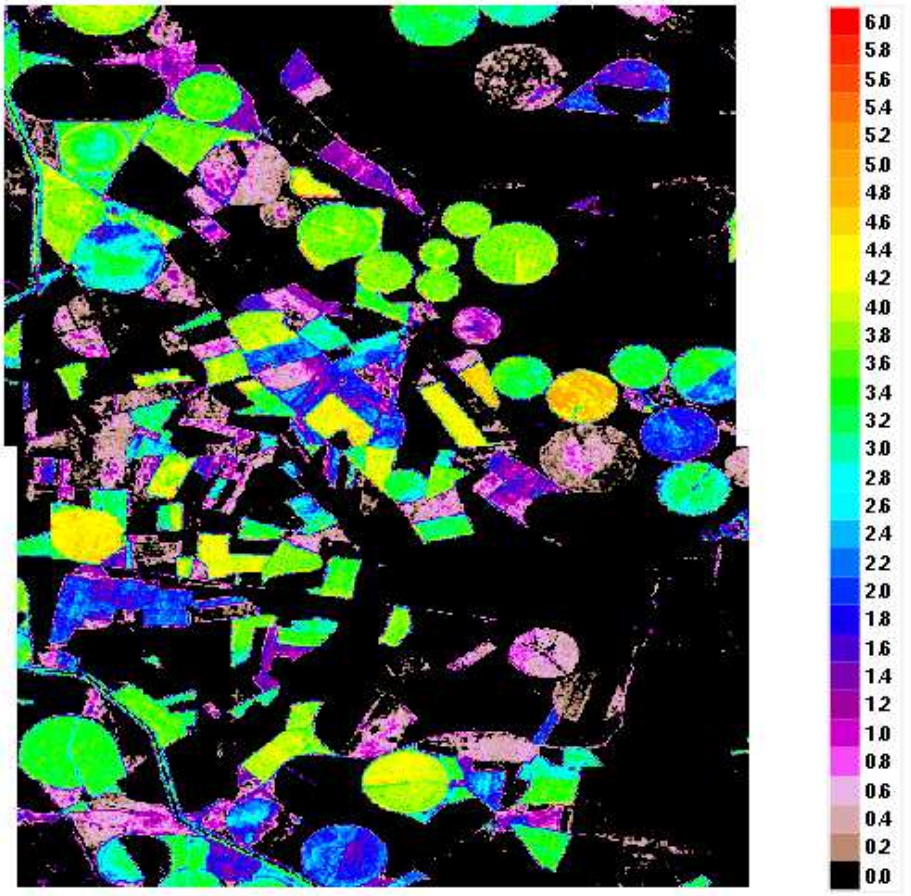

Annex 6 5 : LAI map (20m resolution) from VALERI ground data over Barrax (Spain)

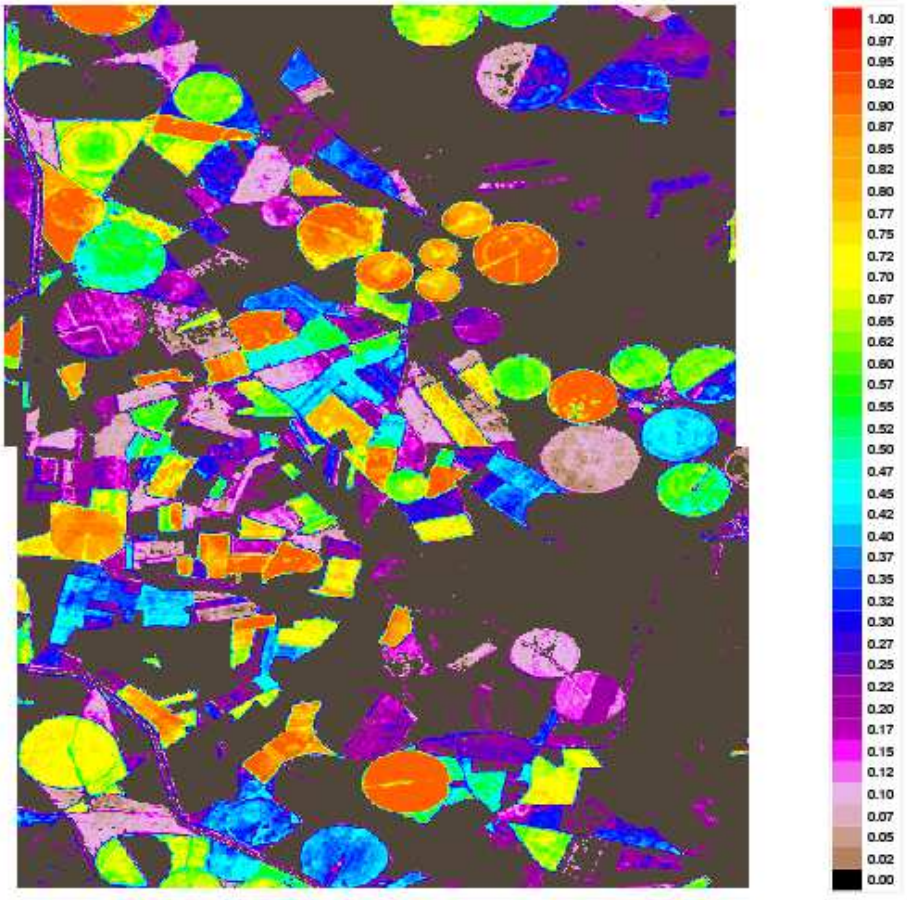

Annex 6 6 : FVC map (20m resolution) from VALERI ground data over Barrax (Spain)

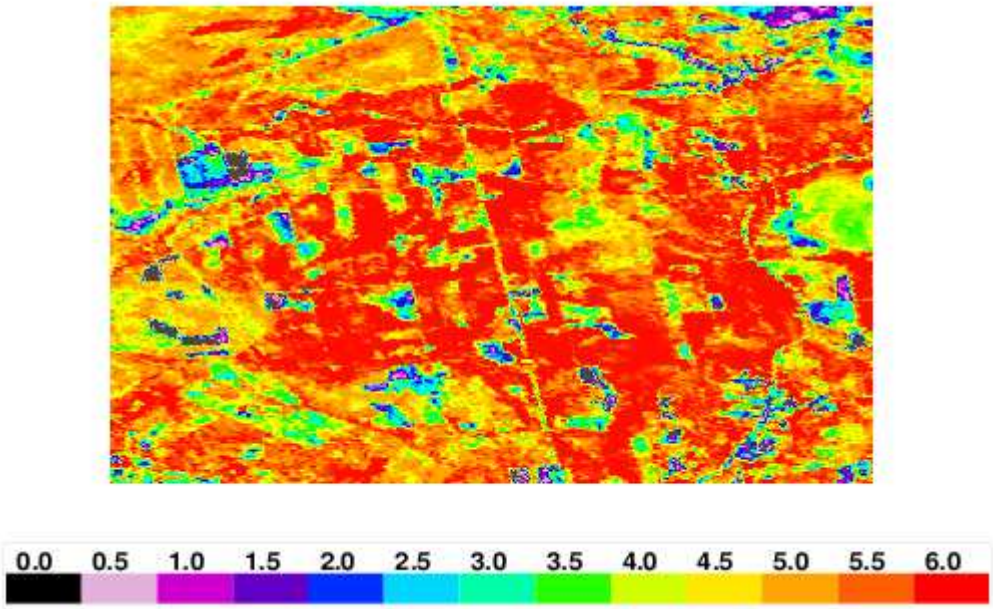

Annex 6 7 : LAI map (20m resolution) from VALERI ground data over Jarvselja (Estonia)

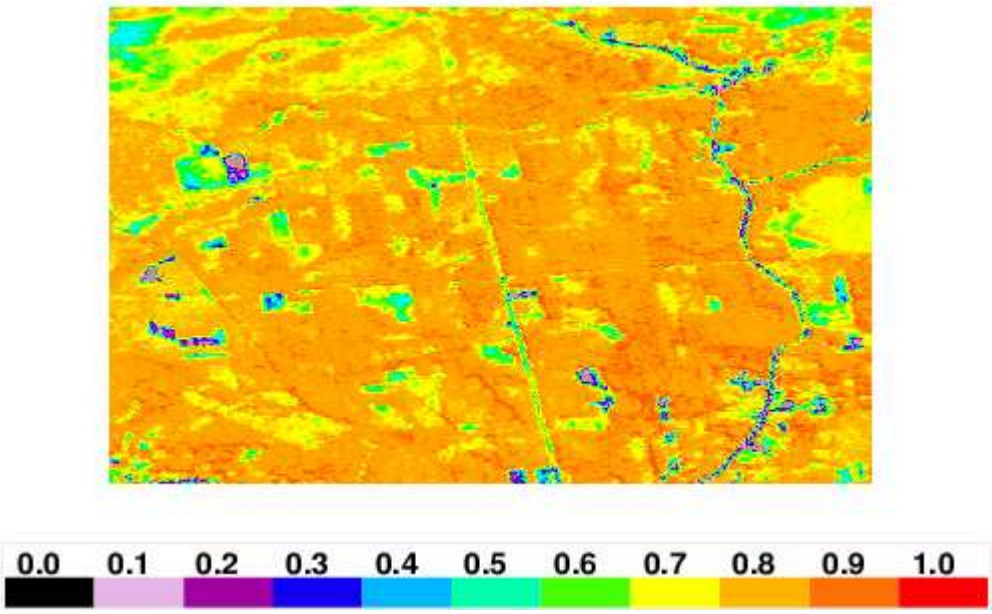

Annex 6 8 : FVC map (20m resolution) from VALERI ground data over Jarvselja (Estonia)

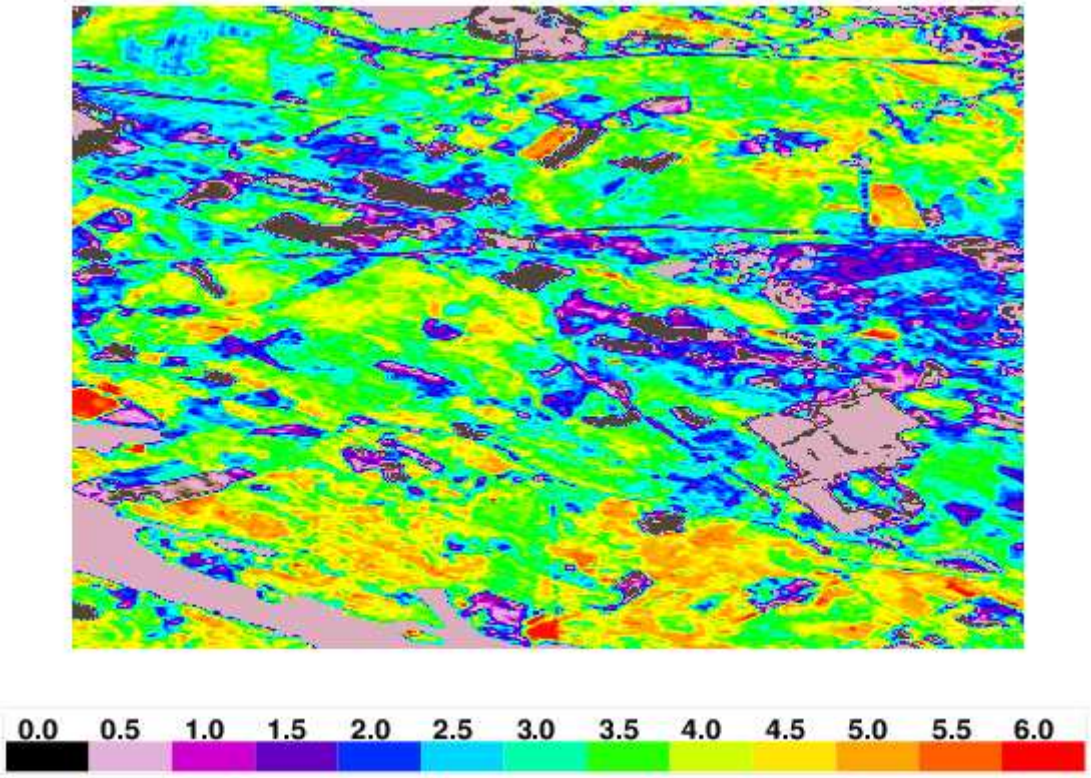

Annex 6 9 : LAI map (20m resolution) from VALERI ground data over Hirsikangas (Finland)

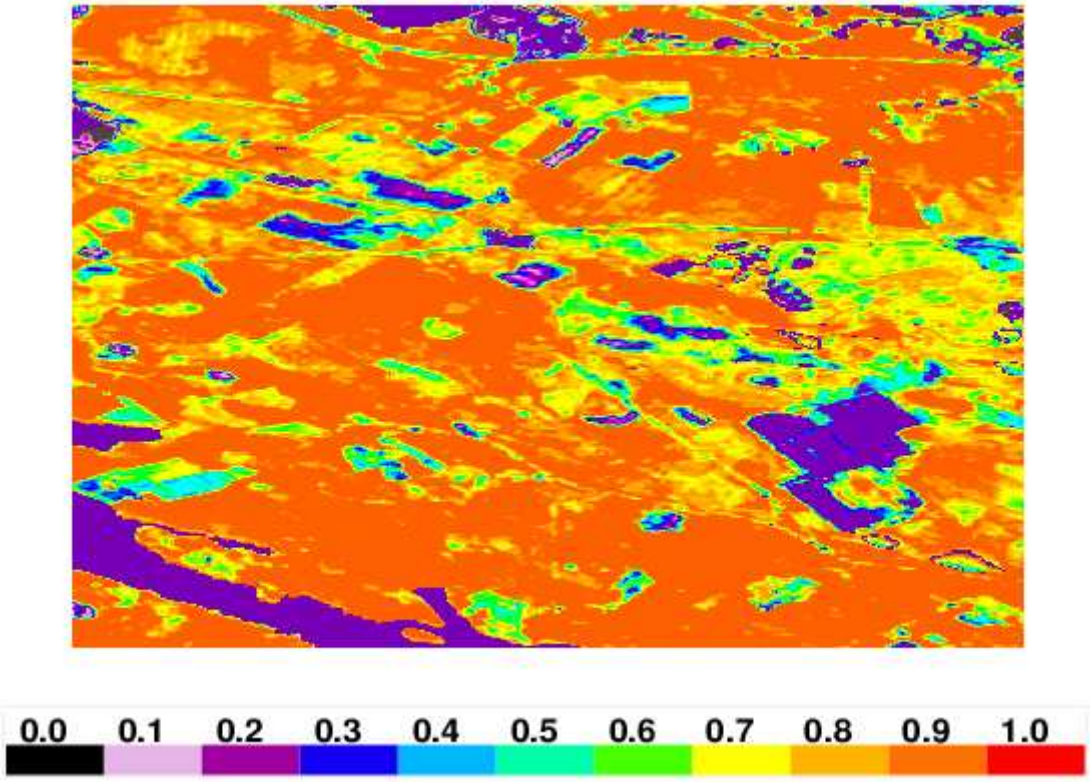

Annex 6 10 : FVC map (20m resolution) from VALERI ground data over Hirsikangas (Finland)

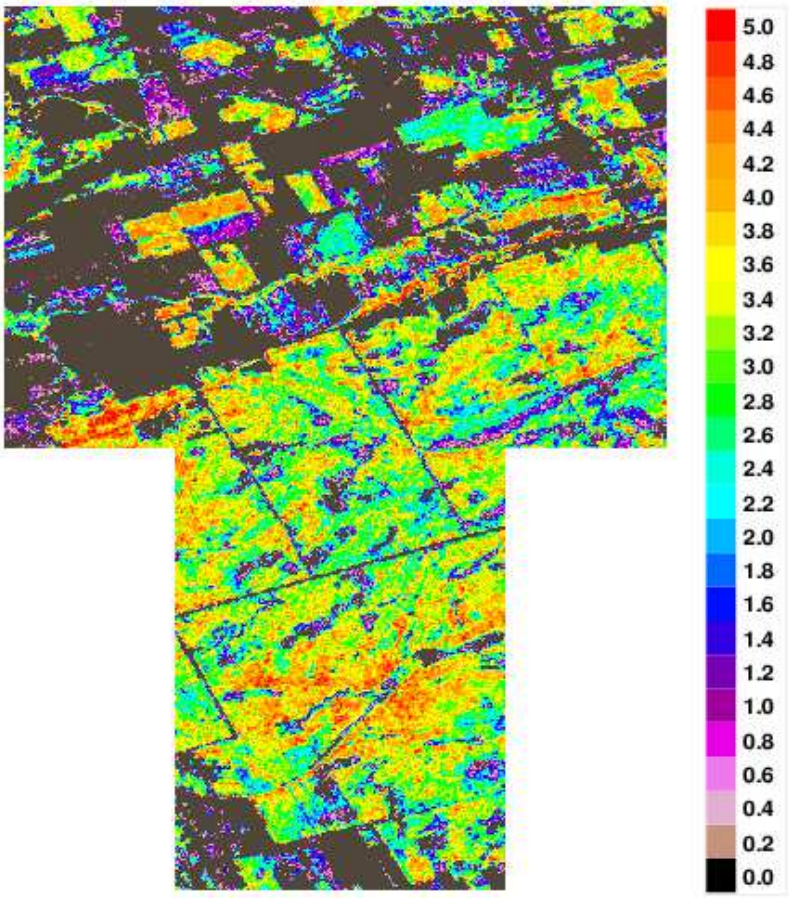

Annex 6 11 : LAI map (20m resolution) from VALERI ground data over Larose (Canada)

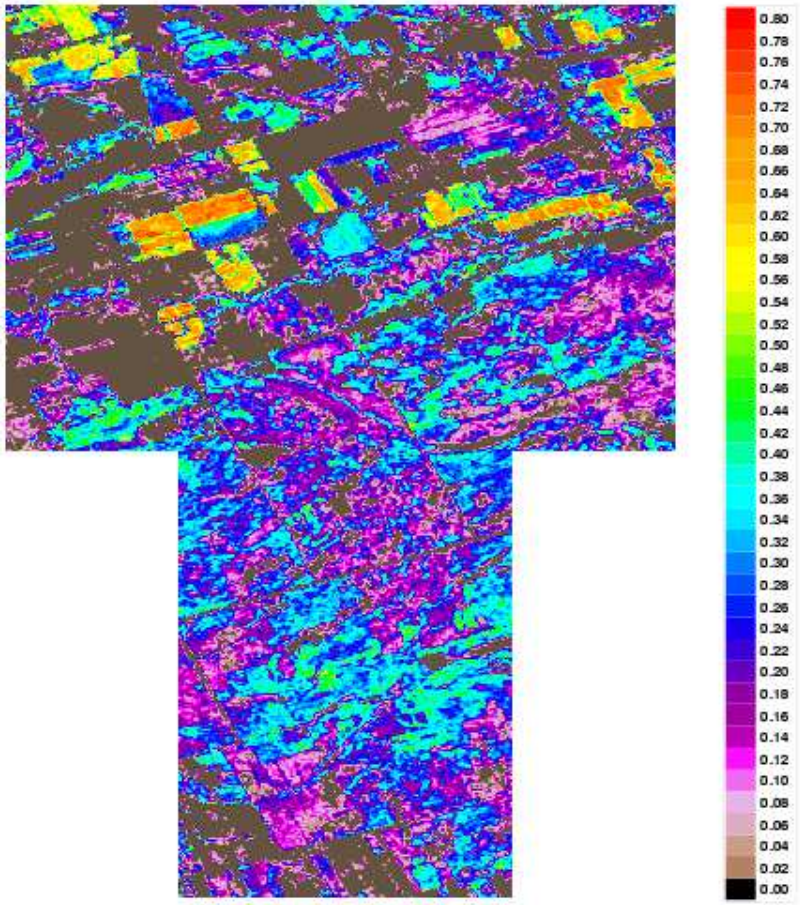

Annex 6 12 : FVC map (20m resolution) from VALERI ground data over Larose (Canada)

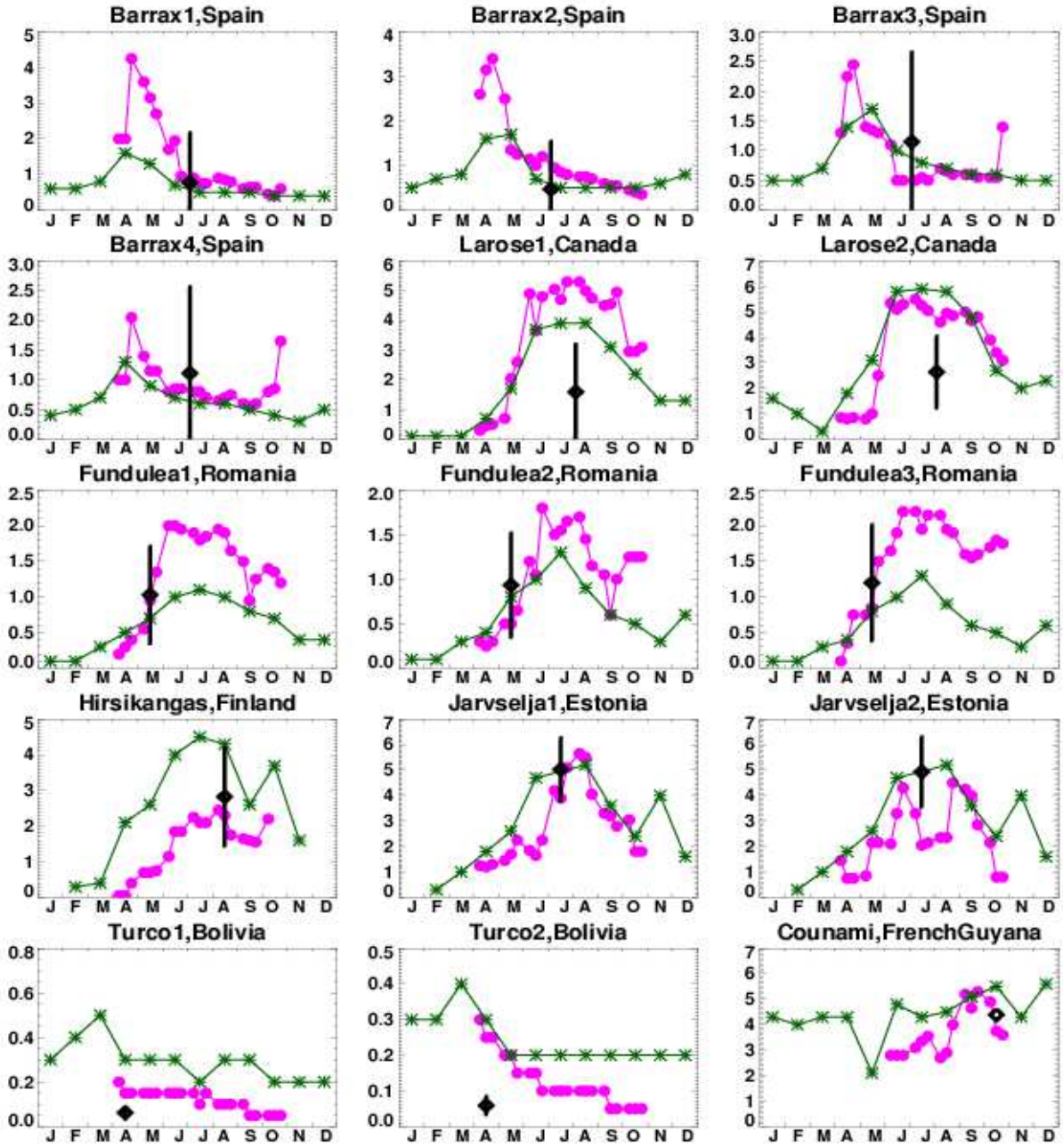

Annex 6 13 : Comparison of LAI from POLDER-2 (magenta), MODIS (green) and VALERI reference maps (black)

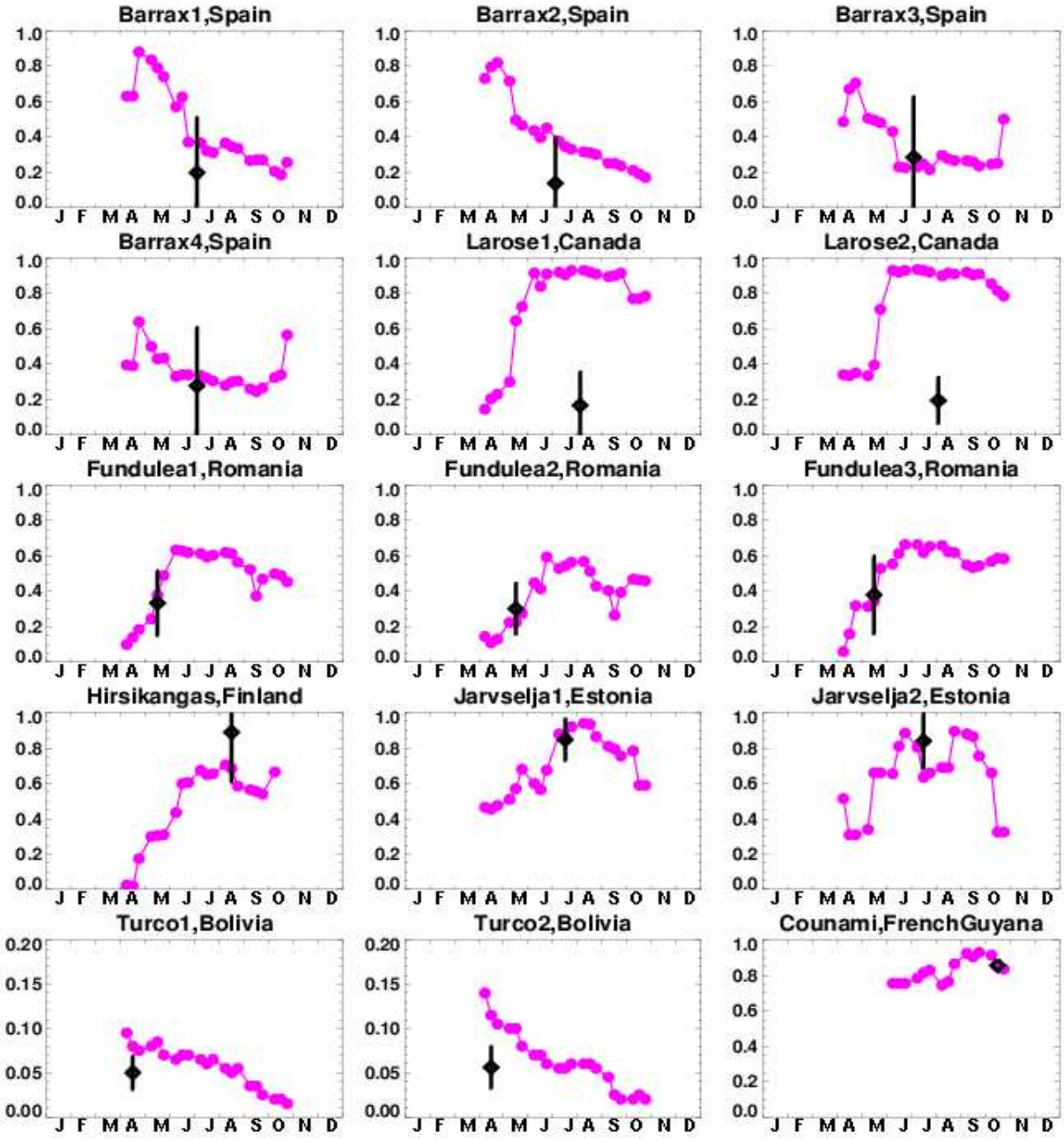

Annex 6 14 : Comparison of FVC from POLDER-2 (magenta) and VALERI reference maps (black)